5-2005

An Investigation of the Current Distribution in an HTS Triaxial Power Cable and its Operational Impacts on a Power System

Marcus Aaron Young II
University of Tennessee - Knoxville

To the Graduate Council:

I am submitting herewith a thesis written by Marcus Aaron Young II entitled "An Investigation of the Current Distribution in an HTS Triaxial Power Cable and its Operational Impacts on a Power System." I have examined the final electronic copy of this thesis for form and content and recommend that it be accepted in partial fulfillment of the requirements for the degree of Master of Science, with a major in Electrical Engineering.

Marshall O. Pace, Major Professor

We have read this thesis and recommend its acceptance:

Aly Fathy, Michael J. Gouge

Accepted for the Council:
Dixie L. Thompson

Vice Provost and Dean of the Graduate School

(Original signatures are on file with official student records.)

To the Graduate Council:

I am submitting herewith a thesis written by Marcus Aaron Young II entitled "An Investigation of the Current Distribution in an HTS Triaxial Power Cable and its Operational Impacts on a Power System." I have examined the final electronic copy of this thesis for form and content and recommend that it be accepted in partial fulfillment of the requirements for the degree of Master of Science, with a major in Electrical Engineering.

Marshall O. Pace
Major Professor

We have read this thesis
and recommend its acceptance:

Aly Fathy

Michael J. Gouge

Accepted for the Council:

Anne Mayhew
Vice Chancellor and Dean of Graduate Studies

(Original signatures are on file with official student records.)

An Investigation of the Current Distribution in an HTS Triaxial Power Cable and its Operational Impacts on a Power System

A Thesis
Presented for the
Master of Science Degree
The University of Tennessee, Knoxville

Marcus Aaron Young II
May 2005

Acknowledgements

I wish to thank all those who helped me complete my Master of Science degree in Electrical Engineering. I would to thank Dr. Mike Gouge and rest of the Applied Superconductivity Group at the Oak Ridge National Laboratory for the opportunity to participate in HTS related research, and for their assistance with this project. I would like to thank Dr. Marshall Pace and Dr. Aly Fathy for their assistance with some of the electromagnetic field theory. I would also like to thank Dr. Jack Lawler for his assistance on some the power system issues.

I would like to thank Andrea Mansoldo of Pirelli Cavi e Sistemi Energia S.P.A, and Laszlo Prikler of the Budapest University of Technology and Economics, for their assistance with the ATP model and power system configuration.

Lastly, I would like to thank Albert Keri and Doug Fitchett of American Electric Power for their assistance with this study.

Abstract

An investigation of the current distribution in a 3-phase triaxial superconducting cable was conducted to study the phase imbalance under steady-state operation and to assist in the construction of a transient model to study operational impacts in a power grid.

The triaxial cable consisted of three superconducting concentric phases inside a copper shield, with each phase composed of multiple layers of BSCCO tape wound helically in opposite directions. Current distribution within the cable was determined by using an electric circuit (EC) model containing the self and mutual inductances resulting from both axial and tangential magnetic fields. An AC loss term was also included in the model. Building on the EC model, a lumped cable model was used to investigate the effects of the triaxial cable on a power grid when faults are applied to the system. Cable lengths for future applications (~16 km) were considered.

Steady-state simulation of the EC model revealed that the electrical imbalance associated with the phases of the triaxial cable may be negligible for cable lengths less than one mile, but become more of a concern at greater lengths. Transient simulations showed that fault currents approaching 30 kA_{peak} may be possible under certain conditions and that resulting induced shield currents may be substantial.

Recommendations for further research are provided as well as possible suggestions for alleviating the electrical imbalance.

Table of Contents

List of Tables

List of Figures

Chapter 1

Introduction and Background

Since the discovery of superconductivity at the beginning of the twentieth century, researchers have been attracted by its potential for high current-carrying capacity for use in electric power transmission systems. Early attempts to design superconducting power cables showed technical promise, but proved impractical from an economic standpoint due to costs of the liquid helium cooling needed to obtain critical temperatures approaching 4 K [1]. In the late 1980's, certain ceramic compounds were discovered that could achieve a superconducting state at temperatures > 77 K. These superconducting ceramic compounds, or high temperature superconductors (HTS), could be cooled using liquid nitrogen (LN2) at costs much cheaper than their liquid helium-cooled, low temperature superconducting (LTS) counterparts. The discovery of HTS materials including the improvement of HTS tape conductors to large engineering critical current densities approaching 20 kA/cm^2 at 77 K have caused a resurgence in the research and development of superconducting power cables, including a triaxial HTS cable prototype to be installed in Columbus, Ohio by Ultera and American Electric Power (AEP).

Advances in superconductor technology make the prospect of economical operation of a superconducting cable a practical concept for certain utility grid applications. One such application is in urban centers, where an increasing populous and industrial presence has increased the demand for electric power in already overloaded transmission grids. Considering the high costs of digging new underground tunnels, and with no room to add more cables in existing tunnels, retrofitting existing underground cables with HTS power cables that can carry over three times the current of conventional, oil-cooled, copper cables may be a logical solution. In addition, the large oil-cooled cables that currently transport electric power though underground tunnels are lossy and potentially pose an

environmental hazard if the cooling oil leaks. HTS power cables would eliminate this environmental hazard because the oil is replaced with environmentally friendly LN2 [2].

1.1 General Behavior of Superconductors

Superconductors have the ability to conduct DC electrical current with virtually zero resistance within a specific operating range when cooled below their critical temperature, T_c. The maximum amount of current that can be applied to a superconductor at a certain temperature without encountering resistance is known as the critical current, I_c, and is defined in practice to be the DC current that produces a voltage gradient of 1 μV/cm. If the applied current or temperature exceeds the critical value, the conductor becomes resistive and assumes the normal state of operation. The resistance of an ideal HTS conductor as a function of temperature is presented in figure (1.1) and

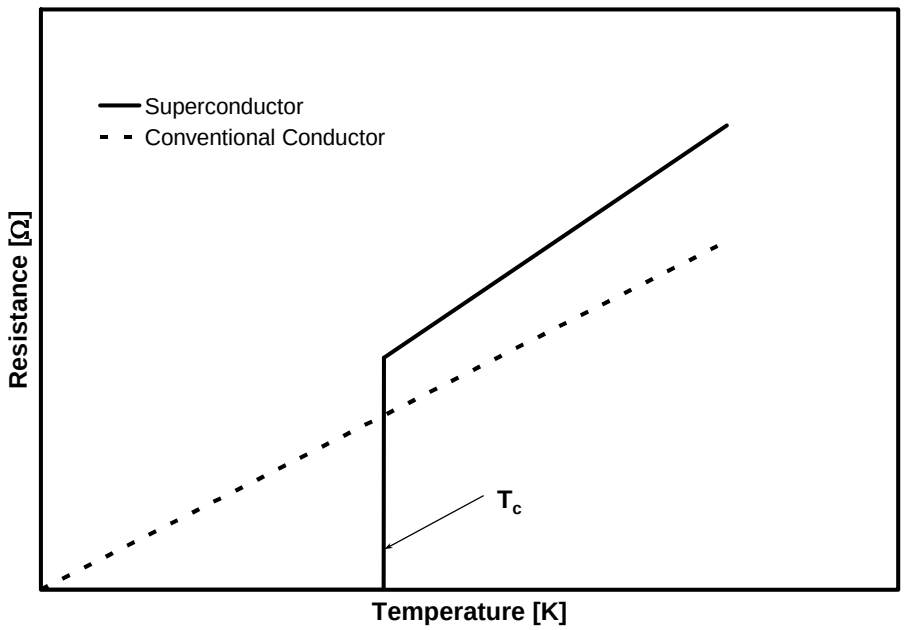

Figure (1.1) Comparison of the resistance curves for an ideal superconductor and a conventional conductor in the 0-300 K temperature range.

reveals that the resistance is virtually zero for temperatures up to T_c, then the conductor assumes the linear resistance of the normal state. A comparison of the V-I curve of an actual superconductor to that of conventional copper is presented in figure (1.2). As shown in figure (1.2), when $I>I_c$ is applied, the HTS conductor reaches an unstable mode of operation where small changes in current result in large changes in voltage. It is in this mode of operation where thermal gradients can cause permanent damage to the HTS conductor if precautionary measures are not taken. The superconductivity of a material is also affected by externally applied magnetic fields where perpendicular fields relative to the flat surface of the HTS tape cause the most degradation of the I_c [3]. However, for most HTS cable designs, the magnetic fields generated are parallel to the tape surface and do not adversely affect the conductors so significantly. More detailed information regarding the physics and behavior of high temperature superconductivity is available in literature [4], and is not discussed further in this study.

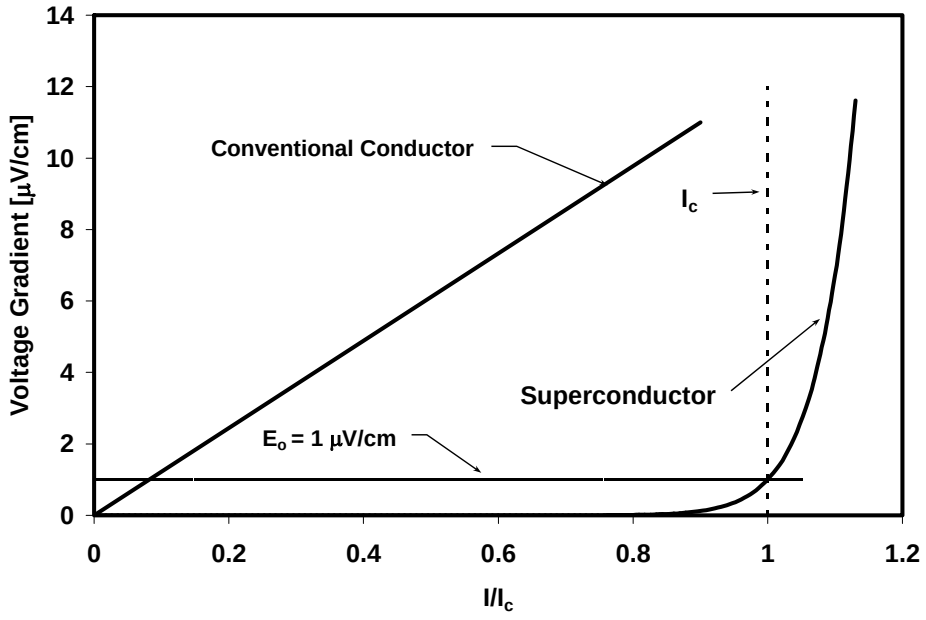

Figure (1.2) Comparison of V-I curves for an actual superconductor and a conventional conductor.

1.2 HTS Power Cables

HTS power cables generally consist of helically wound layers of HTS tape around a former. Many layers of a dielectric material are wound around the HTS tapes to electrically insulate the conductors. An HTS cable is then typically encased in a stainless steel, vacuum-jacketed cryostat to insulate the cryogenic environment from ambient temperatures. The LN2 cooling scheme utilized by an HTS power cable is characterized by its cable type and is designed based on the cable configuration and particular application. Heat losses that affect cryogenic cooling in HTS cables result from the AC losses in the HTS tapes and heat-in-leak losses that occur from outside ambient temperature gradients across the cryostat. One of most technically challenging aspects of an HTS cable is the termination design, where a temperature transition from a conventional copper conductor at ambient temperature to LN2-cooled, HTS occurs while maintaining a closed electrical circuit. A description of a single-phase HTS cable is presented in figure (1.3).

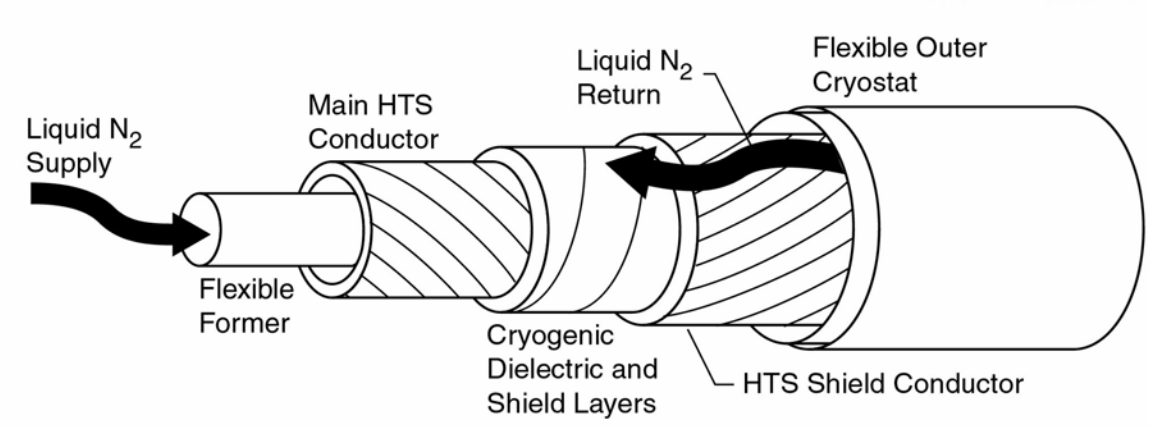

Figure (1.3) Single-phase HTS cable with an HTS return path (coaxial shield).

1.2.1 HTS Tapes

There are many kinds HTS conductors available for use in HTS power system applications [5]. For the majority of HTS power cable designs, $Ba_2Sr_2Ca_2Cu_3O_2$ (BSCCO) is preferred because of its mechanical strength and ability to be fabricated easily in long lengths [6]. HTS BSCCO tape conductors are fabricated using the oxide powder-in-tube or OPIT technique, where the ceramic BSCCO powder is poured into a cylindrical Ag/alloy sheath consisting of a meshed cross-section. The Ag/alloy cylinder and BSCCO powder is then subjected to a series of heating and annealing treatments, until a flat HTS tape is produced. Additional mechanical and electrical stabilizers can then be applied if desired. Although not as ductile as conventional copper conductors, BSCCO HTS tapes are flexible enough so that the helical winding of them up to a critical lay angle does not degrade I_c. A schematic of the Ag/alloy cylinder and fabricated HTS tape is presented in figure (1.4). The amount of BSCCO relative to the matrix material is referred to as the fill factor. For instance, a fill factor of 40% refers to an HTS tape that consists of 40% BSCCO and 60% matrix material.

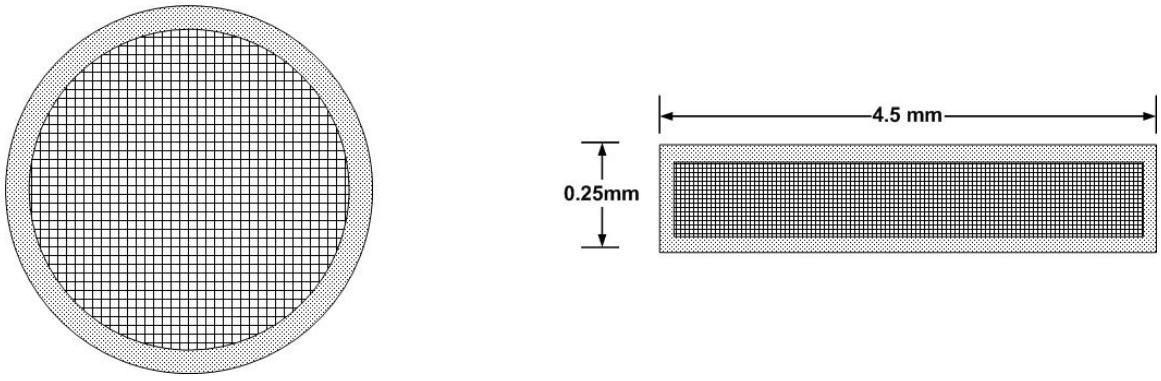

Figure (1.4) Fabrication of BSCCO HTS tape using the OPIT technique. Ag/alloy cylinder with meshed cross-section (left) and fabricated HTS tape (right) with typical dimensions.

1.2.2 Types of HTS Power Cables

Cable designs employing HTS tape technology are characterized as either warm dielectric (WD) or cold dielectric (CD) depending on their liquid nitrogen cooling schemes. WD cables have a nitrogen flow through the core so that the HTS conductor is cooled from the inside out, while the dielectric is applied on the outside of the cryostat at ambient temperature. CD cables have a nitrogen flow on the outer surface of the cable so that the dielectric material is exposed to the cryogenic environment and the HTS conductor is cooled from the outside in. A schematic of both cable types is presented in figure (1.5). Generally, CD cables have a nitrogen flow through the core in addition to the outer flow. Both types of HTS cables have positive and negative attributes [7]. Due to the ambient temperature of the applied dielectric on WD cables, low cost conventional dielectric materials can be used to electrically insulate the conductors, it also makes

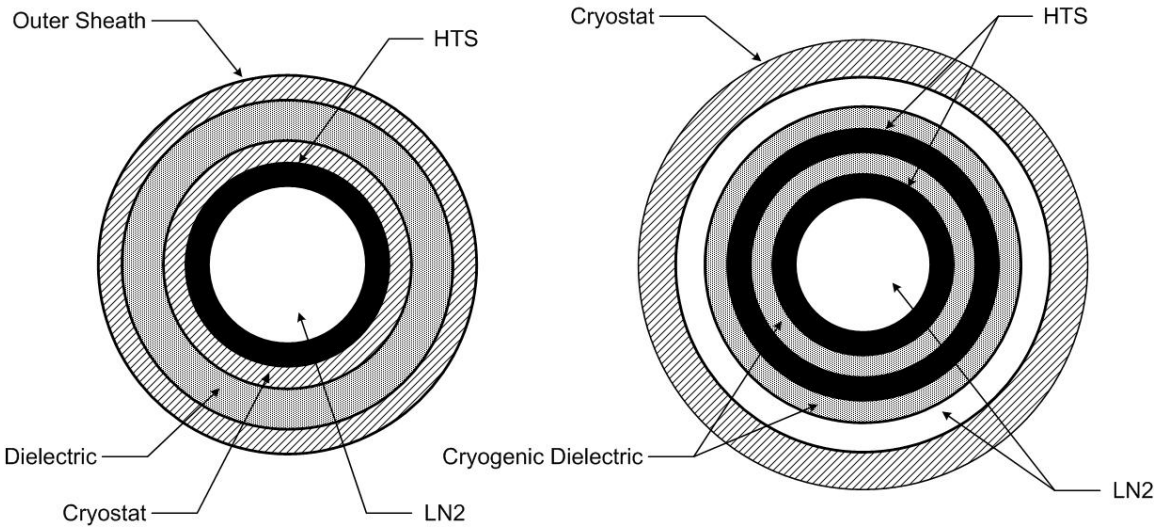

Figure (1.5) Types of cryogenic power cables. Warm dielectric (left) with one HTS conductor path and cold dielectric (right) with two HTS conductor paths (coaxial).

possible the installation of such cables into already existing ductwork. This ability makes WD cables attractive for retrofits where power cable ductwork already exists. It also results in lower material and installation costs. Although WD cables can handle a power capacity double than that of conventional oil-cooled copper cables at the same voltage rating, the lack of an electrical return path results in transport losses in the cryostat, ductwork, and other cables due to stray magnetic fields. CD cables have higher initial costs than WD cables due to the additional HTS shielding material and expensive LN2-impregnated dielectric materials that can withstand cryogenic temperatures. However, the outer nitrogen flow in CD cables allow for an HTS return path to shield magnetic fields so that no transport losses occur in surrounding cable components. Although initially the costs of CD cables may be higher than the WD type, these costs may be balanced over long term operation because CD cables can operate at a higher current capacity with minimal transport losses. These advantages in CD cables result in potential power capacities approaching four times conventional cables. The types of HTS power cables have been summarized in table (1.1).

1.2.3 Geometric Configurations of HTS Power Cables

Several geometric configurations for HTS power cables have been considered for 3-phase electric power transmission, each with its own advantages and drawbacks. Major HTS cable projects currently under way are utilizing three basic geometric schemes based on the particular cable application. These three geometric configurations: coaxial, triad, and triaxial, are discussed in the literature [8, 9] and presented in figure (1.6). A brief description of each configuration is included in this study and summarized in table (1.2).

The coaxial design contains both an HTS forward conducting path and an HTS return conducting path. A description of this arrangement has been presented in figure (1.3). To achieve three electrical phases, three of these single-phase coaxial cables are positioned

Table (1.1) Comparison of HTS power cable types

Cable Type	Description	Advantages/Disadvantages
Warm-dielectric	-LN2 flow in core only. -Dielectric materials are applied outside the cryostat at ambient temperature.	-Can be insulated with conventional dielectric materials -Can be installed into existing ductwork resulting in lower installation costs. -Potential power capacities approaching double that of conventional cables. -Requires metal shielding.
Cold-dielectric	-LN2 flow on outside of cable and possibly through core also. -Dielectric materials operate in a cryogenic environment.	-Requires more expensive dielectric materials that can operate at 77 K. -HTS shielding can be used to contain magnetic fields, decreasing the amount of heat loss due to induced currents. -Potential power capacities approaching 4 times that of conventional cables possible.

Table (1.2) Comparison of HTS power cable designs.

Design	Advantages	Disadvantages
3-phase coaxial	-No metallic shield required. -No external magnetic fields, so no heat losses from surrounding ductwork caused by induced currents.	-A large amount of HTS tape is required because of the HTS shield. -Requires three cryogenic systems to cool the three cables.
Triad	-The amount of cryogenic surface area is reduced. -Consumes less space than the 3-phase coaxial design.	-Like the 3-phase coaxial, there is still an HTS shield. -Cryogenic resources are reduced, because there is only one LN2 return path, but there are still three separate forward paths.
Triaxial	-Amount of cryogenic surface area is significantly reduced. -No HTS shield is required, reducing the amount of HTS tape by a factor of 2. -Consumes much less space than the other two designs.	-Small electrical imbalance due to cable asymmetry. -All phases replace in case of defect.

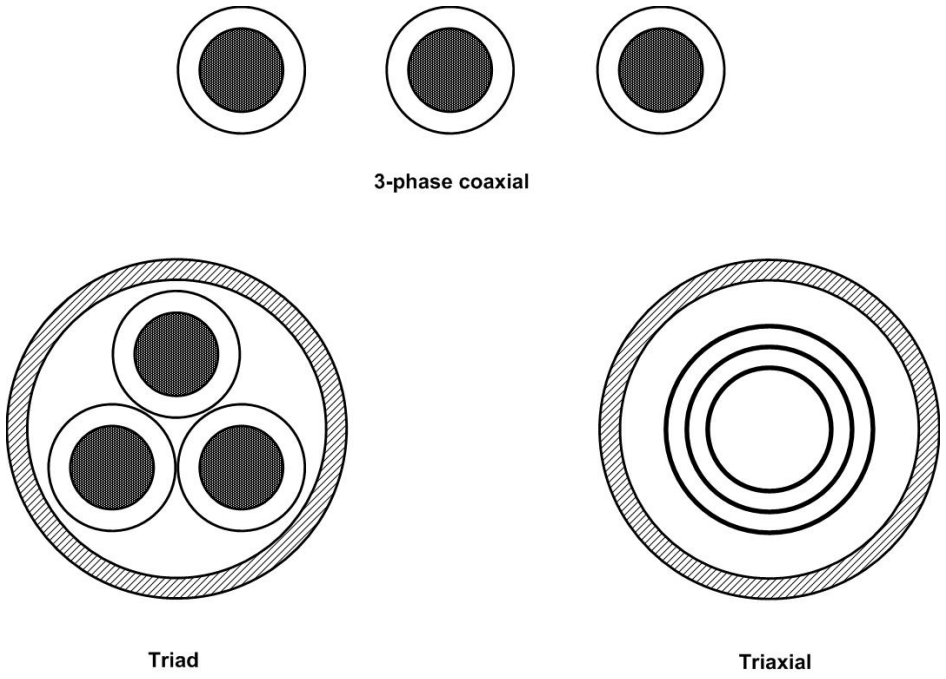

Figure (1.6) 3-phase HTS power cable configurations.

adjacently in a parallel arrangement with three separate sets of terminations. This configuration has been successfully demonstrated [10, 11] at the Southwire Plant in Carrolton, Georgia with over 26,000 hours of operation supplying power to the Southwire manufacturing plant since 2001. There are a few desirable qualities of the CD coaxial design that make it more desirable than other cable configurations. First, the outer LN2 flow allows for an HTS return path so that the vector sum of the external magnetic fields is zero, eliminating the need for a metallic shield. Since there are no magnetic fields on the outside of the cable, heat loss resulting from induced currents in the cryostat or other surrounding metal parts does not occur, therefore the capacity for current flow in the coaxial design is up to four times that of conventional cables of the same voltage rating. Second, the coaxial design is the easiest to realize technically from an electrical and cryogenic standpoint because it consists of three, more simple single-phase systems. However, there are drawbacks to this design starting with the increased amount of HTS tape required to make the return conducting path, and the considerable amount of tunnel

space consumed by the three single-phase systems. Another economic drawback of the coaxial design is the additional operational and maintenance costs resulting from the three separate cryogenic systems.

The triad design consists of three single-phase HTS cables placed triangularly in a common cryostat. Such a design has been successfully developed by Tokyo Electric Power and Sumitomo Electric Industries [12, 13]. Both WD and CD versions of this design have been considered, although the WD has perpendicular field issues that degrade cable I_c. The advantages of the triad design are that the total cryogenic surface area and the amount of consumed space have been effectively reduced due to the common cryostat. However, the amount of HTS tape has not been reduced because the CD version of this design consists of three coaxial HTS cables.

The triaxial design is a CD cable in which all three electrical phases are arranged concentrically in a single cryostat. The basic construction of the triaxial cable design is presented in figure (1.7). Since the net vector sum of the magnetic fields of the three phases is small in this design, an HTS return path is not needed, and the amount of HTS tape is reduced by a factor of two relative to the coaxial and triad designs. In addition, the total cryogenic surface area has been significantly reduced, thereby reducing the cryogenic system capacity required to adequately cool the cable. These advantages coupled with its compact size make the triaxial cable an interesting prospect for power utilities with an expanding power capacity and limited conductor space. However, there is an inherent electrical imbalance due to an asymmetry in the cable cross-section. The differences of radii of the three concentric phases cause a small net current imbalance during steady-state operation that result in net external magnetic fields. These magnetic fields are small enough that a cold copper shield at 77 K placed concentrically with respect to the three phase conductors can adequately manage any induced currents. A prototype of the triaxial design has been scheduled for installation at the Bixby substation in Columbus, Ohio by Ultera and American Electric Power [14]. Although technically the

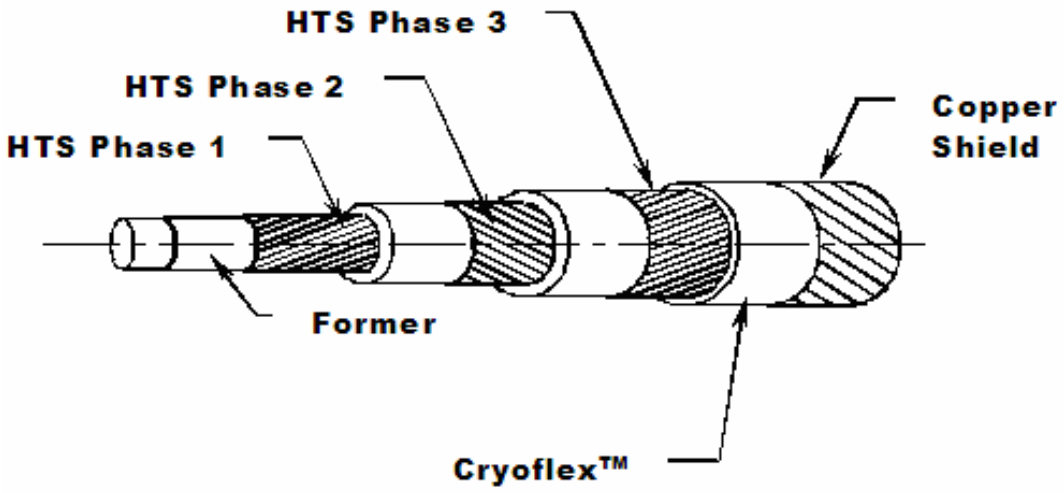

Figure (1.7) 3-phase triaxial cable with cold copper shield.

most difficult to realize because of termination issues and temperature gradients during transients, the triaxial design has prompted interest from cable designers and utilities and is hence the subject of this study.

1.3 Triaxial Cable Study

The triaxial cable to be installed at the Bixby substation in Columbus, Ohio has design specifications to achieve a rating of 13.2 kV, 3 kA_{rms} per phase, and 69 MVA. The 200 m-long prototype will connect two 13.2 kV buses that feed a radial line. The cable will be feed by a 138 kV/13.2 kV, DELTA/WYE-grounded transformer containing a circuit breaker on the high side. A circuit breaker will also be applied at the termination bus, where radial lines will supply power to their respective loads. The cold copper shield and stainless steel cryostat will be grounded at the endpoints to substation ground. A line

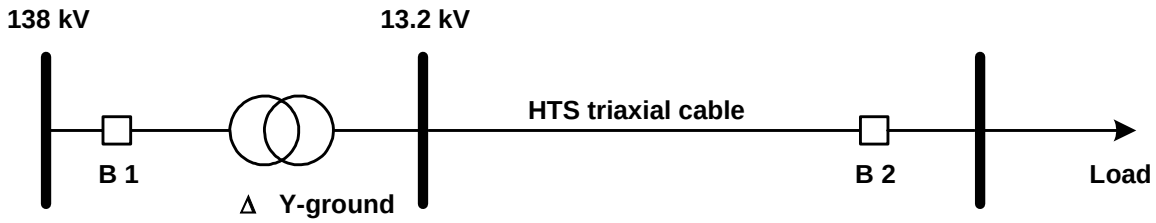

Figure (1.8) Line diagram of the triaxial cable at the Bixby substation.

diagram describing the basic substation components and location of the triaxial cable is presented in figure (1.8). The purpose of this study is to investigate the electrical properties of a triaxial cable for cable lengths > 200 m where electrical imbalances may be more significant. Line lengths practical for future applications, ~16 km, will be considered under different operating conditions.

1.3.1 Electric Circuit Model

An electric circuit (EC) model will be constructed to represent the triaxial cable for simulation in the Alternative Transients Program. Previous studies have evaluated single-phase HTS cables using EC models to study current distribution throughout the HTS tape layers [1, 15-17]. These studies have been used to optimize tape lay angles so that current distribution across the HTS cable cross-section is uniform, resulting in reduced AC losses. For the purpose of this study, the lay angles are assumed to be optimized by cable designers so that the investigation can focus on the electrical interaction of the three phases. Therefore, pi-equivalent circuits, which account for mutual and self inductances, capacitances, and the resistance of each phase, will be used to model the cable. The phase resistances are dynamic and will be modeled as functions of the transport current. An ATP subroutine will be used to model the cold copper shield. The resulting triaxial EC model will contain all three HTS phases and the cold copper shield.

1.3.2 Triaxial Cable Specifications

The specifications of the triaxial HTS cable considered in this study are presented in table (1.3). A sketch of the triaxial cross-section is presented in figure (1.9). From the inside-out, the triaxial cable basically consists of a hollow corrugated former wrapped with layers of bedding tape. The first HTS conductor phase, phase A, is then applied consisting of two helically wound layers of HTS tape. The two HTS layers are wound in opposite directions to cancel magnetic fields and are wrapped with multiple layers of Cryoflex^{TM}, a dielectric tape material designed for operation in cryogenic temperatures. Phases B and C are constructed in the same matter as phase A, so that all three layers are wrapped in layers of Cryoflex^{TM} to electrically insulate the phases from each other and the copper shield, A space between the copper shield and the cryostat provide a path for a LN2 flow.

Table (1.3) Technical specifications of the HTS triaxial cable.

Cable Parameter	**Value**
Phase current [A_{rms}]	3,000
Voltage [Vrms]	15,000
HTS tape cross-section [mm]	4.16 X 0.2
Operating temperature [K]	77
Phase A Ic [A]	5860
Phase B Ic [A]	6490
Phase C Ic [A]	6700
Phase A ID/OD [mm]	42/43
Phase B ID/OD [mm]	47/48
Phase C ID/OD [mm]	52/53
Shield ID/OD [mm]	58/60
Phase A lay angles [degree]	20/22
Phase B lay angles [degree]	24/25
Phase C lay angles [degree]	30/31

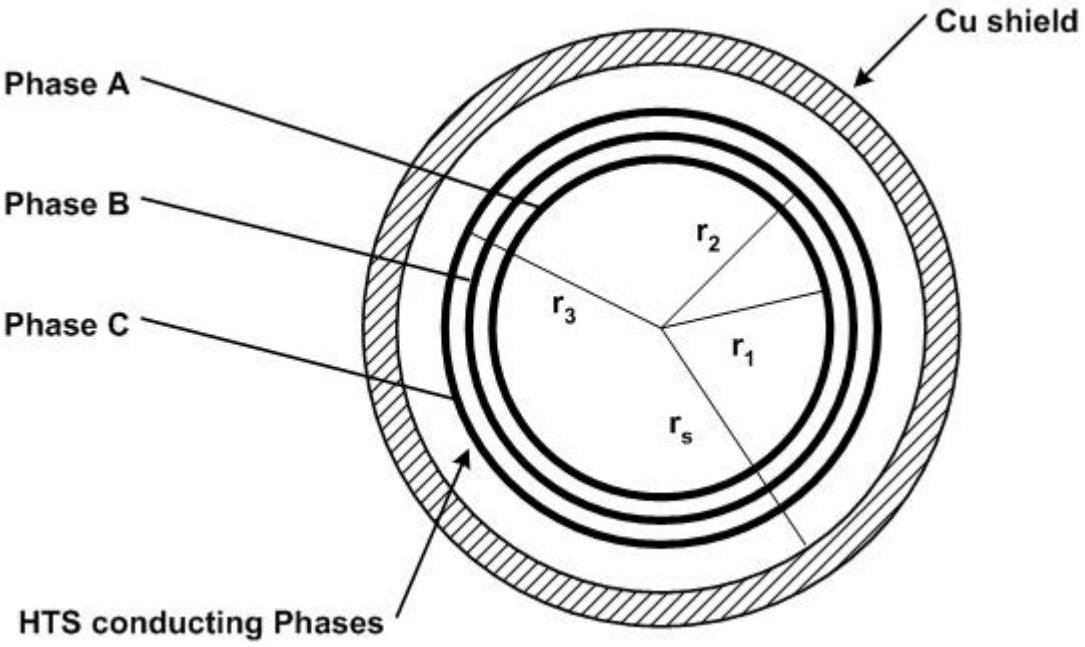

Figure (1.9) Triaxial cable cross-section showing the three superconducting phases and the copper shield (not to scale).

1.3.3 Simulation of EC model

The EC model outlined in section 1.3.1 will be simulated for two different operating conditions. In the steady-state operating condition, the cable operates within specified ratings and the applied voltage is symmetrical across the three phases due to a balanced, 3-phase load. This operating condition presents the most balanced case electrically, however cable asymmetry may affect the electrical balance over long lengths.

Transient operating conditions will also be introduced by applying different faults at the load end of the cable. During this mode of operation, electrical imbalances are expected to be large depending on the fault type. For both modes of operation, the induced shield currents will be assessed.

1.3.4 Objectives

The objectives of this study are to calculate the electrical imbalances of the triaxial cable for steady-state and transient operating conditions. Knowledge regarding the order of magnitude of the currents induced in the cold copper shield during steady-state operation will allow for proper design constraints so that significant heating does not affect the HTS layers. The amount of electrical imbalance in the triaxial cable may also present a power quality issue if the power factor angles become too large. For transient operating conditions, knowledge regarding the order of magnitude of the resulting fault currents and induced shield currents will help determine if any addition stabilizer material applied to the electrical phases is needed. The work to be presented here is an exploratory study and is the first step to understanding the electrical behavior of the triaxial design. Future studies may be able to expand upon this work by adding more technical specifications and detailed modeling.

Chapter 2

Triaxial Cable Model

An electric circuit (EC) model was constructed describing the general electrical behavior of the superconducting triaxial cable. Successful use of EC models to represent single-phase HTS cables for studying the current distribution across the multiple HTS tape layers has been previously accomplished [15-20]. The purpose of these studies was to determine the optimal tape lay-angles that result in the most uniform layer current distribution in order to minimize AC losses. The unequal current distribution across the tape layers is due to the inherent impedance difference of each tape layer caused by their different radii. Since the outer tape layers will have larger radii, their inductance will be smaller than the interior layers, and their inductive reactance will be smaller causing current to flow in the outer layers first.

The triaxial cable presents a different problem because it contains three electrical phases that are electrically insulated from each other with dielectric material. Although the current distribution issue is present within the two HTS tape layers of each phase, it is not as significant as the effects of the three-phase transmission paths caused by the difference in phase radii and mutual coupling. As previously stated, the different radii of the concentric three phases cause electrical imbalances to occur. The EC model constructed for this study, accounts for these electrical imbalances by considering the self and mutual impedances caused by the geometrical asymmetry of the three conducting phases, and calculates the effect of these imbalances on the cold copper shield.

An EC model describing the HTS triaxial cable was constructed for use in the Alternative Transients Program (ATP) using a pi-equivalent model. The pi-equivalent was the model chosen to represent the triaxial cable because it is relatively simple to implement and is a standard transmission line model. The pi-equivalent model allows for the consideration of

self-impedances along with mutual coupling, both of which are relevant for this study. Figure (2.1) shows a pi-equivalent circuit for a three-phase line where resistance, R, inductance and L are shown.

2.1 Alternative Transients Program

The EC model was constructed using the Alternative Transients Program (ATP) [21], a power transients program that is a derivative of the Electromagnetic Transients Program (EMTP). ATP was developed to numerically analyze transients for power systems containing a variety of conventional and user-defined components. This ability of ATP to model unconventional components is an advantage over some of the other power systems analysis software packages that have components with fixed capabilities.

Since ATP is a text-based program, it is not as user-friendly as other point and click type software packages. However, the recent development of a schematic capture program for

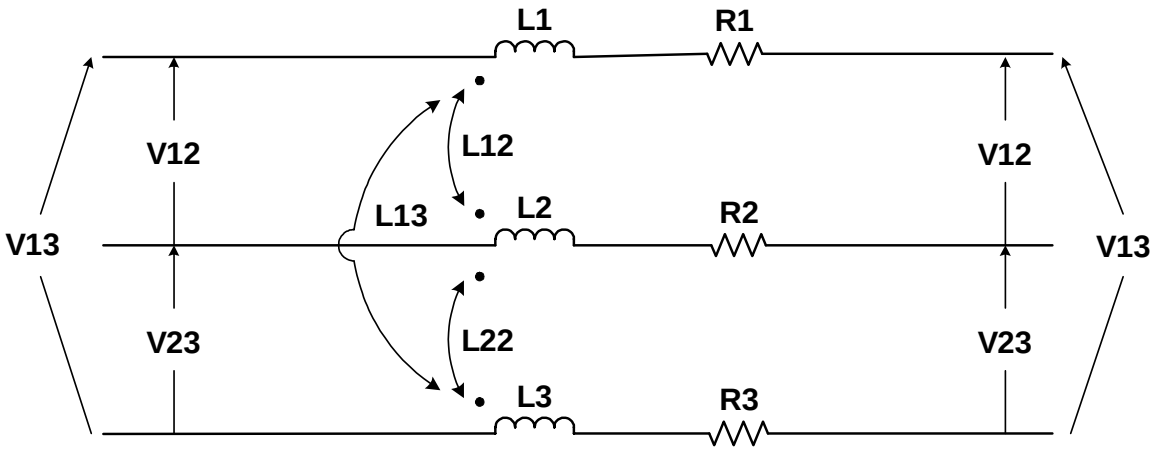

Figure (2.1) Pi-equivalent circuit diagram (Shunt capacitance and shield not shown).

ATP called ATPDraw [22], has significantly reduced the rigor of learning syntax and programming commands. To construct and analyze a system, the user chooses the desired components from the component library, connects the nodes, defines the parameters of each component, and then executes the simulation. ATPDraw converts the schematic into code that is executed by ATP during simulation. The simulation results are stored in an output file where they can be evaluated.

ATP has useful elements and subroutines that assist with the analysis of certain power system components. For modeling the triaxial cable, the cable parameters (CP) subroutine was used to calculate the cable impedances and generate an equivalent-pi model given cable cross-section and material composition. The dynamic resistance of the triaxial cable was modeled using a type-99 nonlinear resistance element that determines phase resistance based on the phase current. Several transmission line models, including the equivalent-pi model, are available in ATP for power transmission studies.

ATP is available by mail or on the web for free, but the user must sign an agreement in order to obtain a license before access to the program is allowed. For the development of the triaxial cable model, an ATP version called ATPMingw32 that is compatible with WindowsXP, along with ATPDraw version 4.1 was used.

2.2 Triaxial Cable Configuration in ATP

The triaxial cable model consists of two major types of components in ATP, the three phase conductors and the copper shield. Represented as sub-matrices in the pi-equivalent model, these components are determined independently and then combined to form the completed model. Both components along with the methods used to determine them are described in this section. The inclusion of a dynamic resistance component that represents the behavior of the HTS conductor is also described.

2.2.1 3-Phase Parameters

The equivalent-pi model requires the RLC parameters of the three conducting phases. For the triaxial cable, the self and mutual inductances resulting from tangential and axial magnetic fields were also included. A more detailed description of the calculation of these inductances is provided in chapter 3. The capacitance was found using conventional methods [23] and is described in chapter 3. To include the dynamic resistance, the three phase resistances in the pi-equivalent model were set to values approaching zero and a type-99 resistance element was connected in series with each phase. This method was used because the pi-equivalent impedance matrix cannot accept changing resistance values. The type-99 element reads a user-defined V-I table from which it chooses a voltage drop based on the phase current. Table (2.1) summarizes the parameters for the 3-phase component of the triaxial pi-equivalent matrix.

Table (2.1) Summary of 3-phase parameters for the pi-equivalent model.

Parameter	Description	Configuration in ATP
Dynamic Resistance (chapter 4)	-An effective dynamic resistance consisting of AC loss and transport loss in the HTS tape. -A function of the phase current. -Temperature is constant.	-Represented by type-99 nonlinear resistance element in series with pi-equivalent.
Series Inductance (chapter 3)	-Accounts for axial and tangential magnetic fields. -Self and mutual inductances are accounted for.	-Represented in pi-equivalent.
Shunt Capacitance (chapter 3)	-Results from the interaction of electric fields.	-Represented in pi-equivalent.

A combination of AC loss and the transport loss within the HTS tapes, the current-dependent resistance was approximated assuming a constant temperature of 77 K. Ohm's law was then used to compile a V-I table based on the approximated dynamic resistance values. Calculation of the effective dynamic resistance and its components are described in detail in chapter 4. To approximate voltages from the V-I table based on phase current, the type-99 element uses linear interpolation to produce a smooth resistance characteristic.

2.2.2 Copper Shield

The cold copper shield surrounding the three electrical phases was included in the model using the CP subroutine in ATP. CP produced a pi-equivalent model containing the impedances of the phase conductors, the shield, and those resulting from mutual coupling. CP accounted for not only the mutual coupling between the phases, but also between each phase and the shield. For the triaxial cable, CP was configured to approximate cable impedances based on a cable in an underground pipe. The program used the Carson and Pollaczek methods to calculate the cable impedances [24], which are dependent on the proximity of the cable to shield and the soil. The behavior of electric power cables in underground pipes have been analyzed in previous studies using these methods without the assistance of ATP [25]. To model the copper shield in CP, the three phase conductors also had to be included into the subroutine so that ATP could calculate the mutual effects of the phases on the shield. To accomplish this, the triaxial cable was specified as having four conducting phases, with the shield being the fourth phase. The corresponding cross-sectional geometry and material properties of the three phases, dielectric, and the shield where entered into CP. CP then produced a 4X4 pi-equivalent matrix describing the three conducting phases and the copper shield. Figures (2.2) and (2.3) show the CP input menus with corresponding triaxial data. Figure (2.4) is a view of the CP generated cable cross-section. A summary of significant CP parameters and their respective values for a 16 km-long cable is presented in table (2.2).

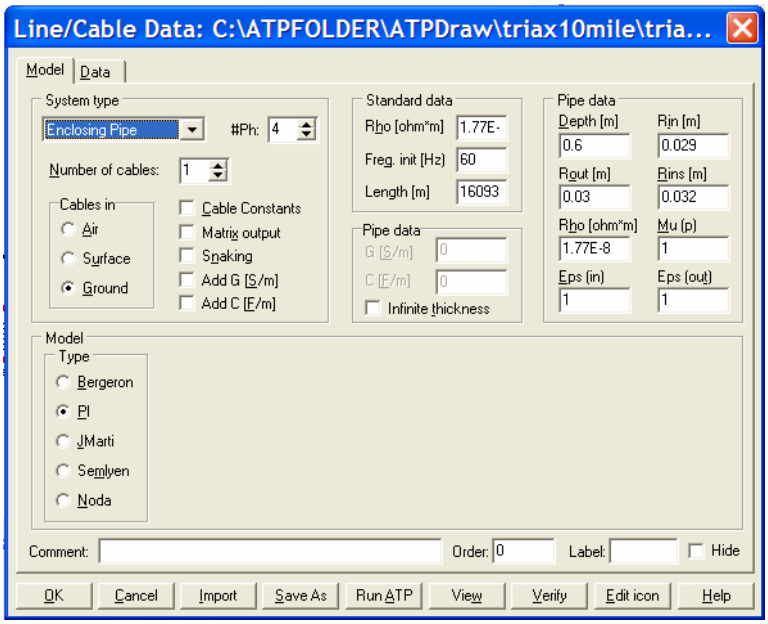

Figure (2.2) Cable Parameters Model menu in ATP for a 16 km-long HTS triaxial cable.

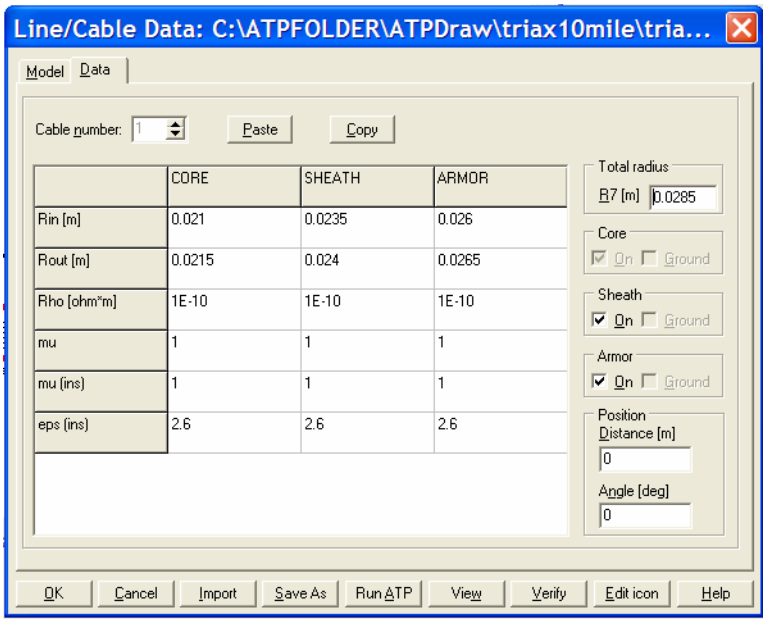

Figure (2.3) Cable Parameters Data menu in ATP for a 16 km-long HTS triaxial cable.

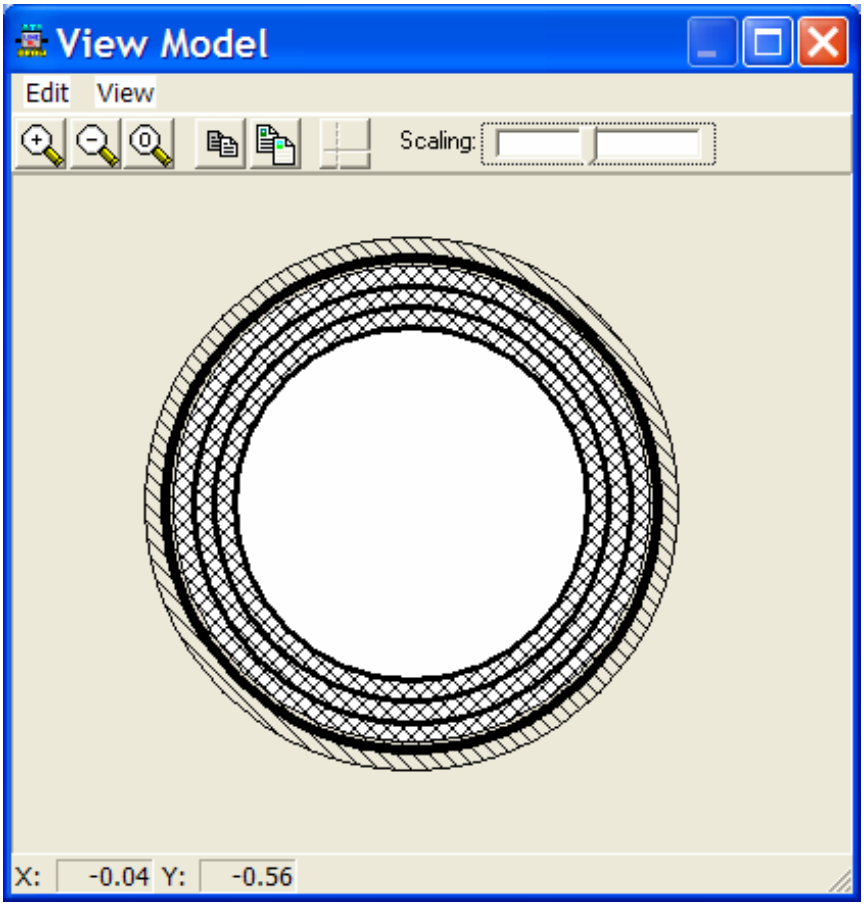

Figure (2.4) Cable Parameters view of the triaxial cable cross-section.

Table (2.2) Significant input parameters for CP to model a 16 km-long HTS triaxial cable.

CP parameter	Description	Value
System Type	Cable type	Underground
# Phases	Number of cable phases.	4 (3 electrical phases and copper shield.)
Length	Cable length	16 km
Rho earth	Soil resistivity	1.77E-8 [ohm*m]
Rho pipe	Resistivity of the copper shield.	1.77E-8 [ohm*m]
Rho conductor	Resistivity of HTS phases.	1E-10 (set to a value approaching zero)
mu	Relative permeability of HTS conductor.	1
mu (ins)	Relative permeability of dielectric (Cryoflex™).	1 (nominal value)
eps (ins)	Relative permittivity of the dielectric (Cryoflex™).	2.6
Core	Represents the first conducting phase.	on (default)
Sheath	Represents the second conducting phase in the triaxial model.	on
Armor	Represents the third conducting phase in the triaxial model.	on

Initially, the earth resistivity was set too high, and the resulting R, L, and C terms for the three phase components were higher than those calculated in chapters 3 and 4. After some investigation, it was discovered that Carson's formula considers the effective radial distance of the magnetic field from the center of the 3-phase conductors to be related to the frequency and resistivity of the propagation medium as presented in equation (2.1).

$$S = \frac{k}{\sqrt{\frac{f}{\rho}}} \qquad [m] \qquad (2.1)$$

S—Conductor-to-image distance below ground.

f—Power frequency (60 Hz).

k—A constant of proportionality.

ρ—Soil resistivity [ohm-m].

Equation (2.1) reveals that higher resistivity values result in a larger effective distance, *S*, which causes the inductive reactance to increase, because the effective distance acts like the radial distance to the shield for the calculation of the inductance. Several values for the resistivity were attempted in CP, and for smaller resistivity values, the impedances of the three phases became smaller, approaching the calculated values. It was discovered that when the resistivity of the earth equaled that of the copper shield, that the three phase impedances strongly correlated with the calculated values. This result assumes that the copper enclosure acts as a complete shield so that earth return currents are avoided, a condition that was also assumed for the calculation of the cable inductances and capacitances in chapters 3 and 4. Therefore the magnetic fields are assumed to exist only in the copper for the purposes of this study, and do not propagate into the earth.

2.2.3 Constructing the Pi-Equivalent Impedance Matrix

The first 3X3 rows and columns of the 4X4 pi-equivalent impedance matrix is the sub-matrix that contains the model of the 3-phase conductors alone, and does not contain any shield components. The resulting impedance values of this sub-matrix from the CP calculation were very close to those calculated in chapter 3, resistance is very small as specified in the CP subroutine. However, CP only evaluates transverse electromagnetic (TEM) phenomena, so axial fields resulting from the helical winding of the HTS tapes are not accounted for. This issue was resolved by replacing the CP values of inductance for the 3X3 sub-matrix by those calculated in chapter 3. The capacitance values generated by CP were nearly an exact match to the values calculated in chapter 3, so no correction was necessary. The resulting pi-equivalent matrix is presented in table (2.3).

Table (2.3) Pi-equivalent impedance matrix for a 16 km-long triaxial cable

Matrix element	R [Ω]	L [mH]	C [μF]
11	10^{-10}	1.13	26.15
21	0.00	0.67	-26.15
22	10^{-10}	0.71	55.23
31	0.00	0.39	0.00
32	0.00	0.37	-29.06
33	10^{-10}	0.38	54.88
41	0.00	0.26	0.00
42	0.00	0.26	0.00
43	0.00	0.26	-19.73
44	1.53	0.24	33.60

2.2.4 Completion of Triaxial Cable Model

To make the pi-equivalent matrix useful for power systems analysis in ATP, it had to be presented in a form to make it accessible to other conventional grid components. To accomplish this a user-defined function called SUPc was created in ATPDraw that accepts the pi-equivalent impedance matrix from an output file, and defines separate nodes for the 3-phase conductors and copper shield. The major benefit of SUPc function is that it allows other system components like the type-99 element, AC sources, and other SUPc functions to be connected in series. This benefit allows for the insertion of voltage and current meters between pi models so that cable data can be acquired as a function of distance, it also allows for the possibility of phase transposition if desired.

The final equivalent circuit consisted of the SUPc function with its three phase conductor node connected in series with a dynamic resistor bank. Both shield nodes are grounded corresponding to the shield being grounded at the endpoints. A description of the ATPDraw schematic of the HTS triaxial cable model is presented in figure (2.5).

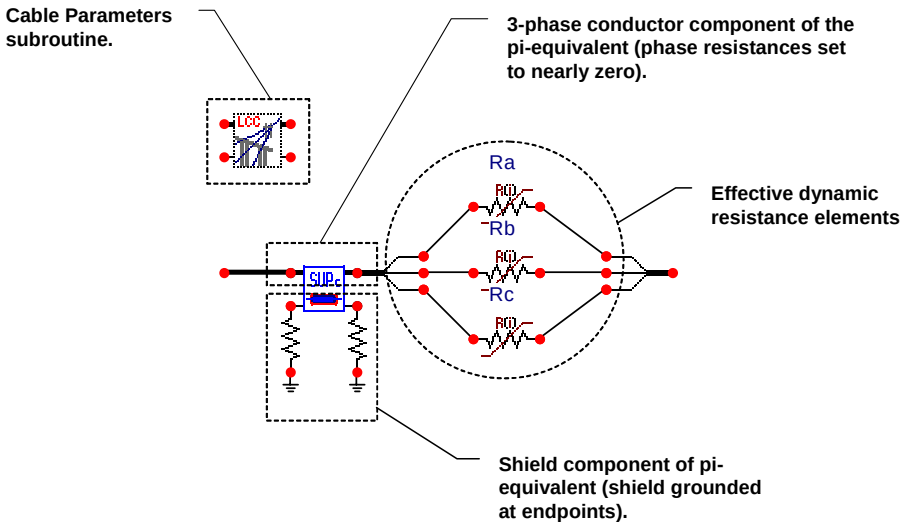

Figure (2.5) ATP circuit representation of the triaxial cable model with grounded copper shield and dynamic resistances.

2.3 Transmission Line Model

A transmission line model of the triaxial cable was composed using the telegraph equations [26] to check results produced by the ATP model. Several approximations were made to simplify the construction of the model including negligible layer thicknesses, exclusion of a non-linear resistance term, and exclusion of the dynamic resistances. Since the transmission line model is valid for only TEM phenomena, the axial field inductance terms are also neglected. A copper shield was included to geometrically set the ground plane, but shield currents were excluded from the analysis. Since these neglected parameters had a small effect on the solutions, their exclusion from the transmission line model did not produce a significant difference from the results in ATP. The characteristic impedance of the line was approximated by the equations for a lossless coaxial line as described in equation (2.2). The wave number was calculated from equation (2.3) and the input impedance was determined using equation (2.4). The telegraph equations were then used to calculate the voltage and current along the line as described in equations (2.5) and (2.6).

$$Z_o = \left(\frac{60}{\sqrt{\varepsilon_r}} \right) \cdot L \qquad \left[\frac{\Omega}{m} \right] \qquad (2.2)$$

$$\beta = \omega \sqrt{\mu \varepsilon} \qquad \left[m^{-1} \right] \qquad (2.3)$$

$$Z_{in}(-l) = Z_o \left(\frac{Z_L \cos \beta l + j Z_o \sin \beta l}{Z_o \cos \beta l + j Z_L \sin \beta l} \right) \qquad [\Omega] \qquad (2.4)$$

$$V_{phasor}(z) = V_o^+ e^{-j\beta z} + V_o^- e^{j\beta z} \qquad [V] \qquad (2.5)$$

$$I_{phasor}(z) = \frac{V_o^{\ +}}{Z_o} e^{-j\beta z} - \frac{V_o^{\ -}}{Z_o} e^{j\beta z} \qquad [A] \qquad (2.6)$$

Z_o—Characteristic impedance

ε_r—permittivity of dielectric material

L—cable inductance matrix

Z_{in}—Input impedance

Z_L—Load impedance

β—Wave number

l—Position along the line

V_{phasor}—Voltage phasor

I_{phasor}—Current phasor

V_o^+—Maximum voltage

V_o^-—Minimum voltage

ω—Resonant angular frequency (f=60 Hz).

These equations were evaluated for a 13.2 kV triaxial cable with a balanced, 3-phase, resistive load, in the same manner as the simulations performed in ATP. Although there are some differences due to the approximations discussed, the results of the transmission line model should describe the relative behavior of the triaxial cable, and therefore should have significant correlation to steady-state results from ATP.

Chapter 3

Inductance and Capacitance

The inductance and capacitance parameters of the 3-phase triaxial superconducting power cable are expressed in matrices, L' and C' [23]. These 3X3 matrices describe the self and mutual values of inductance and capacitance for use in the EC model of the triaxial cable and are represented in per unit length as shown in equations (3.1) and (3.2).

$$L' = \begin{vmatrix} L_{11} & L_{12} & L_{13} \\ L_{21} & L_{22} & L_{23} \\ L_{31} & L_{32} & L_{33} \end{vmatrix} \quad \left[\frac{H}{m}\right] \qquad (3.1)$$

$$C' = \begin{vmatrix} C_{11} & -C_{12} & C_{13} \\ -C_{21} & C_{22} & -C_{23} \\ C_{31} & -C_{32} & C_{33} \end{vmatrix} \quad \left[\frac{F}{m}\right] \qquad (3.2)$$

Where the diagonal entries of the matrices are the self inductance and capacitance terms, and the off-diagonals represent mutual terms. As for all transmission lines, including the triaxial cable, the inductance and capacitance parameters are functions of both geometry and electromagnetic material properties, and are independent of current and voltage [26, 27]. The discussion presented in this chapter focuses on the calculation of the inductance and capacitance parameters of the triaxial cable.

3.1 Self Inductance

The inductance of the triaxial cable was determined by investigating the associated magnetic fields or *B* fields. Due to the helical winding of the HTS tapes along the cable axis and direction of current in the tapes, the orientation of the *B* field can be determined via the Biot-Savart Law and the right-hand rule to consist of two directional components: one component along the length of the cable, the axial field, and a component normal to the length of the cable, the tangential field [28]. Descriptions of the *B* field components are presented in figure (3.1). Both *B* field components contribute to the total inductance of the cable and are therefore considered in the corresponding inductance calculations.

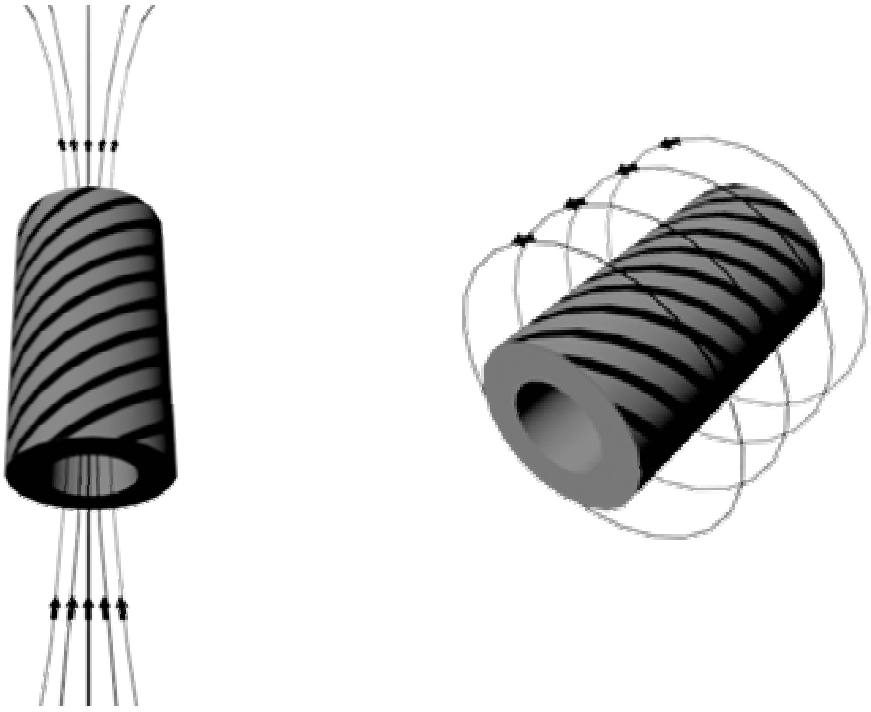

Figure (3.1) Axial (left) and tangential (right) field components resulting from helical winding of conductor.

3.1.1 London Penetration Depth

To account for the distribution of the *B* field inside the thickness of the conductors, the penetration of the *B* field into the HTS tapes was investigated. Unlike conventional conductors, superconductors exhibit the ability to approximately exclude an external *B* field from their interior, effectively becoming perfectly diamagnetic, where the external field is the self-field of the other phases. Known as the Meissner effect [27], this phenomenon causes the HTS tape to behave like a perfect conductor, and occurs when the temperature, T, is less than the critical temperature, T_c, and the external B field is initially zero. Although the resistance is extremely low, superconductors are not perfect conductors in a technical sense. Therefore, external B fields can penetrate the superconducting material into a narrow region called the London penetration depth [29]. According to the London penetration depth, the distance, λ, that the external B field penetrates into the superconducting material is related by the ratio of the material temperature, T, to the critical temperature, T_c, as shown in equation (3.3).

$$\lambda = \frac{\lambda_o}{\sqrt{1-\left(\frac{T}{T_c}\right)^4}} \qquad [m] \qquad (3.3)$$

λ—London penetration depth [m]

λ_o—London penetration depth at 0 K, equal to $5\text{x}10^{-6}$ cm nominally [29].

T—Temperature of superconductor [K]

T_c—Critical temperature of superconductor [K]

For the triaxial cable, if λ << than the thickness of the BSCCO, then the assumption of a perfect conductor is valid and the conductor thickness can be neglected for the calculation of cable inductance. Evaluation of equation (3.3) over a range of temperatures for a typical BSCCO tape with a critical temperature of 104 K is presented in figure (3.2), and reveals that the penetration depth of the B field is approximately λ_o at 77 K, a value

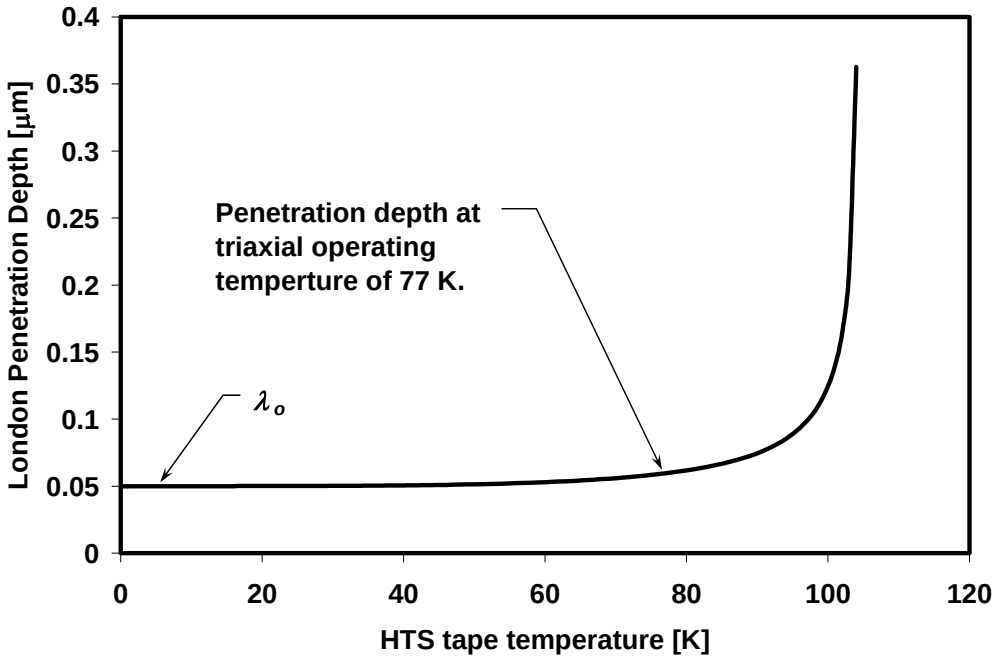

Figure (3.2) London penetration depth of the *B* field into HTS tape.

much smaller than the 100 μm thickness of the BSCCO in a typical HTS tape. Therefore, the penetration of the *B* field into the tape will have little effect on the inductance calculations, so for ease of calculation, the tape thickness can be neglected. However, λ is only valid for the superconducting material, in this case BSCCO. The Ag/alloy matrix material and possible stabilizers that encase the BSCCO filaments are not accounted for, but as analysis will show they have very little effect on the inductance because the thickness of the HTS tapes is small compared to the thickness of the dielectric material between phases. In addition, during steady-state operation all current is expected to flow through the BSCCO, so that the matrix material and other stabilizers do not affect the inductance.

3.1.2 Self Inductance Due to Tangential Fields

The self-inductances due to tangential *B* fields were calculated by analytically applying current in one phase and opening the circuits of the other two phases. To obtain a 3X3 inductance matrix instead of a 6X6, the two layers that compose each phase of the triaxial cable were lumped into one effective phase layer. Since tangential fields in the cable are concentric to the conductor and infinitesimal conductor thicknesses have been assumed, the *B* field resulting from current in a particular phase exists in the area external to that phase. Noting this observation, the self-inductances due to tangential fields were calculated with little difficulty because the internal inductance of the HTS conductors could be neglected. The self-inductance, $L_{t\text{-}i}$, of phase i due to tangential field was then determined by calculating the stored magnetic energy, $W_{m\text{-}i}$ from equation (3.4) [30]. Definitions of the variables used for the calculation the self-inductances due to tangential fields have been provided in table (3.1).

$$W_{m-i} = \frac{1}{2\mu} \int_{Triaxial} B^2 dv \qquad [J] \qquad (3.4)$$

A standard approach for approximating the tangential *B* field of a current-carrying wire is the Biot-Savart Law [31], which associates the loss of field strength to its radial distance, *r*, from the conductor. The resulting magnetic field expression is presented in equation (3.5).

$$B_t = \frac{\mu I}{2\pi r} \qquad [T] \qquad (3.5)$$

The corresponding self-inductance due to tangential fields can then be determined using the conservation of energy principle described in equation (3.6), and is expressed in equation (3.7).

Table (3.1) Variables used in the calculation of the self-inductance due to tangential fields for the triaxial cable.

Variable	Description
B	Magnetic field
B_t	Tangential magnetic field
W_m	Stored magnetic energy
H	Magnetic field intensity
μ	permeability
L_t	Inductance due to tangential fields.
r_i	Mean radius of the i^{th} phase.
r_s	Mean radius of shield
r_{out}	Outer radius of phase conductor.
r_{in}	Inner radius of phase conductor.
I	Phase current

$$W_{m-i} = \frac{1}{2} L_{t-i} I^2 \qquad [J] \tag{3.6}$$

$$L_{t-i} = \frac{\mu}{2\pi} \ln\left(\frac{r_s}{r_i}\right) \qquad \left[\frac{H}{m}\right] \tag{3.7}$$

Since the *B* field occurs only in the dielectric material, equation (3.7) can be rewritten in terms of the permeability of free space as shown in equation (3.8).

$$L_{t-i} = \frac{\mu_o}{2\pi} \ln\left(\frac{r_s}{r_i}\right) \qquad \left[\frac{H}{m}\right] \tag{3.8}$$

If the thickness of the HTS conductor layers is not excluded from the analysis, then the permeability of the conductor materials would have to be accounted for in the internal inductance component. Values of the relative permeability for selected conductor and dielectric materials that compose the triaxial cable are described in table (3.2).

To further validate neglecting the HTS conductor thickness for the calculation of the triaxial self inductances, they were recalculated for a finite HTS conductor thickness and a uniform current density along the phase layer cross-section. An expression for the current distribution along the cross section of phase *i* is expressed in equation (3.9). The magnetic field intensity, H_x, was calculated via Ampere's law [26] as shown in equations (3.10) and (3.11). The composition of the HTS tapes was assumed to be silver, since little about the electromagnetic properties of BSCCO are known. Therefore, the HTS tapes were treated as conventional conductors with extremely low resistance, and the London penetration depth was ignored. The resulting tangential *B* field is expressed in equation (3.12).

Table 3.2 Relative permeability of selected triaxial cable materials.

Material	Relative Permeability
Copper	≈1 [27]
Silver	≈1 [27]
Dielectric	≈1 [27]

$$I_x = \frac{x^2 - r_{in}^2}{r_{out}^2 - r_{in}^2} I_i \qquad [A] \qquad (3.9)$$

x—Radial position within phase conductor thickness.

I_x—Portion of the current distributed along cross-section at distance, x.

r_{out}—Outer radius of phase i.

r_{in}—Inner radius of phase i.

$$\oint H_x ds = I_x \qquad [A] \qquad (3.10)$$

$$H_x = \frac{I_x}{2\pi x} \qquad \left[\frac{A}{m}\right] \qquad (3.11)$$

$$B_x = \mu_o H_x \qquad [T] \qquad (3.12)$$

Substitution of equation (3.9) into equations (3.11) and (3.12) yielded the tangential B field for a particular phase that is a function of the current distribution in the cross section of the cable. The stored magnetic energy was then found using equation (3.4). The resulting self-inductance was calculated using equation (3.6) and is shown in equation (3.13).

$$L_{t-i} = \frac{\mu_o}{2\pi}\left[\frac{r_{out}^2 - 3r_{in}^2}{4\left(r_{out}^2 - r_{in}^2\right)} + \frac{r_{in}^4}{\left(r_{out}^2 - r_{in}^2\right)^2}\ln\left(\frac{r_{out}}{r_{in}}\right) + \ln\left(\frac{r_s}{r_{in}}\right)\right] \qquad \left[\frac{H}{m}\right] \tag{3.13}$$

The first two terms in equation (3.13) represent the inductance due to the internal fields that exists within the thickness of the conductor. The last term represents the inductance due to the external fields, and is the same as the tangential self-inductances from equation (3.8) that assume negligible thickness. A comparison of the self-inductance values due to tangential fields calculated with and without the conductor thickness is given in table (3.3) for the geometric parameters of the 13.2 kV triaxial cable presented in table (1.3). The results in table (3.3) show that the inclusion of conductor thickness has little bearing on the inductance values. Therefore, the assumption that conductor thickness can be neglected was validated for this case. It was noticed that the magnetic flux was slightly less when thickness was considered because not all the current was distributed in the centerline of the conductor cross-section. Therefore, the assumption of negligible thickness produced a more conservative value of inductance.

Table (3.3) Calculated self-inductance values due to the tangential fields of the 13.2 kV HTS triaxial power cable. Inductance values calculated assuming finite and negligible tape thickness are compared.

Phase Conductor	L_t [μH/m] finite	L_t [μH/m] negligible	% difference
Phase A	64.82	65.61	1.22
Phase B	42.66	43.36	1.65
Phase C	22.71	23.34	2.80

3.1.3 Self Inductance Due to Axial Fields

The self-inductances due to the axial component of the *B* fields were estimated using Ampere's law as expressed in equation (3.14), which states that the line integral around any closed contour is proportional to the current passing through it [27]. Since the length of the cable is much greater than its diameter, the axial *B* field within the helical winding of the cable was considered parallel with its length and the field outside the winding was neglected. Therefore, equation (3.14) is valid for analysis of the triaxial cable because it considers this ideal case. If Ampere's law is evaluated over a section of the described solenoid, the *B* field along all paths is equal to zero except for the interior path parallel to cable length, *a*-*b*, as described in figure (3.3) and equations (3.15), (3.16), and (3.17). A description of the variables used in the calculation of the self inductance due to axial fields is presented in table (3.4).

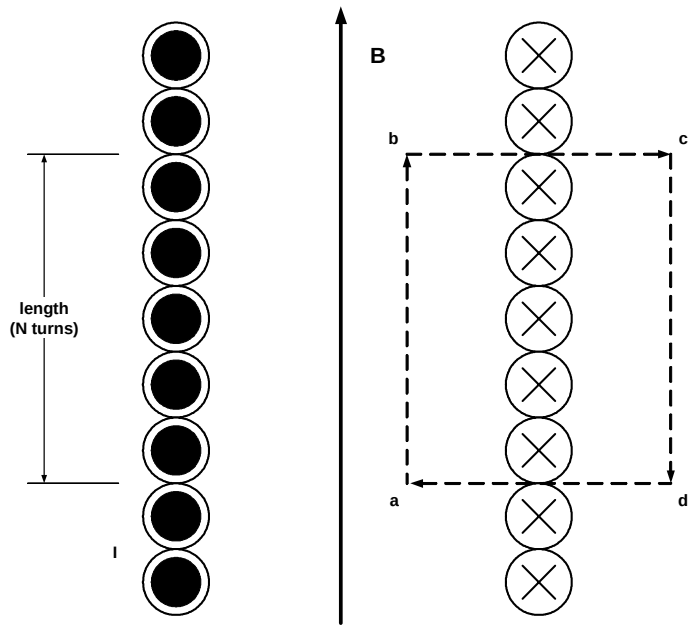

Figure (3.3) Evaluation of Ampere's Law on a solenoid.

Table (3.4) Variables used in the calculation of the self-inductances due to the axial fields of the triaxial power cable.

Variable	Description
B_a	Axial magnetic field
$B_{a\text{-}in}$	Axial field of inner HTS layer in a phase
$B_{a\text{-}out}$	Axial field of outer HTS layer in a phase
W_m	Stored magnetic energy
N	Number of helical HTS tape turns
μ	Permeability
L_a	Inductance due to axial fields
r_i	Mean radius of the i^{th} phase
l	Solenoid length
υ_p	Winding pitch of HTS tape
α	Tape lay angle in degrees. Can be positive or negative depending on the winding direction.
I	Phase current

$$\oint_C B \cdot dl = \mu_o I \qquad \left[\frac{H \cdot A}{m}\right] \qquad (3.14)$$

$$\oint_{abcd} B \cdot dl = \int_{ab} + \underbrace{\int_{bc} + \int_{cd} + \int_{ca}}_{=0} \qquad \left[\frac{H \cdot A}{m}\right] \qquad (3.15)$$

$$\int_{ab} B \cdot dl = \mu_o NI \qquad \left[\frac{H \cdot A}{m}\right] \qquad (3.16)$$

$$B = \frac{\mu_o NI}{l} \qquad [T] \qquad (3.17)$$

If the length, l, of the cable is equal to a unit length, then the turns ratio, N, is inversely proportional to the pitch, υ_p, as shown in equation (3.18). The winding pitch, expressed in equation (3.19), is the length of one turn of the helically wound HTS tape and is dependant on the lay angle, α, and mean radius, r.

$$B = \frac{\mu_o I}{\upsilon_p} \qquad [T] \qquad (3.18)$$

$$\upsilon_p = 2\pi r \tan\alpha \qquad [m] \qquad (3.19)$$

The axial self-inductance, $L_{a\text{-}i}$, was then determined from the stored magnetic energy as in the case of the tangential inductances, and is expressed in equation (3.20) [28].

$$L_{a-i} = \frac{\mu_o \pi}{\upsilon_p^2} \qquad \left[\frac{H}{m}\right] \qquad (3.20)$$

In order to model the triaxial cable using available power systems analysis software packages where only 3X3 parameter matrices are accepted, it was necessary to lump the two layers of HTS tape that compose each phase into one equivalent phase conductor. Since equation (3.20) accounts for only one HTS tape layer per phase, another expression was developed to account for the lay angle of each HTS layer. In order to lump the two conductor layers of each phase into one effective layer, the axial *B* field resulting from each layer, $B_{a\text{-}in}$ and $B_{a\text{-}out}$, was calculated. The total field for each phase was then found by summing these individual HTS tape layer *B* fields as described in equations (3.21) and (3.22). The pitch terms $\upsilon_{p\text{-}in}$ and $\upsilon_{p\text{-}out}$ were inherently positive or negative depending on the sign of the lay angles, which in turn was related to the relative winding directions of the tape layers. For instance, if α_{in} is positive and α_{out} is negative, the total *B* field calculated in equation (3.22) would be smaller than if both were positive. Therefore, the opposing winding directions tend to cancel a portion of the axial *B* field.

$$B_{a-i} = B_{a-in} + B_{a-out} \qquad [T] \qquad (3.21)$$

$$B_{a-i} = \frac{\mu_o \mathrm{I}_{in}}{\upsilon_{p-in}} + \frac{\mu_o \mathrm{I}_{out}}{\upsilon_{p-out}} \quad [T] \qquad (3.22)$$

Assuming that the winding directions and lay angles of the HTS tapes have been optimized for equal current distribution through both layers in each phase, currents I_{in} and I_{out} are set equal and equation (3.22) can be written as equation (3.23).

$$B_{a-i} = \frac{\mu_o I_i}{2}\left(\frac{1}{\upsilon_{p-in}} + \frac{1}{\upsilon_{p-out}}\right) \qquad [T] \qquad (3.23)$$

Application of equations (3.4) and (3.6) to equation (3.23) yields the axial self-inductance due to axial fields, $L_{a\text{-}i}$, of phase *i* as shown in equation (3.24).

$$L_{a-i} = \frac{\mu_o \pi r_i^2}{2}\left(\frac{1}{\upsilon_{p-in}} + \frac{1}{\upsilon_{p-out}}\right)^2 \qquad \left[\frac{H}{m}\right] \qquad (3.24)$$

Evaluation of equation (3.24) yields an expected pattern of self-inductance values due to axial field. For HTS tape layers wound in opposing directions the inductance values are smaller, likewise, they are larger if the tapes are wound in the same direction.

3.2 Mutual Inductance

Mutual inductances were determined by analytically observing the magnetic flux in one phase resulting from the current in another. This flux magnetically links the two circuits together and is therefore called the flux linkage, λ_{ij}. The mutual inductance between two phases was then found by dividing the total flux linkage by its respective current as expressed in equation (3.25).

$$L_{ij} = \frac{\lambda_{ij}}{I_j} \rightarrow I_i = 0 \quad \left[\frac{H}{m}\right] \qquad (3.25)$$

The magnetic flux, Φ_{ij}, produced by current, I_j, was determined by integrating the field produced by phase j, B_j, over the area enclosed by phase i. The resulting magnetic flux is described in equation (3.26).

$$\Phi_{ij} = \int_{s_i} B_j \cdot ds \quad [Wb] \qquad (3.26)$$

In the triaxial cable, the mutual inductance occurs from coiled conductors that consist of multiple turns. Therefore, the total magnetic flux linking phase i to phase j was found by considering the turns ratio, N_{ji}, which the magnetic flux passes through. The total magnetic flux linkage is shown in equation (3.27).

$$\lambda_{ij} = N_i \Phi_{ij} \quad [Wb] \qquad (3.27)$$

The mutual inductance was then found by implementing equation (3.25). Like the self-inductances, the mutual inductances consist of axial and tangential components. The tangential component is presented first since it requires less computational rigor.

3.2.1 Mutual Inductance Due to Tangential Fields

Using equation (3.5) to determine the *B* field produced by phase *j*, the magnetic flux passing into phase *i* was calculated from equation (3.27). The resulting magnetic flux is presented in equations (3.28) and (3.29).

$$\mathbf{\Phi}_{t-ij} = \int_{r_j}^{r_s} \frac{\mu_o \mathbf{I}_j}{2\pi r} dr \quad [Wb] \qquad (3.28)$$

$$\Phi_{t-ij} = \frac{\mu_o I_j}{2\pi} \ln\left(\frac{r_s}{r_j}\right) \quad [Wb] \qquad (3.29)$$

The lower bound of the integral in is r_j because the tangential *B* field resulting from current in phase *j* only exists for $r>r_j$. The total flux linkage was then found from equation (3.27) to be equal to the flux, where the turns ratio is unity because each cylinder is one turn in the case of tangential fields. The resulting mutual inductance, $L_{t\text{-}ij}$, was determined by equation (3.25) and is presented in equation (3.30).

$$L_{t-ij} = \frac{\mu_o}{2\pi} \ln\left(\frac{r_s}{r_j}\right) \left[\frac{H}{m}\right] \quad where \quad i \neq j \qquad (3.30)$$

Since the flux in phase *j* due to a current in phase *i* is also external to phase *j*, $L_{t\text{-}ij}=L_{t\text{-}ji}$, a result that agrees with the Neumann formula for mutual inductance [27, 30].

3.2.2 Mutual Inductance Due to Axial Fields

The mutual inductances due to axial fields were calculated using the same process as described for the tangential components, except that the turns ratio, N_i, is not unity due to differences in radii and lay angles of the conducting layers in each respective phase. Based on equation (3.22), the axial *B* field resulting from current in phase *i* is presented in equations (3.31) and (3.32), where $N_{i\text{-}in}$ is the number of turns of the inner HTS tape layer of phase *i*, and $N_{i\text{-}out}$ is that of the outer layer.

$$B_i = \frac{\mu_o I_i}{2l}\left(N_{i-in} + N_{i-out}\right) \quad [T] \qquad (3.31)$$

$$B_i = \frac{\mu_o I_i}{2l} N_i \quad [T] \quad where \quad N_i = N_{i-in} + N_{i-out} \qquad (3.32)$$

The resulting flux is shown in equation (3.32).

$$\Phi_{ij} = \frac{\mu_o \pi I_i}{2l} N_i r_i^2 \quad [Wb] \qquad (3.33)$$

The flux linkage was found from equation (3.27) and described in equation (3.24) where N_j represents the number of turns of the tape layers in phase *j* for unit length *l*.

$$\lambda_{ij} = N_j \Phi_{ij} \quad [Wb] \quad where \quad N_j = N_{j-in} + N_{j-out} \qquad (3.34)$$

The corresponding mutual inductance was found by taking the number of terms over a unit length. The number of turns could then be related to the winding pitch of the tapes as expressed in equation (3.35).

$$L_{a-ij} = \frac{\mu_o \pi}{2}\left(\frac{1}{\upsilon_{i-in}} + \frac{1}{\upsilon_{i-out}}\right)\left(\frac{1}{\upsilon_{j-in}} + \frac{1}{\upsilon_{j-out}}\right) r_i^2 \quad \left[\frac{H}{m}\right] \quad where \quad i \neq j \qquad (3.35)$$

Since flux in phase *j* due to a current in phase *i* exists only for $r<r_i$, $L_{a\text{-}ij}=L_{a\text{-}ji}$ and Neumann's formula is again satisfied.

3.3 Effective Inductance

From the axial and tangential components calculated, the total effective inductance of the triaxial cable was found by adding both components as described in equation (3.36).

$$L_{effective} = L_a + L_t \quad \left[\frac{H}{m}\right] \qquad (3.36)$$

The following pair of equations provides a complete description of the mutual and self inductance parameters of the triaxial cable, where equation (3.37) yields the self inductance and equation (3.38) yields the mutual inductance.

$$L_{ij} = \frac{\mu_o \pi}{2}\left(\frac{1}{\upsilon_{i-in}} + \frac{1}{\upsilon_{i-out}}\right)^2 r_i^2 + \frac{\mu_o}{2\pi}\ln\left(\frac{r_s}{r_i}\right) \quad \left[\frac{H}{m}\right] \quad where \quad i = j \qquad (3.37)$$

$$L_{ij} = \frac{\mu_o \pi}{2}\left(\frac{1}{\upsilon_{i-in}} + \frac{1}{\upsilon_{i-out}}\right)\left(\frac{1}{\upsilon_{j-in}} + \frac{1}{\upsilon_{j-out}}\right) r_i^2 + \frac{\mu_o}{2\pi}\ln\left(\frac{r_s}{r_i}\right) \quad \left[\frac{H}{m}\right] \quad where \quad i \neq j \qquad (3.38)$$

Inductance values for the 13.2 kV triaxial cable were attained from evaluation of these equations with the parameters given in table (1.3) and are presented in equation (3.39)

$$L' = \begin{vmatrix} 70.20 & 41.67 & 24.37 \\ 41.67 & 44.14 & 22.97 \\ 24.37 & 22.97 & 23.70 \end{vmatrix} \left[\frac{nH}{m} \right] \qquad (3.39)$$

3.4 Effective Capacitance

The capacitance parameters of power cables are usually determined through observation of the electric fields, or *E* fields, that are generated by the cable in the cross-section. For most power cable applications, the *E* field radiates from the conductors outwardly in a direction normal to the axis of the conductor. In the case of the triaxial cable, observation of the *E* fields associated with the helical winding of the conductor may prove to be a difficult task because more than one component of the *E* field may exist. Unfortunately, the capacitance could not be calculated by relating it to the cable inductance expressed in equation (3.40) because it is valid only for transverse electromagnetic (TEM) transmission lines [26], and the triaxial cable is not a TEM line due of the presence of an axial field component. Because little about the electric field orientations are known in the triaxial cable, the capacitances were found by assuming the more conventional case; that the electric fields are normal to the conductor axis in a radial direction. Therefore, the helical winding of the HTS tape was ignored and the phases were observed as three concentric cylinders. The corresponding capacitances were calculated using a conventional method [23] that has been used in a previous triaxial

$$L'C' = \mu\varepsilon \qquad (3.40)$$

μ—Permeability of the conductor.

ε—Permittivity of the dielectric material.

L'—Inductance matrix.

C'—Capacitance matrix.

cable study [32]. First, the capacitance components were calculated by observing the electric field between the conducting layers as expressed in equations (3.41), (3.42), and (3.43). Since the relative permittivity of the dielectric material, Cryoflex™, was not available, an assumed value of 2.6 was used based on the value of Kapton.

$$C_{12} = \frac{2\pi\varepsilon}{\ln\left(\frac{r_{2-in}}{r_{1-out}}\right)} \quad \left[\frac{F}{m}\right] \tag{3.41}$$

$$C_{23} = \frac{2\pi\varepsilon}{\ln\left(\frac{r_{3-in}}{r_{2-out}}\right)} \quad \left[\frac{F}{m}\right] \tag{3.42}$$

$$C_{34} = \frac{2\pi\varepsilon}{\ln\left(\frac{r_{s-in}}{r_{3-out}}\right)} \quad \left[\frac{F}{m}\right] \tag{3.43}$$

ε—Permittivity of dielectric material.

$r_{1\text{-}out}$—Outer radius of phase A.

$r_{2\text{-}in}$—Inner radius of phase B.

$r_{2\text{-}out}$—Outer radius of phase B.

$r_{3\text{-}in}$—Inner radius of phase C.

$r_{3\text{-}out}$—Outer radius of phase C.

$r_{s\text{-}in}$—Inner radius of copper shield.

The capacitance matrix was then found using equation (3.44).

$$C' = \begin{vmatrix} C_{12} & -C_{12} & 0 \\ -C_{12} & C_{12}+C_{23} & -C_{23} \\ 0 & -C_{23} & C_{23}+C_{34} \end{vmatrix} \quad \left[\frac{F}{m}\right] \qquad (3.44)$$

Evaluation of these equations for the 13.2 kV triaxial cable with specifications presented in table (1.3) provide the capacitance values for the cable under study and are expressed in equation (3.45).

$$C' = \begin{vmatrix} 1.625 & -1.625 & 0 \\ -1.625 & 3.432 & -1.806 \\ 0 & -1.806 & 3.410 \end{vmatrix} \quad \left[\frac{nF}{m}\right] \qquad (3.45)$$

A simple check was made to see if these capacitance values were reasonable for the triaxial cable. The cable capacitances were recalculated using equation (3.40) with the tangential field inductance components only. The corresponding values of capacitance matched exactly those in equation (3.45). Therefore, the assumption of a TEM line is a reasonable one in this case, because the inductances due to axial fields are small relative to those due to tangential fields.

Chapter 4

Effective Resistance of the Triaxial Cable

Unlike conventional conductors, superconductors possess virtually zero resistance. When a DC current less than the critical current is applied to a superconductor, little or no voltage is generated across it because electrons are allowed to travel unimpeded in the material lattice. However, when AC currents or time-varying magnetic fields are applied, first generation superconductors like HTS BSCCO tapes exhibit heat losses that are described as AC loss [33]. Alternating current losses are of particular interest in applications like HTS power cables, where applied AC currents result in time-varying magnetic fields that exist parallel to the surface of the tape. Ohmic losses are also generated by these superconductors, and are associated with the transition of the conductor from the superconducting to the normal state of operation. These ohmic losses are referred to as transport losses because the transport current flows through the resistive matrix material. Both of these loss components are dynamic and non-linear due to their dependence on the applied current and the critical current, I_c, which is a function of both temperature and applied magnetic field. Generally, the I_c of superconductors degrades as temperature and applied B field increase [3], which leads to a further increase of heat loss. Based on these loss mechanisms, this chapter will focus on the development of an effective resistance for use in the lumped parameter cable model, which is described in equation (4.1) as the series combination of the transport resistance and the AC resistance.

$$R_{eff} = R_{transport} + R_{AC} \quad \left[\frac{\Omega}{m}\right] \qquad (4.1)$$

This effective resistance was calculated as a function of the transport current so that it can be represented as a type-99 non-linear resistance element in ATP. For the scope of this study, the temperature of the cable was assumed constant throughout operation and

applied fields were neglected. These assumptions will simplify the analysis and reduce the complexity of the model with minimal loss of operational integrity.

4.1 Alternating Current Resistance

Alternating current loss, or magnetization loss, is a result of the nonlinear electromagnetic behavior of the HTS tapes. Although too small to have any effect on the driving sources, the AC loss does generate enough heating in applications to cause an appreciable heat source. Therefore, the ac loss is an important design parameter because it specifies how much additional cooling is necessary to maintain optimal HTS performance. During steady-state operation under rated conditions, the ac loss contributes a small resistive component to the effective resistance of the cable.

4.1.1 Sources of AC Loss

When an alternating field is applied to a superconductor, several phenomena occur within the HTS tape that results in generated watt loss. The phenomena most influential in HTS power cables are hysteretic loss, coupling loss, and eddy current loss [20, 34]. Hysteretic loss occurs due to reversible fluxoid motion caused by penetration of the changing magnetic field lines from the outer surface of the tape into the interior [6, 35]. The changing flux causes alteration of the current density of the tape near the outer surface first then gradually alters the most interior portions. Coupling loss occurs as the magnetic field penetrates into the HTS tape, causing localized induced screening currents that attempt to block the flux in accordance with the Meissner effect [27]. In order to maintain an average zero voltage across the tape, the localized voltages resulting from the screening currents must be cancelled via cross currents in the matrix material in accordance with Kirchoff's voltage law. These cross currents, or coupling currents, couple the filaments together and generate ohmic loss as they flow throughout the

resistive matrix. A description of the screening and coupling currents are presented in figure (4.1). The eddy current loss is caused by locally induced eddy currents in the Ag/alloy or other matrix material, but some studies have shown that such eddy current losses are very small for power frequencies [34, 36], thus making them negligible in HTS power cables.

4.1.2 Modeling AC Loss

Ever since the potential of superconductors for use in electromagnets and other applications were realized, AC losses have been the focus of numerous studies that attempt to understand their origins and explain their behavior [35, 37]. The accomplishment of such studies has rendered mathematical models that describe the AC loss of superconductors under various conditions. Generally, these AC loss models are mathematically extensive and conceptually complicated to understand without strong knowledge of the physics that drives them. Such AC loss models have been modified to describe HTS power cables and have been used in studies that model the current distribution within these cables. Most of the AC loss models that describe HTS cables are

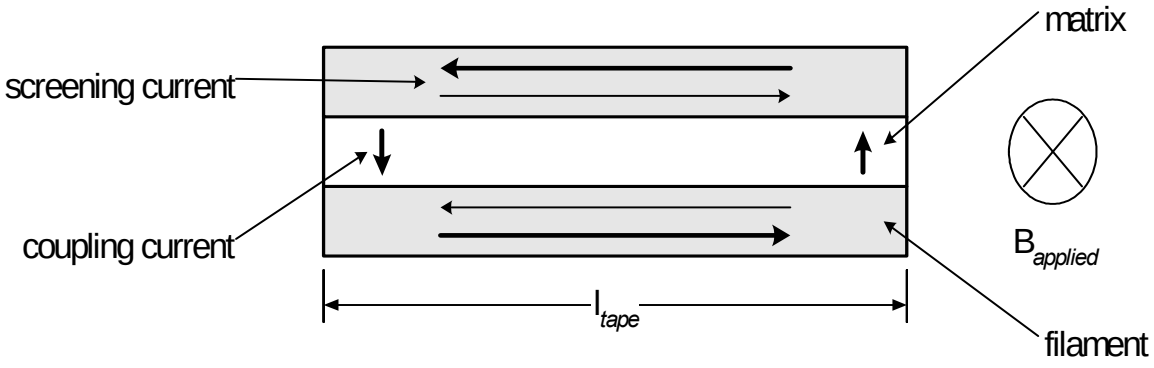

Figure (4.1) Coupling and screening currents within two filaments of HTS tape.

typically constructed for specific cable designs [16, 18, 34]. Fortunately, there is a model available that can describe HTS power cables called the monoblock model that is much easier to implement than other AC loss models, and has good correlation to experimental AC loss measurements [36, 17]. The monoblock model assumes a multi-filamentary thin superconducting tube that produces a purely tangential field at the surface, with a transport current that penetrates from the outer surface to the interior. A description of the monoblock model is presented in figure (4.2). Unlike other AC loss models, the monoblock model is convenient for use in power cable design because it can approximate AC loss for each conducting layer using one expression. The expression describing the monoblock model is presented in equations (4.2) and (4.3).

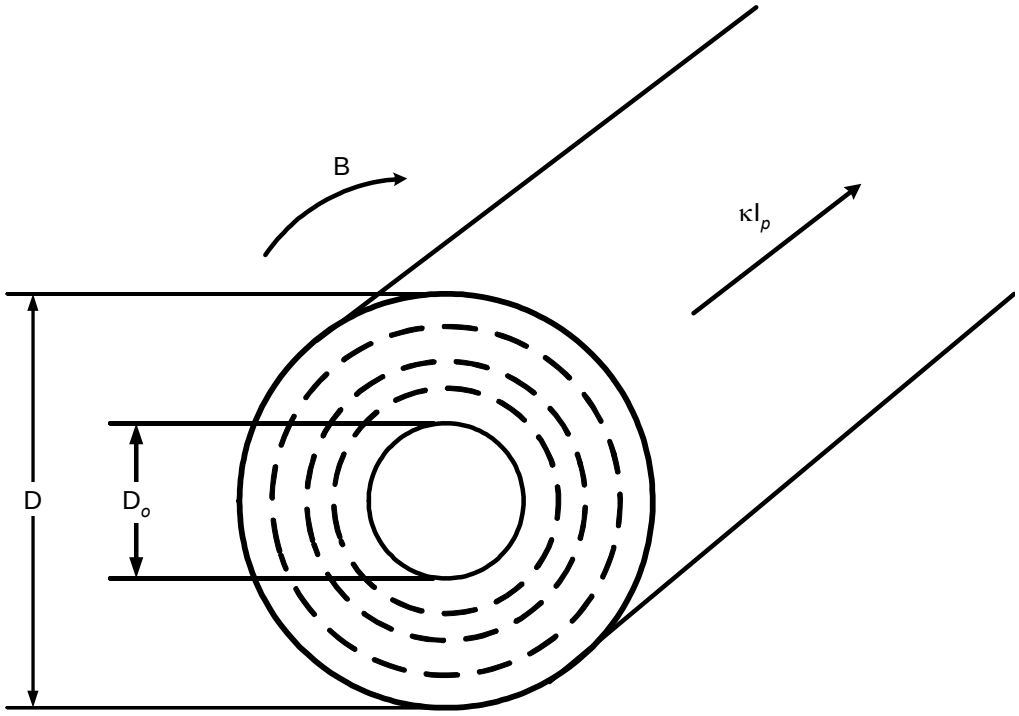

Figure (4.2) Superconducting monoblock tube with superconducting filaments.

$$W_{ac} = \frac{\mu_o f}{2\pi} \kappa \frac{I_c^2}{h^2} \left[(2 - Fh) Fh + 2(1 - Fh) \ln(1 - Fh) \right] \quad \left[\frac{W}{m} \right] \tag{4.2}$$

$$where, \quad h = \frac{D^2 - D_o^2}{D^2}, \quad F = \frac{I_p}{I_c} \tag{4.3}$$

I_p—Peak current per HTS tape.

κ—Number of tapes per phase.

D_o—Inner diameter of phase conductor.

D—Outer diameter of phase conductor.

f—Operating frequency (60 Hz).

There are some drawbacks of the monoblock model that need consideration. First, the monoblock model is valid only for $I_p \leq I_c$, so proper representation of the AC loss has to be considered for the normal operation of the cable. Second, the monoblock model is not an ambitious AC loss model, meaning that improvements in HTS materials and other possible enhancements to HTS tapes are not considered. For instance, coupling losses are improved when the filaments within HTS tapes are twisted [38], but the monoblock model assumes that the HTS filaments are straight. However, the monoblock model does provide a good approximation to the AC losses measured from previous HTS power cable designs measured in the laboratory, including a 5 meter-long triaxial cable tested at ORNL [39]. The AC losses of a 1.5 m triaxial cable were measured using a caliometric method [38], then compared to an approximation using the monoblock model. The comparison of the measured losses to the monoblock model is presented in figure (4.3), where the losses shown represent the combined losses of the three concentric phases. Approximations of the AC loss for each phase of the 13.2 kV triaxial cable are presented in figure (4.4).

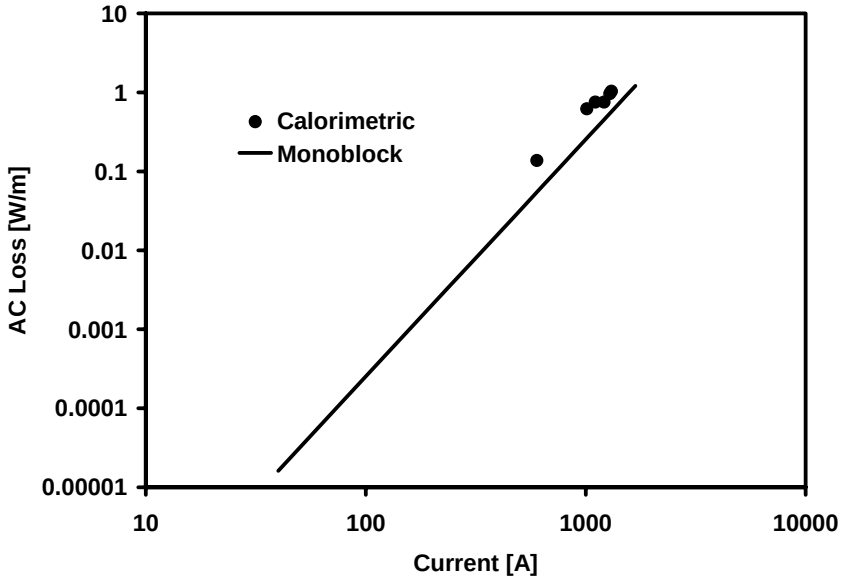

Figure (4.3) AC loss of a 5 m triaxial cable tested at ORNL.

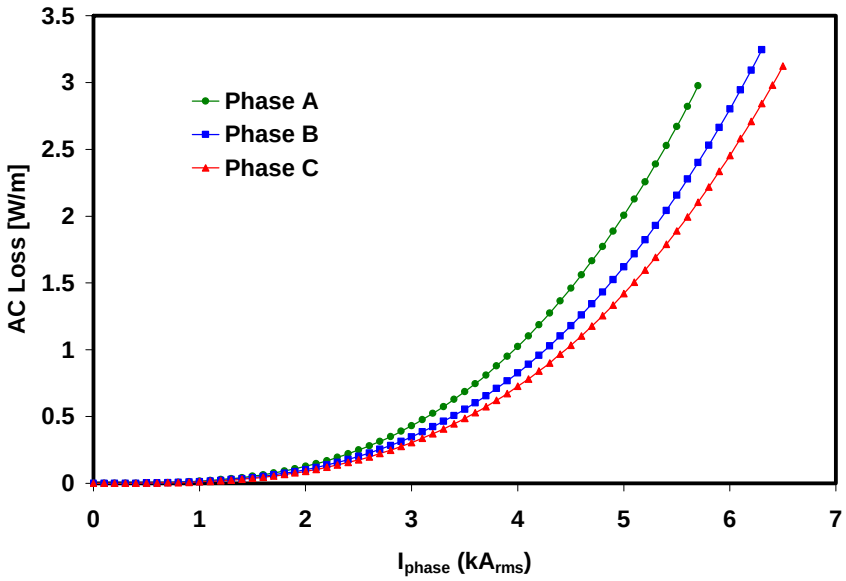

Figure (4.4) Approximated AC loss of a 13.2 kV triaxial cable using the monoblock model.

4.1.3 Effective AC Resistance

Due to its ease of use for engineering purposes of approximating the AC loss, the monoblock model was used to find the effective AC resistance, R_{ac}, for the triaxial cable model under study. To facilitate the requirements of the triaxial cable model, $R_{ac,}$ was approximated for each phase by dividing the AC loss, W_{ac}, by the square of the peak transport current, using equation (4.4), where $I_{p\text{-}transport}=\kappa I_p$ or the peak phase current in the case of this study.

$$R_{ac} = \frac{W_{ac}}{I_{phase}^2} \qquad \left[\frac{\Omega}{m}\right] \qquad (4.4)$$

Approximations to equation (4.4) are presented in figure (4.5) for each phase of the triaxial cable in the range $I_p \leq I_c$. In the described region of operation, the effective AC

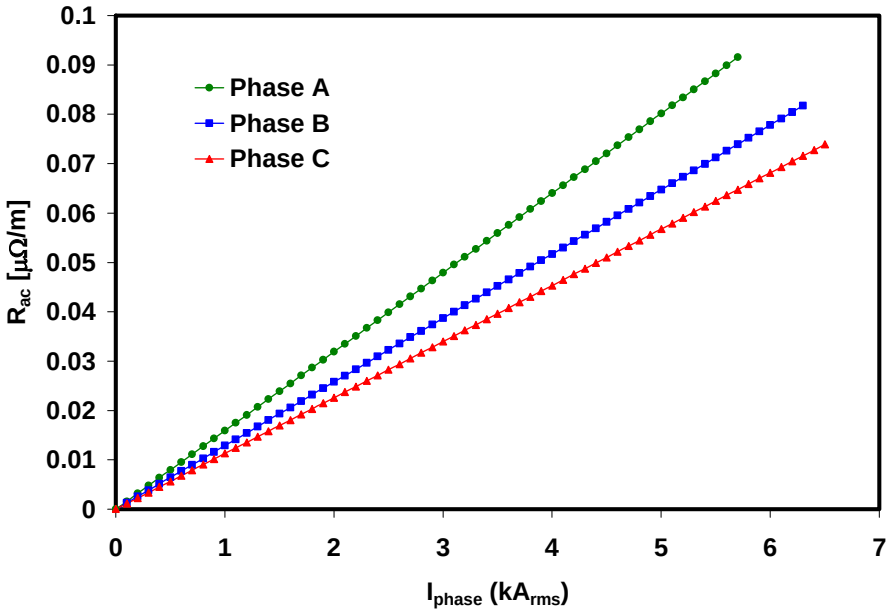

Figure (4.5) Calculated AC resistance of a 13.2 kV triaxial cable.

resistance appears linear with respect to current as the approximated AC losses are proportional to the cube of the transport current, a result that has strong correlation with previous studies [28]. The inclusion of R_{ac} into the model is useful because it provides a finite value of resistance within the superconducting range of operation, as opposed to using the ideal value of zero which may lead to execution errors in ATP and other power system analysis software. Although not an ambitious model, the monoblock model is a practical approximation of the AC loss in the triaxial cable because it correlates with laboratory testing.

4.2 Transport Resistance

The transport resistance, $R_{transport}$, represents the effective resistance due to transport loss. As previously stated, the transport losses are associated with the normal operation of the superconductor, and are described by the transition of current from the superconductor into matrix material. A better explanation of the normal operation of BSCCO tapes can be made by observing their V-I relationship. Such a relationship is presented in figure (4.6) for a BSCCO Ag/alloy HTS tape, and was obtained experimentally by applying a DC current ramp to the tape in a liquid nitrogen bath. The critical current, I_c, was measured by observing tape voltage across a known distance and applying the 1μV/cm criterion [40]. Observing figure (4.6), the potential across the voltage taps is virtually zero for $I<I_c$, but for $I>I_c$, the curve makes a sharp transition into the normal region of operation. In this region of operation, the tape becomes purely resistive and small changes of current result in large changes of voltage. An expression describing the potential of a HTS material along its length is presented in equation (4.5) and is valid for both modes of operation [40].

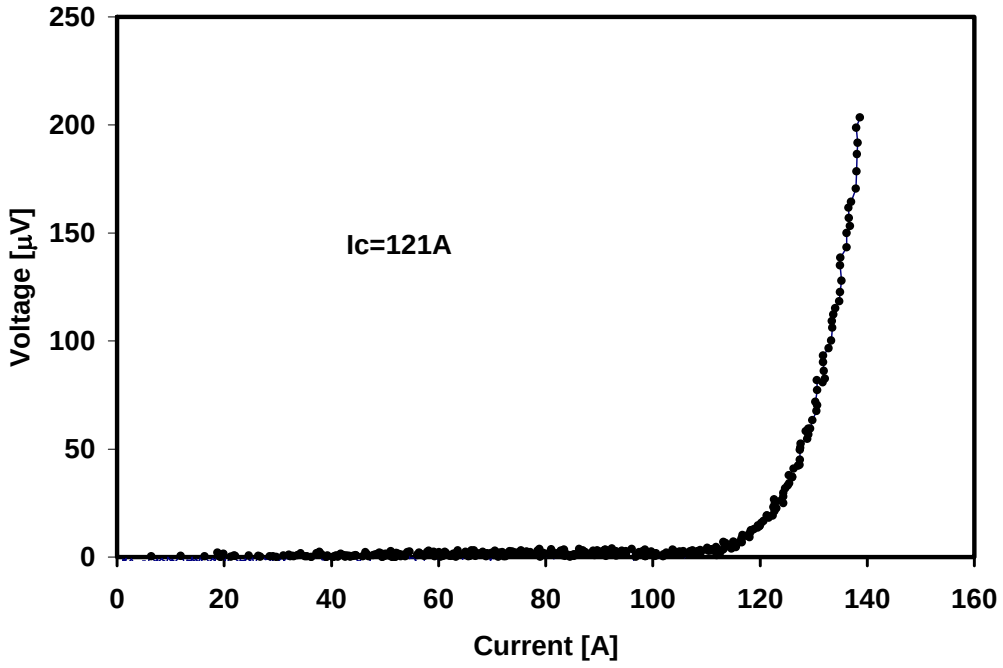

Figure (4.6) V-I relationship of a BSCCO Ag/alloy HTS tape manufactured by American Superconductor Corporation measured at ORNL.

$$V_{HTS} = E_o \left(\frac{I_{HTS}}{I_c} \right)^n \qquad \left[\frac{V}{m} \right] \qquad (4.5)$$

V_{HTS}—Superconductor voltage.

I_{HTS}—Superconductor DC current.

E_o—Critical electric field corresponding to 1 μV/cm.

For obvious reasons, it is more desirable for applications to operate in the superconducting mode where heat losses are almost zero. However, in cable applications faults and other perturbations occur that introduce large currents into HTS tape conductors. These currents can be many times I_c and will cause the HTS conductors to operate in the normal mode, potentially producing large thermal gradients that can

damage the conductors. To prevent such damage from occurring, HTS tapes are manufactured with electrical stabilizers that can conduct these large currents for a finite amount of time. These stabilizers can be made from several electrically conductive materials, depending on the application. In general, HTS tapes usually consist of filaments of superconductor material surrounded by a metal/alloy matrix. There are many possible HTS tape/stabilizer combinations, but the most general case for present HTS power applications is BSSCO superconductor in an Ag/alloy matrix. Such an HTS tape topology was described in chapter 2 and is presented in figure (4.7), which describes the cross-section of a BSCCO Ag/alloy tape. The depiction of a BSCCO HTS tape in figure (4.7) is not precisely accurate because the filaments are very small compared to the cross-sectional area and the number of filaments are actually much larger. However, figure (4.7) provides a broad generalization of the material and geometrical composition of BSCCO HTS tapes in general. If a transport current in the BSSCO becomes large enough such that $I>I_c$, it will be shared with Ag/alloy matrix material and the overall heat losses generated will be mitigated for a small fraction of time until grid contingencies are

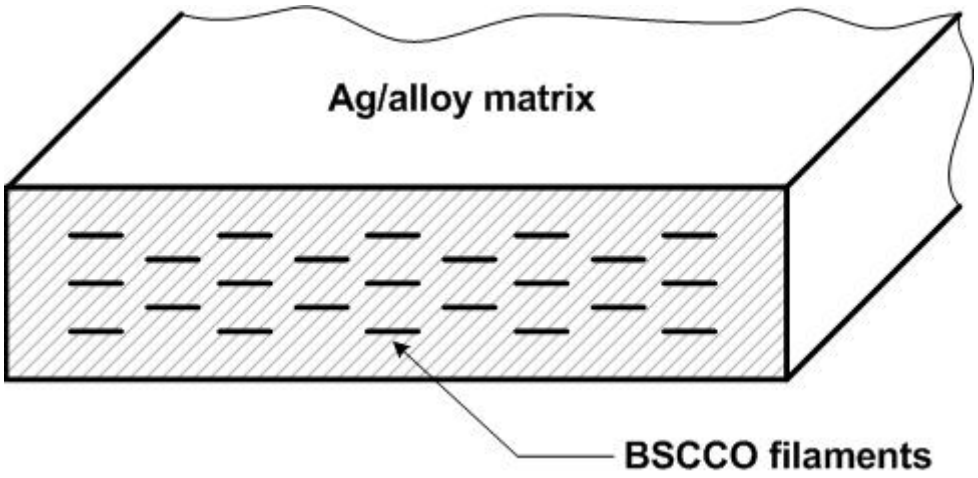

Figure (4.7) Cross-section of a BSCCO Ag/alloy HTS tape.

activated. Safety mechanisms of this nature are of great importance for the design of HTS power cables because they can prevent serious damage from overloading or fault currents.

4.2.1 HTS Tape Current Sharing

The dynamic transition of current from the HTS material into the stabilizer has been the topic of much study and can be investigated by two models; the critical state model and the flux flow model [38, 41]. Due to its simplicity and basic conception, the critical state model will be discussed first. The critical state model assumes an abrupt transition from the superconducting to the normal region at $I=I_c$. Therefore, when I_c is exceeded, all current greater than I_c flows through the matrix material and $R_{transport}$ can be described by equation (4.6).

$$\begin{aligned} R_{transport} &= 0, & I < I_c \\ R_{transport} &= R_{matrix}, & I > I_c \end{aligned} \quad \left[\frac{\Omega}{m}\right] \tag{4.6}$$

Where, I, is the transport current and, R_{matrix}, is the resistance of the matrix material obtained from experimental measurements. However, in application, BSCCO filaments can conduct current greater than I_c, an effect not accounted for in the critical state model.

The flux flow model accounts for this simultaneous sharing of current between the HTS and the matrix material by assuming a more gradual transition from the superconducting state to the normal state of operation. This gradual transition of operational state is achieved through the realization of the parallel resistance combination of R_{matrix} and R_{HTS} as described in equation (4.7).

$$R_{transport} = \frac{R_{HTS} R_{matrix}}{R_{HTS} + R_{matrix}}, \qquad for\ all\ I \qquad \left[\frac{\Omega}{m}\right] \tag{4.7}$$

For the HTS tape modeled in this study, the HTS material is BSCCO, hence R_{HTS} will be referred to as R_{BSCCO} from this point and is described by equation (4.8).

$$R_{BSCCO} = \frac{E_o\left(\frac{I_{BSCCO}}{I_c}\right)^n}{I_{BSCCO}} \qquad \left[\frac{\Omega}{m}\right] \qquad (4.8)$$

From equations (4.7) and (4.8) it can be observed that for $I<I_c$, $R_{transport}$ is very small and when $I>>I_c$, R_{BSCCO} becomes very large such that $R_{transport}=R_{matrix}$, results that correlate with the critical state model. However, for a finite range of transport current just greater than I_c, R_{BSCCO} and $R_{transport}$ approach the same order of magnitude and the transport current is distributed through both materials simultaneously. Calculated profiles of the transport resistance and transport current distribution in a nickel-plated, Ag/alloy, BSCCO HTS tape are presented in figures (4.8) and (4.9) as a function of temperature and constant current.

As previously mentioned, I_c decreases with increasing temperature, so if current is held constant R_{BSCCO} increases in accordance with equation (4.8). Likewise, if temperature is held constant and the transport current increases, R_{BSCCO} increases as I_c is exceeded. This relationship is useful in the absence of a thermal process that determines HTS tape temperatures. The flux flow model can provide valuable insight to HTS cable designers as to what kind of electrical stabilizers can help protect the integrity of the HTS conductors against fault currents or other extreme operating conditions. Therefore, for the purpose of this study, the flux flow model will be used due to its ability to consider electrical stabilizers and because data is readily available.

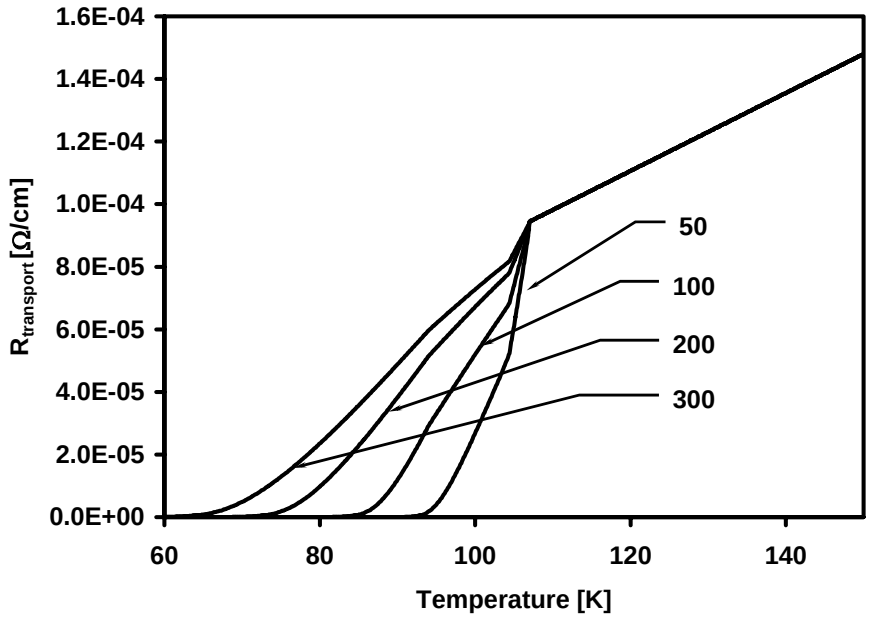

Figure (4.8) Transport resistance of a BSCCO HTS tape for constant transport current.

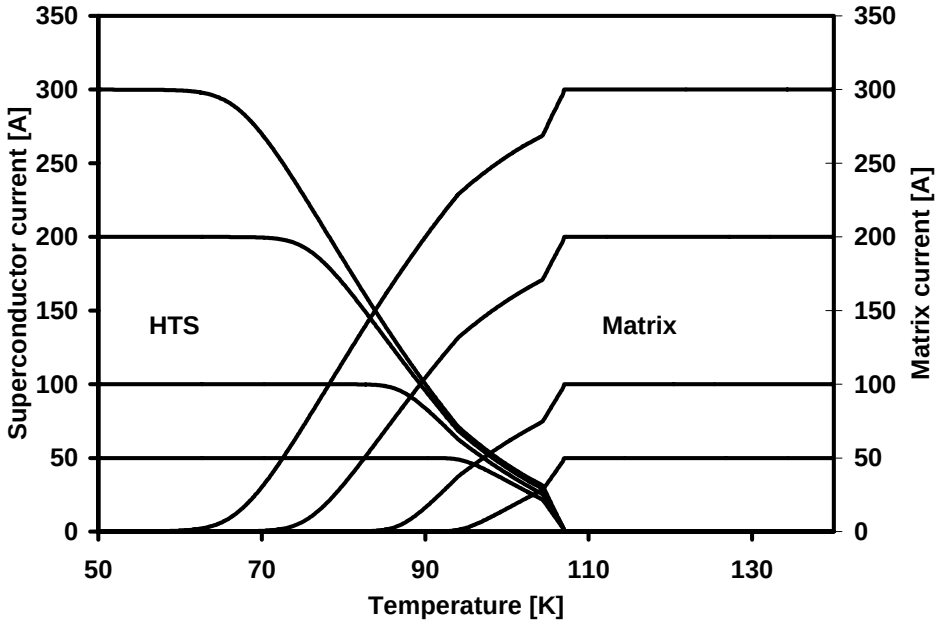

Figure (4.9) Current distribution of a BSCCO HTS tape for various transport currents.

4.2.2 Matrix Resistance

Although calculation of the transport losses via the flux flow model may appear simple according to equation (4.7), acquiring values for R_{BSCCO} and R_{matrix} requires some work. The matrix resistance was obtained by measuring the voltage drop across a known distance of a sample tape when a small transport current, approximately 1 mA, is applied. To acquire resistance as a function of temperature, the sample was cryogenically cooled to $T=T_c$ using a cryogenic refrigerator and the tape voltage was observed for a constant current until the tape assumed ambient temperature. The resulting resistance curve was linear with respect to temperature for ranges of interest in applications and was valid for $T_c<T<T_{ambient}$. To obtain the matrix resistance for $T<T_c$, the curve was extrapolated down as shown in figure (4.10).

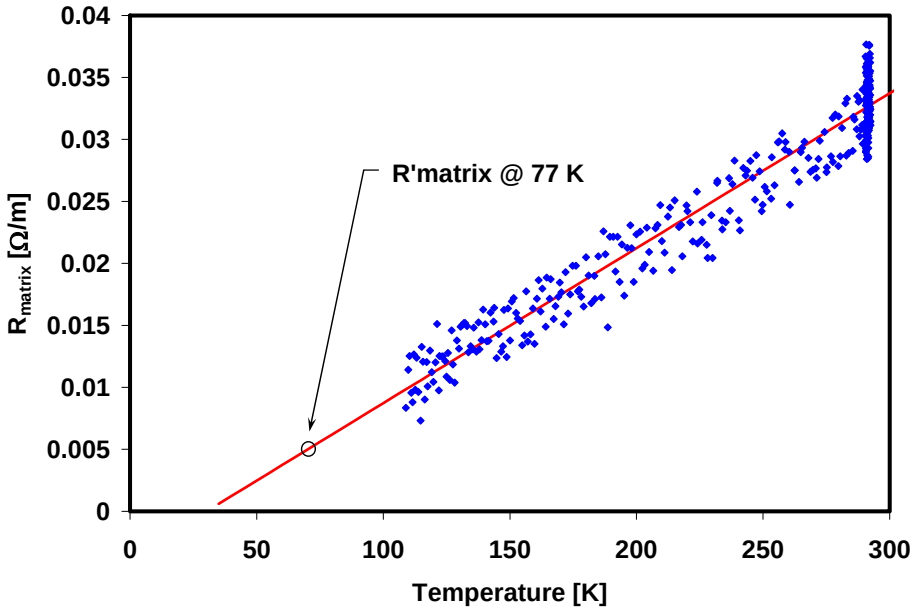

Figure (4.10) Measured matrix resistance of an HTS tape with Ag/alloy sheath.

For this study, the matrix resistance value corresponding to the temperature of liquid nitrogen, 77 K, was of interest since temperature was assumed to remain constant in the model. However, the measured resistance obtained was the matrix resistance of an individual tape and not that of the bundled layers that compose the phases, which consists of many tapes. Equation (4.8) shows that since the tapes in a phase are in parallel, R_{matrix} is simply the measured matrix resistance of a single tape divided by the number of tapes in the particular phase [20].

$$R_{matrix} = \frac{R'_{matrix}}{N} \qquad \left[\frac{\Omega}{m}\right] \tag{4.9}$$

4.2.3 BSCCO Resistance

The resistance of the BSCCO was approximated using the parallel resistance relationship described in equation (4.7) and some numerical computation. From equation (4.8), it is shown that R_{BSCCO} is a nonlinear function of I_{BSCCO}, therefore, I_{BSCCO} has to be determined before R_{BSCCO} can be calculated. Figure (4.11) describes the parallel resistance arrangement discussed in this study. To find I_{BSCCO}, the voltages are equated in accordance with Kirchoff's Voltage law as presented in equation (4.10).

$$I_{matrix}R_{matrix} = I_{BSCCO}E_o\frac{\left(\frac{I_{BSCCO}}{I_c}\right)^n}{I_{BSCCO}} \tag{4.10}$$

Observing figure (4.11), I_{matrix} can be expressed in terms of I_{BSCCO} and $I_{transport}$ as shown in equation (4.11).

$$I_{matrix} = I_{transport} - I_{BSCCO} \qquad [A] \tag{4.11}$$

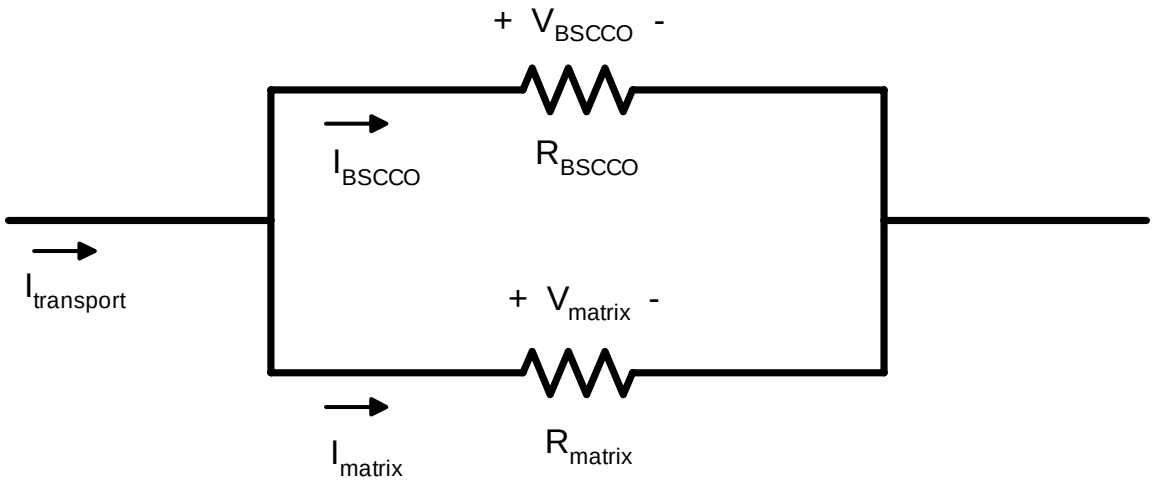

Figure (4.11) Parallel resistance diagram of the matrix material and the BSCCO.

Cancellation of terms and application of equation (4.11) to equation (4.10) yields solvable relationship for I_{BSCCO} and is presented in equation (4.12).

$$E_o\left(\frac{I_{BSCCO}}{I_c}\right)^n = \left(I_{transport} - I_{BSCCO}\right)R_{matrix} \qquad (4.12)$$

Evaluation of equation (4.12) required numerical methods to solve for I_{BSCCO}. Since the region of applicable solutions is known, $0 < I_{BSCCO} < I_{transport}$, a bisection method was used to approximate numerically I_{BSCCO} [42]. Then, R_{BSCCO} and R_{matrix} were known and $R_{transport}$ could be determined.

4.3 Effective Resistance

The effective resistance, R_{eff}, was calculated from equation (4.1) after all of the component resistances were approximated. Since the AC resistance is valid only for $I_p<I_c$ as described by the monoblock model, its value outside this region was approximated to be constant corresponding to the AC loss at I_c. To validate the constant R_{ac} approximation for $I>I_c$, an assumption was made that the transport losses dominate this range of operation due to the exponential nature of the V-I curve. The resulting effective resistance curves are presented in figure (4.12) and (4.13). As described in figure (4.13), the effective resistance approaches a threshold corresponding to the value of R_{matrix} at 77 K with increasing transport current. The reason for this threshold was the constant temperature of the cable assumed by the cable model. Inclusion of a thermal process

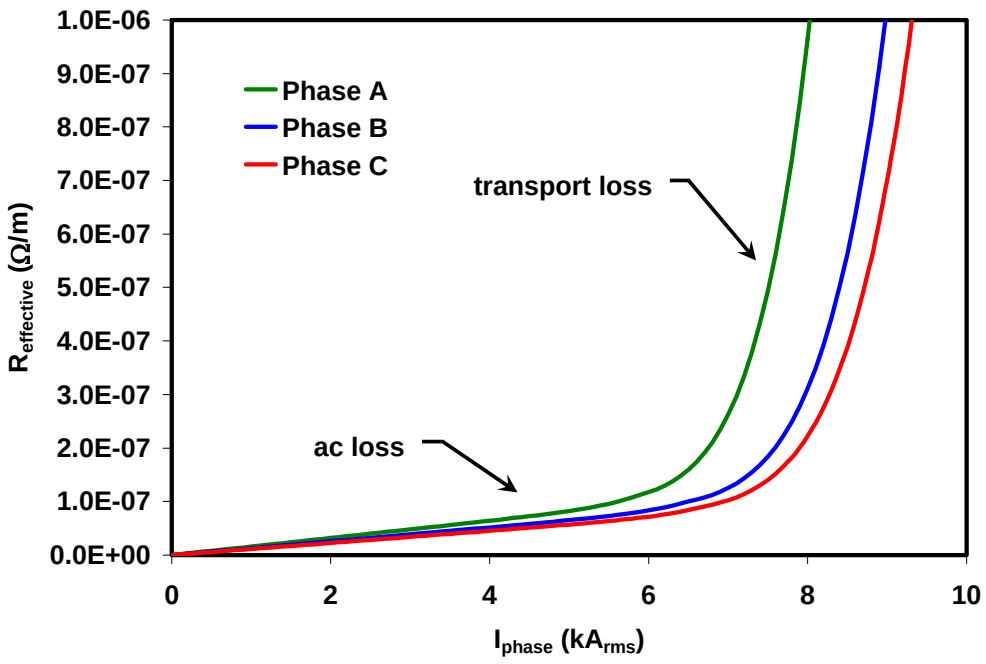

Figure (4.12) Effective resistance of a 13.2 kV triaxial cable. Plot has been enlarged so that the AC losses can be observed.

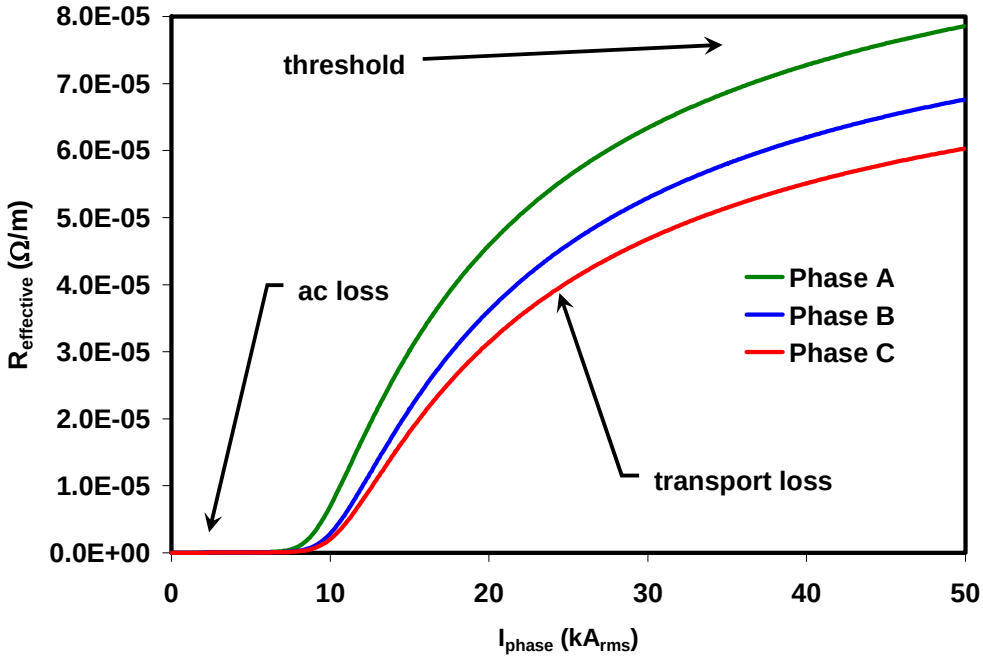

Figure (4.13) Effective resistance of a 13.2 kV triaxial cable for currents up to 50 kA peak.

would cause this limit to climb linearly with temperature. Calculation of the effective resistance was performed using Matlab™. The type-99 non-linear resistance element in ATP requires V-I data in table format, so Matlab™ was also used to convert the calculated effective resistance values into effective voltages via ohm's law. The corresponding Matlab™ files "triaxresist" and "triaxresistvolt" are included in Appendix B.

Chapter 5

Simulation and Results

Simulation of the HTS triaxial power cable in a simple power system was performed using ATP. Steady-state simulations representing the most balanced operating case were made on a 16 km-long triaxial cable by subjecting the EC model to conditions such that rated current would flow at the rated voltage. The electrical imbalance was then measured as a function of line distance. Transients were simulated by subjecting the EC model to various fault scenarios and measuring resulting cable currents. The EC model simulated in this study was configured for an HTS triaxial power cable with a cross-section as shown in figure (1.9) and ratings of 13.2 kV, 3 kA, 69 MVA. A description of the system configuration and the simulation results are included in this chapter.

5.1 Steady-State Analysis

The electrical imbalance of the triaxial cable was investigated by simulating the compiled EC model under rated conditions in ATP. This electrical imbalance was measured at several points along the length of the cable to observe what line lengths may be practical for utility applications.

5.1.1 Steady-State System Configuration

Configuration of the system for steady-state operation was set to achieve rated conditions on the power cable. The source end of the cable was connected to a 13.2 kV, 3-phase generator and the load end was connected to a balanced 3-phase, resistive load. The copper shield was grounded at the endpoints to simulate conditions at the Bixby

substation. The triaxial cable was represented by the user-defined element, SUPc, as described in chapter 2, with the resistive component set to a constant nominal value corresponding with the rated current. Since the steady-state operation of the cable was at rated current, the superconducting layers operated in the superconducting mode so that the cable resistance was due only to AC loss. Therefore, the resistance used for the simulations of the cable in steady-state was that corresponding to AC loss, R_{ac}, at the rated current. To simulate cable characteristics as a function of line distance for a 16 km cable, ten SUPc elements where cascaded in a series configuration with voltage and current probes positioned at each node. A further description of the steady-state system configuration is presented in figure (5.1).

5.1.2 Steady-State Simulation

Steady-state simulation of the power system was accomplished by setting the balanced resistive load so that the largest current flowing in any phase was approximately the rated

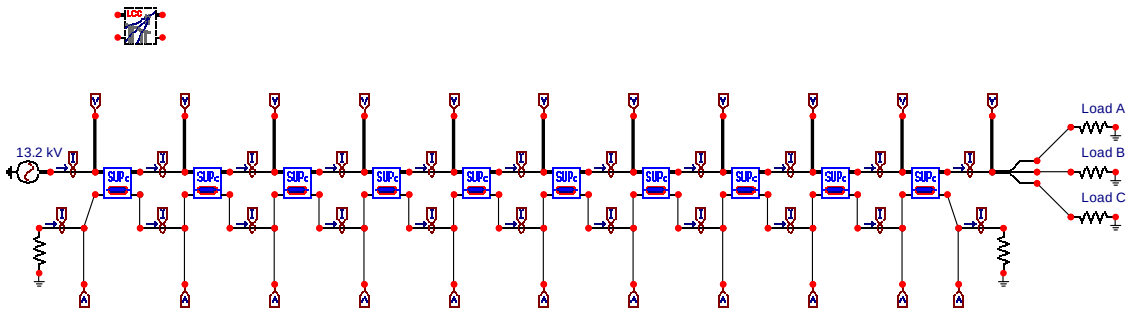

Figure (5.1) Power system configuration for the steady-state simulation of the triaxial cable.

current. For the 13.2 kV cable, this was accomplished by observing the line currents after each simulation and adjusting the balanced resistive load until 3 kA_{rms} was achieved in at least one of the three phases. It is important to note that the load was adjusted symmetrically, so that any electrical imbalance was a result of the cable parameters and not the load.

The ATP simulation results were compiled using Matlab™. Since ATP only outputs the time dependant voltages and currents along the cable length, the Matlab™ program named, "triaxATP", was written to calculate the phase angles and line power. The "triaxATP" program is included in Appendix B.

Steady-state simulations of the triaxial cable where also performed using the telegraph equations in Matlab™. The configuration of the telegraph equation (TE) model was the same as that of ATP, except for the omission of some cable parameters as described in section 2.3 of chapter 2. The program code, "triaxTE", is included in Appendix B.

5.1.3 Steady-State Simulation Results

Simulation of the 13.2 kV triaxial cable using ATP and the TE model produced comparable results. The results of the steady-state simulations are presented in this section as a function of cable distance from the source on the left-hand side to the load on the right-hand side. The solid lines represent ATP simulation and the dashed lines represent that of the TE model. Simulations of a 13.2 kV triaxial cable with a 69 MVA load at 0.9 power factor lagging, and a 69 kV triaxial cable with a purely resistive load were also performed and are included in Appendixes C & D. Simulation of a 200 m-long cable was not performed in this study, but evaluation of the 16 km results show that the electrical imbalance is negligible.

The voltage and current profiles presented in figures (5.2) and (5.3) show imbalances in both cable voltage and current for phases A, B, and C. The phase voltages are symmetric and assume the rated value at the source, but as the distance from the source approaches the load they begin to diverge. In contrast, the phase currents are imbalanced at the source, but appear to attempt convergence toward the load. Also, only one of the phase currents is at the rated value, the other two are either above or below the mark. As expected, the current in phase A is the lowest of the three phases due to the higher inductive reactance. In both cases, the ATP results show correlation with the TE model. However, there is some difference due to the omission of the axial field inductance in the TE model. The power factor angles presented in figure (5.4) reveal that phases B and C have higher capacitance than phase A, and that phase A has a higher inductance than phases B and C. The total reactive power presented in figure (5.5) is negative at the source end of the cable, suggesting that the cable behavior is capacitive for the described system configuration.

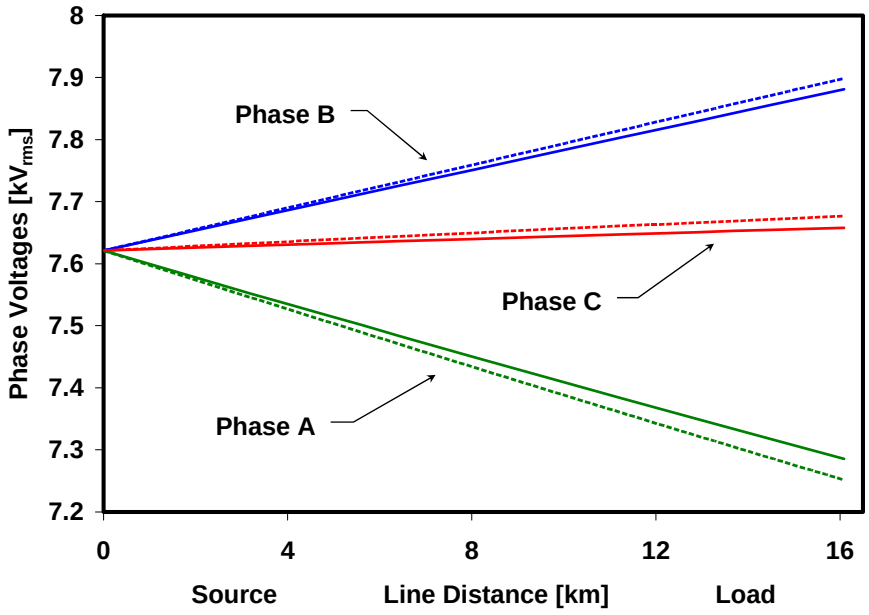

Figure (5.2) Phase voltages of a 13.2 kV triaxial cable.

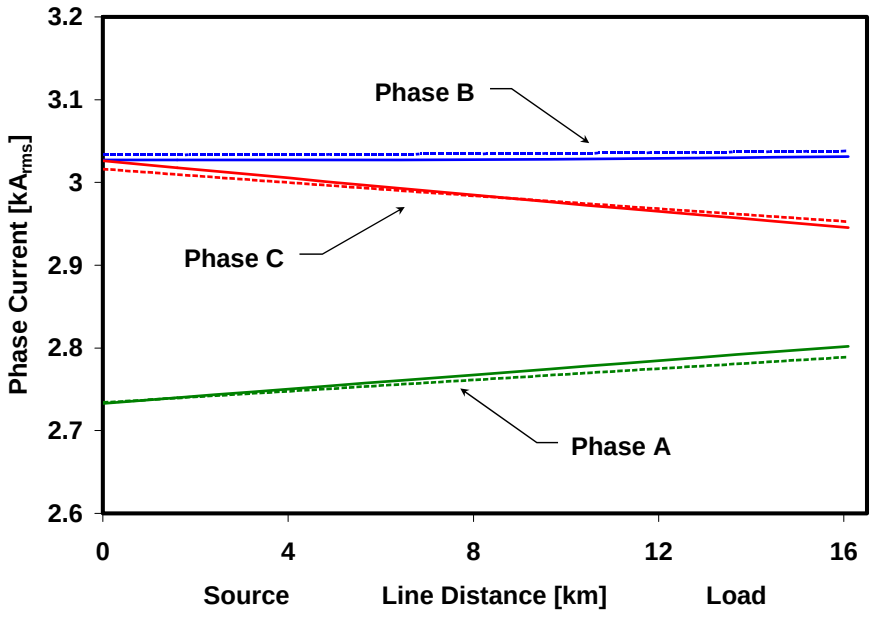

Figure (5.3) Phase currents of a 13.2 kV triaxial cable.

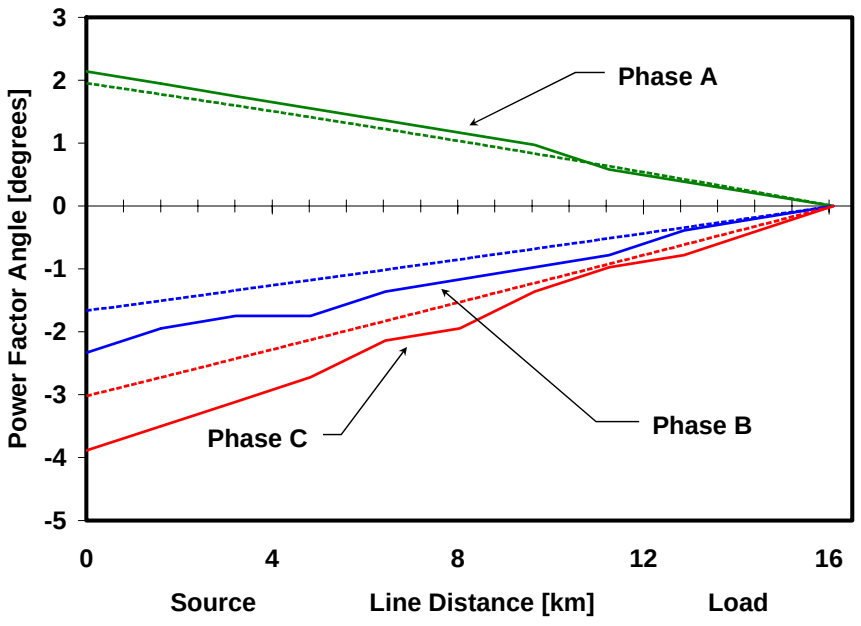

Figure (5.4) Power factor angles of a 13.2 kV triaxial cable.

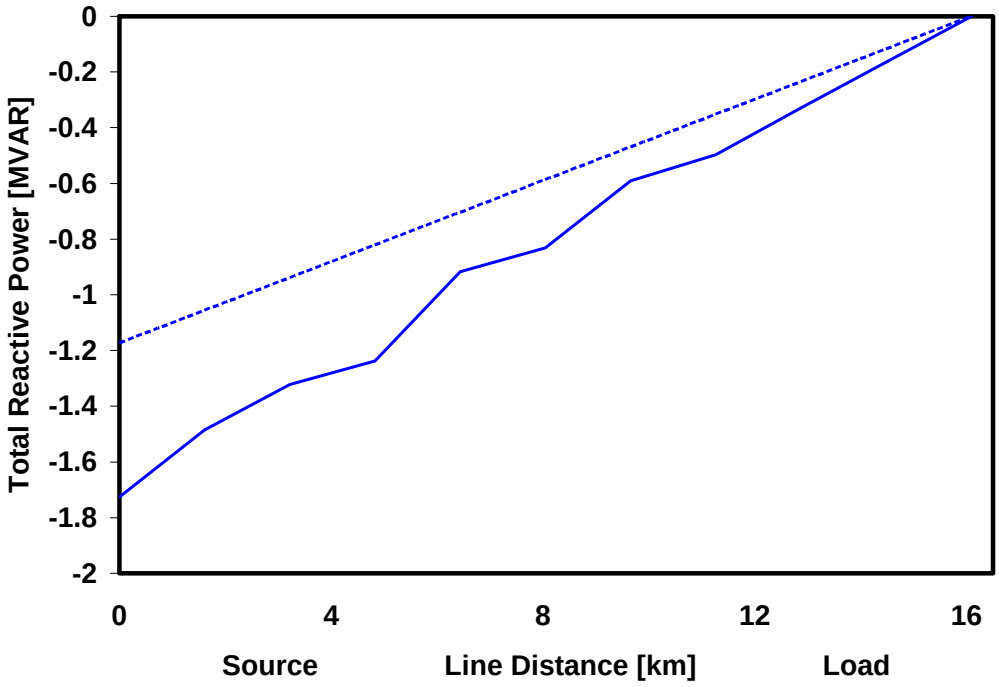

Figure (5.5) Total reactive power of a 13.2 kV triaxial cable.

The real power in each phase is described in figure (5.6) and shows an imbalance similar to the current in figure (5.3). The total real power presented in figure (5.7) is the sum of real power of each phase, and appears to be approximately constant. Comparison of the total real and reactive power plots in figures (5.5) and (5.7) shows that the magnitude of the total real power is much greater than the reactive power. Therefore, the reactive power has little effect on the apparent power of the cable, and the total apparent power is approximately the same as the total real power. Observation of figure (5.7) also shows that the total apparent power is lower than the rated value, a consequence of the lower than rated phase currents presented in figure (5.3).

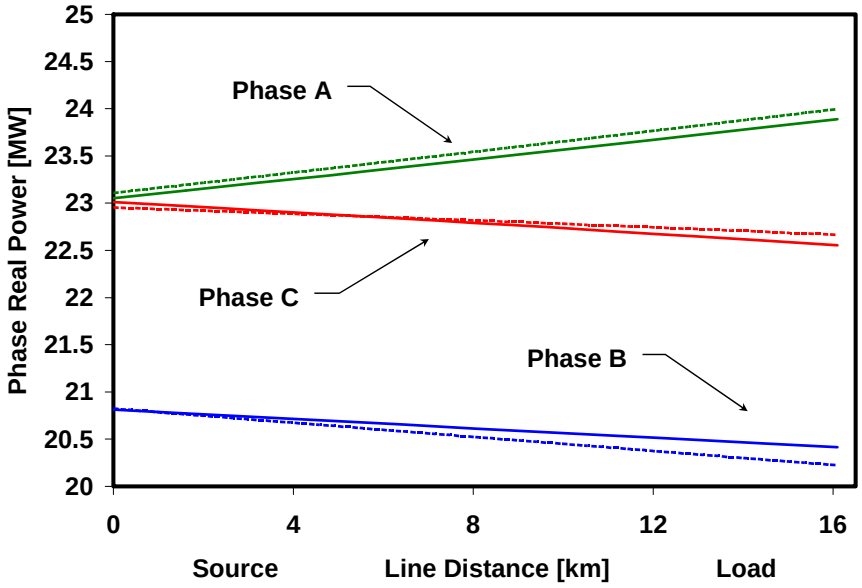

Figure (5.6) Phase real power of a 13.2 kV triaxial cable.

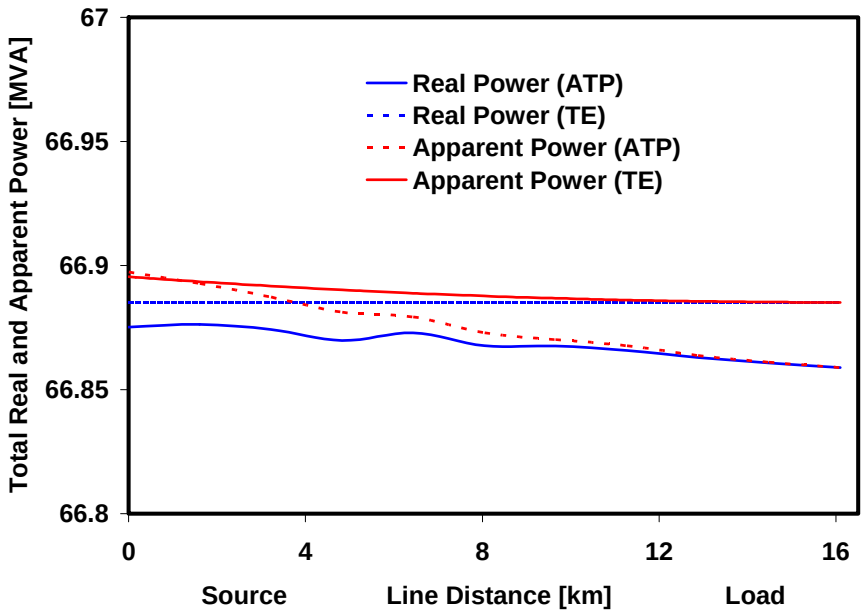

Figure (5.7) Total real and apparent power of a 13.2 kV triaxial cable.

The line-to-line voltages of the triaxial cable are presented in figure (5.8) and reveal a disagreement between ATP and the TE model. The ATP results show that voltages V_{ac} and V_{bc} increase together, while the TE model shows divergence of the two voltages. Initially, it appeared that a software or round-off error may be the source of this issue, because some oscillation existed in the ATP data. To rule-out any possibility that the omission of the axial field inductance term in the TE model may be the reason for the difference between the two voltage plots, the EC model was re-simulated in ATP with only the tangential field inductances. The resulting line-to-line voltages showed strong correlation with the TE model, which is evidence that the axial field inductance may be a significant parameter for triaxial cable study. The line-to-line voltages resulting from the re-simulated ATP case are presented in figure (5.9).

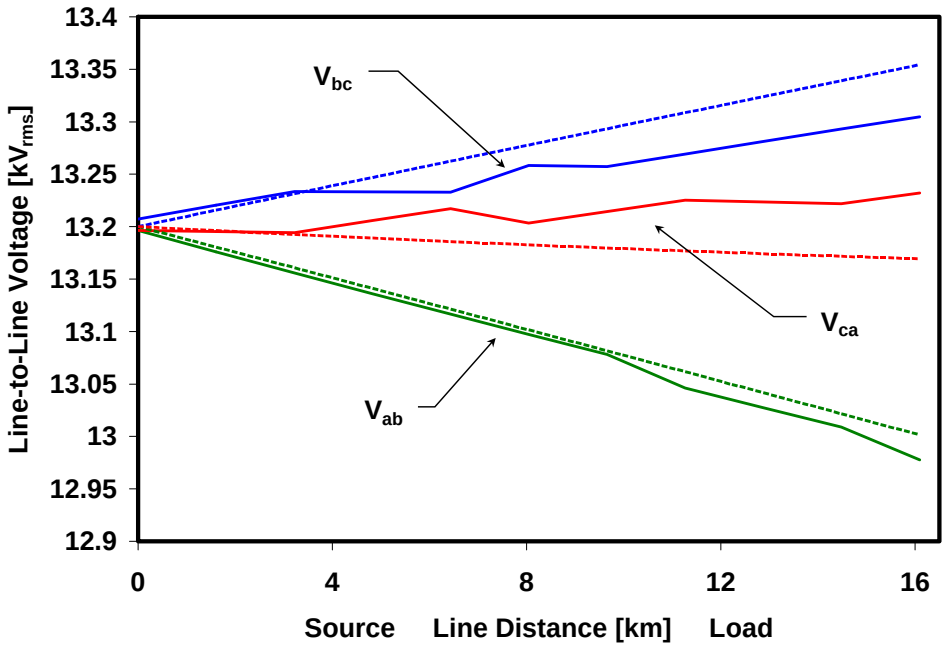

Figure (5.8) Line-to-line voltages of a 13.2 kV triaxial cable (1). Axial field inductance included.

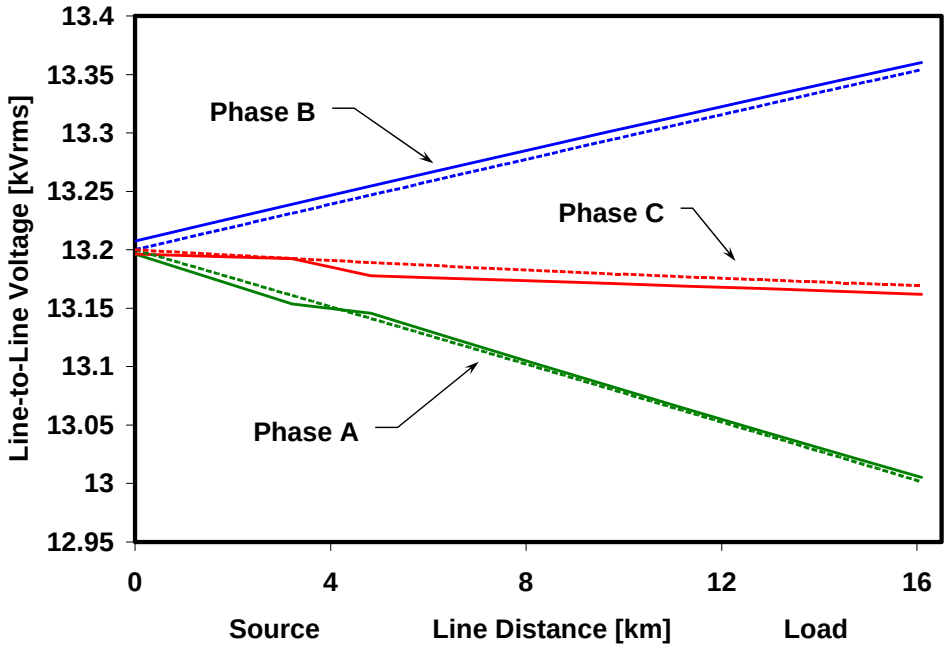

Figure (5.9) Line-to-line voltages of a 13.2 kV triaxial cable (2). Axial field inductance omitted.

Plots of the steady-state shield voltage and current presented in figure (5.10) show that the voltage of the shield at the endpoints is zero, a result that corresponds with the substation configuration described earlier. However, shield voltage at the midpoint distance peaks, a behavior similar to that of a previous underground cable study [43]. The shield current appears to be approximately inversely proportional to the shield voltage with maximum values occurring at the shield endpoints. However, according to the results, both shield current and voltage are small during steady-state operation.

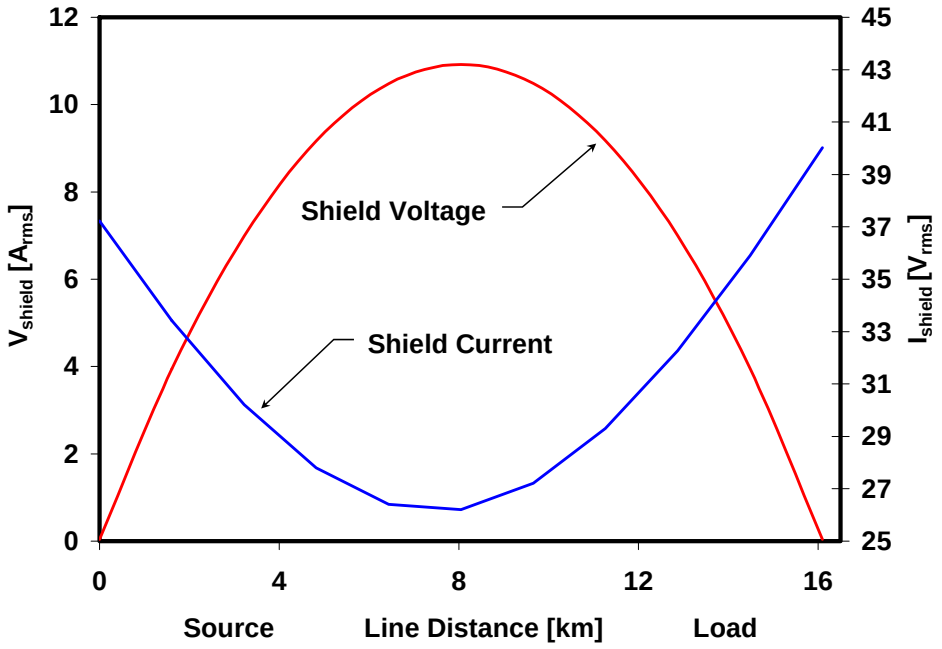

Figure (5.10) Copper shield voltage and current of a 13.2 kV triaxial cable.

5.2 Transient Analysis

The effect of transients on the triaxial cable was investigated by simulating various faults at the load end of the cable in ATP. Three fault types where considered in this study including single line-to-ground (SLG), double line-to-ground (DLG), and 3-phase faults (3 lines to ground). The resulting fault, phase, and shield currents were recorded at the source end of the cable and compiled utilizing a user-program named “triaxfault”, which was written for use in Matlab™ and is included in Appendix B. The pre-fault condition of the cable was obtained from simulations in section 5.1.

5.2.1 Transient System Configuration

The source end of the cable was connected to a 13.2 kV, 3-phase generator and a series equivalent network impedance to represent the step-down transformer and the power system on the high-voltage side. The cable was represented by one SUPc user-defined element with its resistance set to a negligible value so that the cable resistance could be represented using a type-99 nonlinear resistance element in series with each cable phase. Due to the high currents associated with power system faults, the superconducting layers within the cable make the transition to the normal state, so that the nonlinear resistance parameters discussed in chapter 4 needed to be included in the transient analysis. Faults were then applied to the system using ATP switching elements grounded through a 1 mΩ resistor to prevent iteration errors. A representation of the system configuration for a SLG fault on phase C is presented in figure (5.11). The system configurations for other fault types considered in this study are similar to that in figure (5.11) with the exception that the position and number of the switching elements vary.

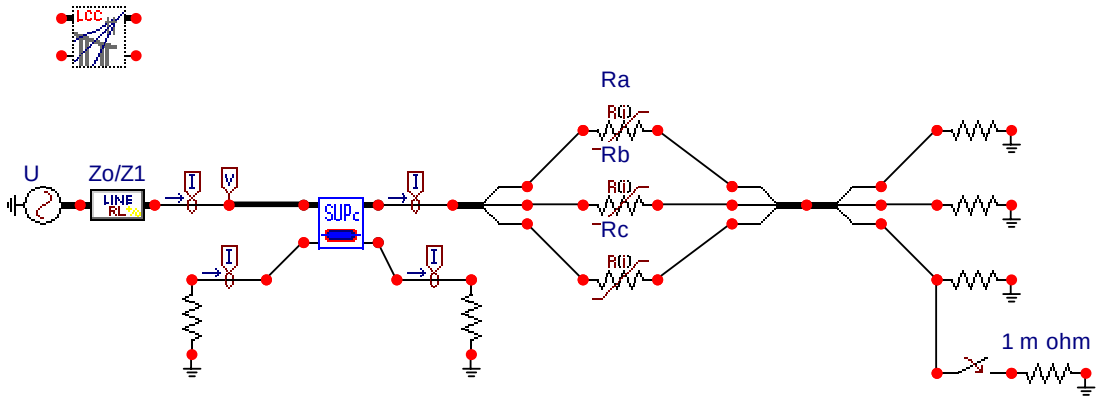

Figure (5.11) Power system configuration for simulation of a SLG fault on phase C.

The equivalent network impedance discussed above is the linear combination of the source impedance and the short-circuit transformer impedance [45]. This impedance consolidates the network on the high-voltage side of the transformer itself into a lumped parameter that can be accounted for in ATP. The equivalent network impedance is an important parameter because it limits fault currents that can be much larger if only the cable impedance is present. A description of the equivalent source impedance is presented in figure (5.12). Where, Z_{eq}, includes the zero and positive sequence components of the system. Values for the equivalent network impedance were calculated from information obtained by the utility, and by assuming some nominal parameter values. Calculation of the equivalent network impedance is included in Appendix E.

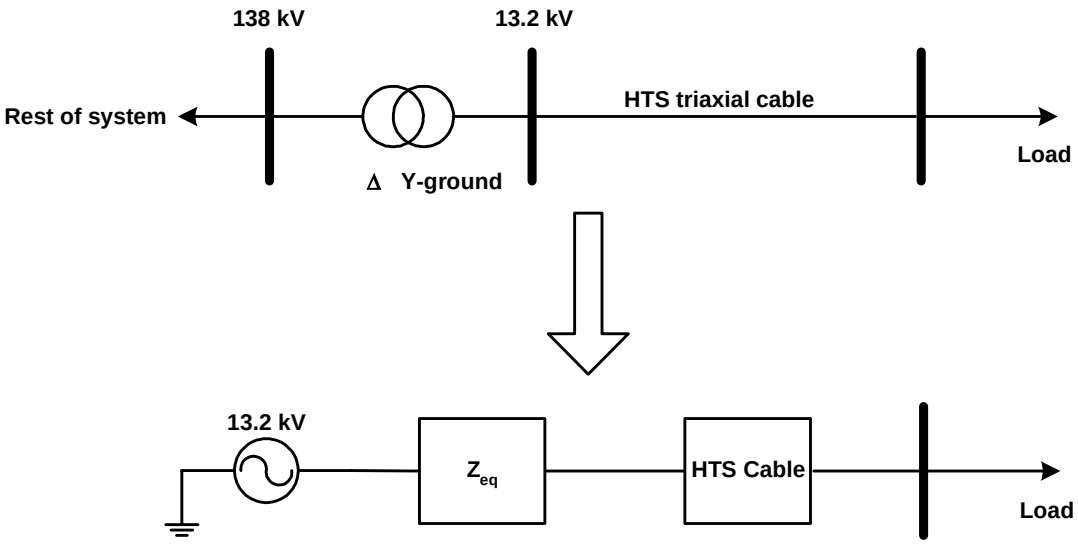

Figure (5.12) Description of the equivalent network impedance.

5.2.2 Transient System Simulations

The three fault types discussed in this chapter were simulated on the 13.2 kV triaxial cable in ATP. Time-dependent plots of the resulting cable currents for selected fault locations are presented in figures (5.13), (5.14), and (5.15). The maximum currents for each fault type are presented in table (5.1).

The fault simulations in ATP revealed that the largest peak fault currents resulted from a DLG fault applied to phases A and C, while the largest shield current resulted from a SLG fault on phase C. For most of the fault cases simulated, the shield current approached a peak value of 500 A, an amount 10 times the pre-fault value of 50 A.

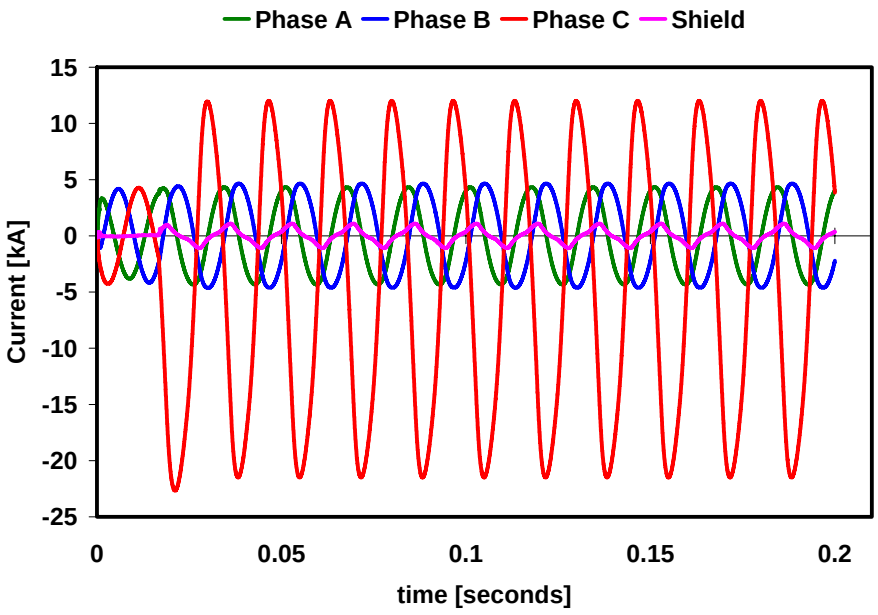

Figure (5.13) Cable currents resulting from a SLG fault on phase C.

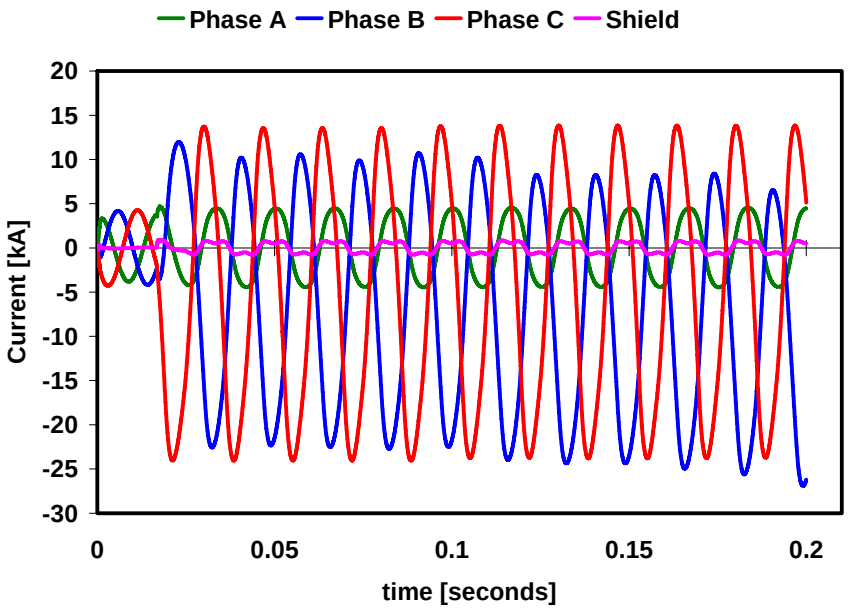

Figure (5.14) Cable currents resulting from a DLG fault on phases B & C.

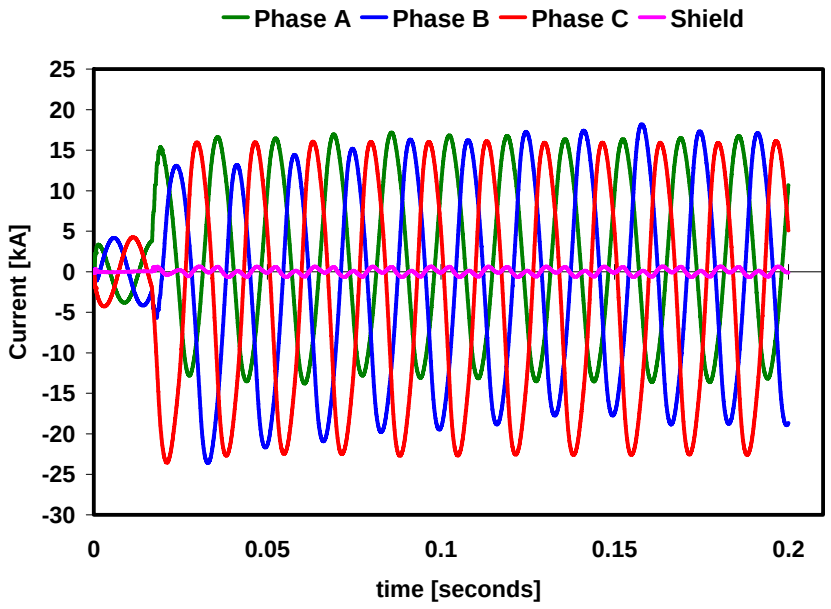

Figure (5.15) Cable currents resulting from a 3-phase fault.

Table (5.1) Peak cable currents resulting from specified line-to-ground faults.

Fault type and location	$I_{phase\ A}$ (kA_{peak})	$I_{phase\ B}$ (kA_{peak})	$I_{phase\ C}$ (kA_{peak})	I_{shield} (kA_{peak})
Pre-fault	3.9	4.3	4.2	0.05
SLG (A)	18	4.5	4.5	0.5
SLG (B)	4.0	18.0	4.5	0.5
SLG (C)	4.0	4.5	21	1.0
DLG (A, B)	30.0	20.0	4.8	0.5
DLG (B, C)	4.5	25.0	23.0	0.7
DLG (A, C)	29.0	4.5	20.0	0.5
3-phase	16.0	20.0	16.0	0.5

Chapter 6

Concluding Remarks

An electric circuit (EC) model was composed to describe the electrical behavior of an HTS triaxial cable for simulation in ATP. The model included the self and mutual inductance parameters due to magnetic fields tangent to the cable cross-section and parallel with the axial length of the cable. A dynamic resistance as a function of current was included to account for losses in the HTS tapes for both the superconducting and normal states using the flux flow method. A cold copper magnetic shield was included in the model using the Cable Parameters subroutine in ATP. The EC model composed in this study was based on a 200 m prototype that is to be installed at the Bixby substation for operation at 13.2 kV, 3 kA_{rms}, and 69 MVA. A line practical for future applications, 16 km, was considered in the study.

6.1 Discussion of Results

Simulations of the EC model were performed to measure the steady-state electrical imbalance caused by the asymmetric cross-section of the cable and cable currents resulting from applied faults. Induced shield currents due to the electrical imbalance from both cases were also measured. Steady-state simulation of the EC model with a balanced, 3-phase, resistive load showed that the inherent electrical imbalance becomes more significant as the cable distance increases from the source towards the load. Observation of the power factor angles revealed that one phase may have a power factor that is capacitive while another may have an inductive power factor. These steady-state results showed that for short cable lengths like the 200 m prototype, the imbalance is small and the effect on the surrounding power system may be negligible, but longer cable lengths may present a voltage imbalance that can adversely affect 3-phase machinery. A local

power utility suggested that the difference between the line-to-neutral voltages supplied to 3-phase machinery should not exceed 3% or negative sequence currents will degrade the performance and operating life of such machines [46]. The triaxial cable results in figure (5.2) show that over 7% difference occurs between the line-to-neutral voltages. Therefore, a correction of the imbalance may be necessary in this case or else the length of the cable would have to be reduced from 16 km to 8 km approximately. However, in urban centers where the triaxial cable is expected to have the most impact, such a cable would feed numerous single-phase loads consisting of residences and offices, so the electrical imbalance may not be an issue for this type of application.

Transient simulations revealed that fault currents approaching 30 kA_{peak} may occur depending on fault type and location. The simulations also revealed that large electrical imbalances resulting from applied faults cause induced currents in the surrounding phases and copper shield. These induced shield currents can become significant, approaching peak values of 1 kA.

6.2 Future Work

The work performed in this exploratory study is a compilation of basic information regarding HTS cables and power systems analysis. It is the hope of this author that this study will serve as a benchmark, and that further studies may refine the compiled model and increase its sophistication. Further studies may also investigate in greater detail the effect of the triaxial cable on a more practical power system, and possibly contrive solutions to issues that may arise, including the electrical imbalance.

There may be several ways to increase the sophistication of the model, a couple of them are briefly discussed here: First, the inclusion of a known thermal process would allow for a more accurate depiction of the HTS conducting layers under transient conditions. For instance, when $I<I_c$ is applied to an HTS tape, its resistance increases as explained in

chapter 4. This process results in a feedback loop such that as the tape heats up, I_c decreases, and additional heating occurs causing I_c to degrade, and so on. This feedback loop presents a thermal runaway condition that may cause damage to the HTS material if precautionary measures are not taken. Therefore the inclusion of a thermal process would allow cable designers to investigate various electrical stabilizing schemes and how they may affect the electrical properties of the cable. Second, inclusion of the cryostat may add another element of heating to the cable if the imbalance becomes large enough that resulting magnetic fields cause an induced cryostat current to flow.

Further studies of the electrical imbalance associated with the triaxial cable may lead to solutions that could preserve power quality. Such solutions may include transposition of the phases, where the phases are swapped at incremented line distances to compensate for the imbalance. Simulation of the EC model in ATP using the transposition elements can help to determine the transposition sequence and the distance increment for which transposition should be performed. In the case of the triaxial cable, phase transposition may prove impractical both technically and economically due to the complexity of the cable terminations, therefore other methods of compensation like capacitor banks or static compensators may be more attractive to utilities.

6.3 Closing Remarks

The EC model developed and simulated in this study attempted to provide some insight into the electrical behavior of an HTS triaxial power cable in a power system. Before the commencement of this study, little information regarding such a cable had been published in literature, therefore those who conduct future studies regarding the electrical behavior of a triaxial cable will have a possible starting point from which to build upon.

List of References

List of References

[1] V. E. Sytnikov, N. V. Poliakova, V. S. Vysotsky, "Current Distribution and voltage-current relation in multi-layered LTS and HTS cable core: a review," *Physica C* 401, pp.47-56, 2004.

[2] Nathan Kelly et al., "HTS cable system demonstration at Detroit Edison," *Proceedings of the IEEE Power Engineering Society Transmission and Distribution Conference*, v 2, 2001, p 871-876.

[3] M. A. Young et al., "Measurements of the Performance of BSCCO HTS Tape under Magnetic Fields with a Cryocooled Test Rig," *IEEE Transactions on Applied Superconductivity*, Vol. 13, No. 2 III, June 2003, pp. 2964-2967.

[4] M. Cyrot, "Introduction to superconductivity and high-Tc materials," World Scientific, Singapore; River Edge, N. J. 1992.

[5] C. Dineen et al., "High Temperature Superconductors for Power Cables," *Journal of Alloys and Compunds*, 195, (1993), pp. 507-510.

[6] Edmund S. Otabe et al., "Hysteresis Loss in a Superconducting Bi-2223 Tape with Fine Filaments," *IEEE Transactions on Applied Superconductivity*, Vol. 9, No. 2, June 1999, pp. 2569-2572.

[7] J. Jippin, A Mansoldo, C. Wakefield, "The impact of HTS cables on Power Flow distribution and Short-circuit currents within a meshed network," *Proceedings of the IEEE Power Engineering Society Transmission and Distribution Conference*, v 2, 2001, p 736-741.

[8] Diego Politano et al., "Technical and economical assessment of HTS Cables," *IEEE Transactions on Applied Superconductivity*, Vol. 11, No. 1, March 2001. pp. 2477-2480.

[9] P. W. Fisher et al., "Design, Analysis, and Fabrication of a Tri-Axial Cable System," *IEEE Transactions on Applied Superconductivity*, Vol. 13, No. 2, June 2003, pp. 1938-1941.

[10] J. P. Stovall et al., "Installation and Operation of the Southwire 30-meter High-Temperature Superconducting Power Cable," *IEEE Transactions on Applied Superconductivity*, Vol. 11, No. 1, March 2001.

[11] D. T. Lindsay, "Operating experience of the southwire high temperature superconducting cable installation," *Proceedings of the IEEE Power Engineering Society Transmission and Distribution Conference*, v 2, n WINTER MEETING, 2001, p 442-447.

[12] S. Honjo et al., "High-T_c superconducting power cable development," *Physica C* 357-360, pp.1234-1240, 2001.

[13] K. Miyoshi et al., "Development of 66 kV-class High-Tc Superconducting power transmission cable – remarkable decrease in AC losses and production of prototype cable," *Physica C* 357-360, pp.1259-1262, 2001.

[14] M. J. Gouge et al., "High-temperature superconducting tri-axial power cable," *Physica C: Superconductivity and its Applications*, v 392-396 II, n SUPL., October, 2003, p 1180-1185.

[15] S. Kruger Olsen et al., "Loss and Inductance Investigations in a 4-layer Superconducting Prototype Cable Conductor," *IEEE Transactions on Applied Superconductivity*, Vol. 9, No. 2, June 1999, pp.833-836.

[16] Noji et al., "AC loss analysis of 114 MVA high-Tc superconducting model cable," *Physica C* 392-396, pp.1134-1139, 2003.

[17] Mukoyama et al., "Uniform current distribution conductor of HTS power cable with variable tape-winding pitches," *IEEE Transactions on Applied Superconductivity*, Vol. 9, No. 2, June 1999, pp. 1269-1272.

[18] F. Grilli, M. Sjöström, "Prediction of resistive and hysteretic losses in a multi-layer high-T_c superconducting cable," *Supercon. Sci. Technol*. 17 (2004) 409-416.

[19] M. Däumling, "A model for the current distribution and ac losses in superconducting multi-layer power cables," *Cryogenics*. 39 (1999) 759-765.

[20] H. Noji, "AC loss of a high-T_c superconducting power-cable conductor," *Supercon. Sci. Technol*. 10 (1997) 552-556.

[21] ATP-EMTP Program, Canada/American EMPT User Group.

[22] H. Høidalen, L. Prikler, "New Features in ATPDraw for advanced modeling of lines/cables and transformers," EMTP/ATP Workshop, February 25, 2004, Seoul, Korea.

[23] J. C. Das, "*Power System Analysis: Short-Circuit Load Flow and Harmonics,*" New York, NY. Marcell Dekker 2002.

[24] A. Ametani, "A General Formulation of Impedance and Admittance of Cables," *IEEE Trans. On Power Apparatus and Systems,* vol PAS-99, no. 3, 1980.

[25] L. M. Wedepohl, D. J. Wilcox, "Transient analysis of underground power-transmission systems," *Proc. IEE,* vol 120, no. 2, 1973, 253-260.

[26] F. T. Ulaby, "*Fundamentals of Applied Electromagnetics,*" Menlo Park, CA. Addison Wesley 1999.

[27] U. Iana and A. Inan, "*Engineering Electromagnetics*", Addidon-Wesley, 1999.

[28] M. Daumling et al., "Ac loss in superconducting power cables," *published in Studies of High Temperature Superconductors,.* Nova Science Publishers, Vol. 33, 2000, pp. 73.

[29] F. London and H. London, "The Electromagnetic Equations of the Supraconductor", *Proceedings of the Royal society of London. Series A, Mathematical and Physical Sciences*, Vol. 149, No. 866, (March 1, 1935), pp. 71-88.

[30] P. Lorrain, D. Corson, "*Electromagnetic Fields & Waves*", W. H. Freemanans Co., New York, 2nd edition, 1970.

[31] H. Benson, "*University Physics*", John Wiley & Sons, New York, 1996.

[32] D. Willen, et al., "Application potential for low-loss and low-impedance HTS cables to enable the cost-effective integration of sustainable and distributed energy sources," *Submitted at the EUCAS for publication in the IEEE trans. On Appl. Superconduct.,* September 2003.

[33] Jakob Rhyner, "Magnetic properties and AC-losses of superconductors with power law current-voltage characteristics", *Physica C* 212, pp.292-300, 1993.

[34] N. Magnusson, "Semi-empirical model of the losses in HTS tapes carrying AC currents in AC magnetic fields applied parallel to the tape", *Physica C* 349, pp.225-234, 2001.

[35] W. T. Norris, "Calculation of hysteresis losses in hard superconductors carrying ac: isolated conductors and edges of this sheets", *Phys. D: Appl. Phys.* 3, pp.489, 1970.

[36] G. Vellego, P. Metra, "An analysis of the transport losses measured on HTSC single-phase conductor prototypes," *Supercon. Sci. Technol*. 8 (1995) 476-483.

[37] W. J. Carr. Jr, "AC *Loss and Macroscopic Theory of Superconductors*", Taylor and Francis and, New York, NY. 2001.

[38] J. J. Rabbers, "*AC Loss in Superconducting Tapes and Coils*", Doctoral Thesis, University of Twente, The Netherlands, October 2001.

[39] J. W. Lue, et al., "Electrical Tests of a Triaxial HTS Cable Prototype," *AIP Conference Proceedings*. (2002) 606-613.

[40] Y. Iwasa, "*Case Studies in Superconducting Magnets*", Plenum Press, New York, 1994.

[41] M. A. Young, et al., "Burnout Test of First- and Second-Generation HTS Tapes in Liquid Nitrogen Bath Cooling," *AIP Conference Proceedings*. (2004) 860-868.

[42] W. H. Press, et al., "*Numerical Recipies: The Art of Scientific Computing*", Cambridge University Press, New York, 1986.

[43] L. M. Wedepohl, D. J. Wilcox, "Estimation of transient overvoltages in power-cable transmission systems," *Proc. IEE*, vol. 120, no. 8, 1973.

[44] M. J. Gouge, D. Swain, "Triax cable modes", Internal correspondence, Oak Ridge National Laboratory, June 2003.

[45] L. Prikler, Internal correspondence, Budapest University of Technology and Economics, September 2004.

[46] B. Coppick, Internal Correspondence, Powell Valley Electric Utility, December 2004.

Appendixes

Appendix A

Nomenclature

Key HTS terms and the location of their definitions

Abbreviations

AC	Alternating Current
AEP	American Electric Power
ATP	Alternative Transients Program
BSCCO	Barium-Strontium-Calcium-Copper-Oxide
CD	Cold-Dielectric
DC	Direct Current
EC	Electric Circuit
HTS	High Temperature Superconductivity
LN2	Liquid Nitrogen
LTS	Low Temperature Superconductor
TE	Telegraph Equations
TEM	Transverse Electromagnetic
WD	Warm-Dielectric

Appendix B

Matlab™ Programs

“triaxresist”

```
function
[Rphase1,Rphase2,Rphase3,Vphase1,Vphase2,Vphase3]=triaxresist(Iphase1,Iphase2,Iphase3)
%%%%%%%%%%%%%%%%%%%%%%%%%%%%%%%%%%%%%%%%%%%%%%%%%%%%%%%%%%%%%%%%%%%%%%%%%%%%
%Dynamic Resistance of Triaxial Cable                                        %
%                                                                            %
%Written By: Marcus Young 8/16/04                                            %
%                                                                            %
%Dynamic resistance is combination of transport                              %
%current loss and ac loss.                                                   %
%The ac loss is estimated by the monoblock                                   %
%model, and the transport loss is estimated from the                         %
%flux flow resistivity.                                                      %
%%%%%%%%%%%%%%%%%%%%%%%%%%%%%%%%%%%%%%%%%%%%%%%%%%%%%%%%%%%%%%%%%%%%%%%%%%%%

%Input Parameters:
Ic=[5860,6489,6700];        %phase critical currents
Ip=[Iphase1,Iphase2,Iphase3];
numtapes=[56,63,70];        %number of tapes per phase
Do=[42.75,47.75,52.75];     %outside diameter per phase
Di=[42.25,47.25,52.25];     %inside diameter per phase

%Constant Parameters
muo=4*pi*10^-7;
f=60;

%%%%%%%%%%%%%%%%%%%%%%%%%%%%%%%%%%%%%%%%%%%%%%%%%%%%%%%%%%%%%%%%%%%%%%%%%%%%
%Use Monoblock model to calculate Rac                                        %
%                                                                            %
%%%%%%%%%%%%%%%%%%%%%%%%%%%%%%%%%%%%%%%%%%%%%%%%%%%%%%%%%%%%%%%%%%%%%%%%%%%%
%Set peak current value:

%Magnetization loss (Monoblock model)
for s=1:3
   F(s)=Ip(s)/Ic(s);
   h(s)=(Do(s)^2-Di(s)^2)/Do(s)^2;
   if Ip(s)>Ic(s)
       Ipac(s)=Ic(s);
       Fac(s)=Ipac(s)/Ic(s);
       Rac(s)=(f*muo/(2*pi)*Ic(s)^2/h(s)^2*((2-Fac(s)*h(s))*Fac(s)*h(s)+2*(1-
Fac(s)*h(s))*log(1-Fac(s)*h(s))))/Ipac(s)^2;
   else
       Rac(s)=(f*muo/(2*pi)*Ic(s)^2/h(s)^2*((2-F(s)*h(s))*F(s)*h(s)+2*(1-
F(s)*h(s))*log(1-F(s)*h(s))))/Ip(s)^2;
        end
    end

%%%%%%%%%%%%%%%%%%%%%%%%%%%%%%%%%%%%%%%%%%%%%%%%%%%%%%%%%%%%%%%%%%%%%%%%%%%%
%Find transport resistance from Flux-flow model                              %
%                                                                            %
%%%%%%%%%%%%%%%%%%%%%%%%%%%%%%%%%%%%%%%%%%%%%%%%%%%%%%%%%%%%%%%%%%%%%%%%%%%%
for s=1:3
    Eo=1e-6;
    Rm=(-.5275+.0175*(77))/(14000*numtapes(s));    %[Ohms/cm]--resistance of Ni-plated
tape @ 77K
    nvalue=14;
    Ibscco(s)=bisection(Ip(s),Ic(s),nvalue,Rm);
    Rbscco(s)=Eo*((Ibscco(s)/Ic(s))^nvalue)/(Ibscco(s)); %in [Ohm/cm]
    Rtransport(s)=((Rbscco(s)*Rm)/(Rbscco(s)+Rm))*100;  %[Ohm/m]
end

%%%%%%%%%%%%%%%%%%%%%%%%%%%%%%%%%%%%%%%%%%%%%%%%%%%%%%%%%%%%%%%%%%%%%%%%%%%%
%Calculate total effective resistance: Rac+Rtransport   %
```

```
%                                                                       %
%%%%%%%%%%%%%%%%%%%%%%%%%%%%%%%%%%%%%%%%%%%%%%%%%%%%%%%%%%%%%%%%%%%%%%
for s=1:3
    Rphase(s)=Rac(s)+Rtransport(s);
    Vphase(s)=Rphase(s)*Ip(s);
end

Rphase1=Rphase(1);
Rphase2=Rphase(2);
Rphase3=Rphase(3);
Vphase1=Vphase(1);
Vphase2=Vphase(2);
Vphase3=Vphase(3);
```

“bisection”

```
function Z=bisection(I,Ic,n,Rm)
%Solves for Ihts using a bisection method
%Function used in "triaxresist"
%Marcus Young

ACC=.0001; %set accuracy
maxiterations=40;
%RM=5.7065e-5;
%I=305;
Eo=1e-6;
%n=14;
%Ic=114.8835;

%Function to be solved
x1=0;
x2=I;
FMID=Rm*(I-x2)-Eo*(x2/Ic)^n;
F=Rm*(I-x1)-Eo*(x1/Ic)^n;

%Perform bisection method
if F*FMID>=0
    disp('Root must be bracketed for bisection');
    break
end
if F<0
    RTBIS=x1;
    DX=x2-x1;
else
    RTBIS=x2;
    DX=x1-x2;
end
for i=1:maxiterations
    DX=DX*0.5;
    XMID=RTBIS+DX;
    FMID=Rm*(I-XMID)-Eo*(XMID/Ic)^n;
    if FMID<0
        RTBIS=XMID;
    elseif abs(DX)<ACC
        Z=XMID;
        %disp(XMID);
        break
    elseif FMID==0
        Z=XMID;
        %dip(XMID);
        break
    end
end
```

“triaxresisvolt”

```
%%%%%%%%%%%%%%%%%%%%%%%%%%%%%%%%%%%%%%%%%%%%%%%%%%%%%%%%%%%%%%%%%%%%%%%
%Check for user-defined function triaxresist()          %
%                                                       %
%Written By: Marcus Young 8/19/04                       %
%                                                       %
%Uses function to plot effective resistance or voltage  %
%values for the triaxial cable using "triax resist".    %
%                                                       %
%Program also writes results from "triaxresist" to      %
%EXCEL.                                                 %
%%%%%%%%%%%%%%%%%%%%%%%%%%%%%%%%%%%%%%%%%%%%%%%%%%%%%%%%%%%%%%%%%%%%%%%

clear;
clc;

length=1609.43;  %length of line section [m]

Ip1=1:100:50000;     %Current range
Ip2=Ip1;
Ip3=Ip1;

sizeIp1=size(Ip1);
numpts1=sizeIp1(1,2);

for k=1:numpts1
    [r1,r2,r3,v1,v2,v3]=triaxresist(Ip1(k),Ip2(k),Ip2(k));
    Rp1(k)=r1*length;
    Rp2(k)=r2*length;
    Rp3(k)=r3*length;
    Vp1(k)=v1*length;
    Vp2(k)=v2*length;
    Vp3(k)=v3*length;
end
subplot(2,1,1)
plot(Ip1,Vp1,Ip2,Vp2,'r',Ip3,Vp3,'g');
subplot(2,1,2)
plot(Ip1,Rp1,Ip2,Rp2,'r',Ip3,Rp3,'g');
title('Effective voltage for type 99 non-linear resistance element in ATP');
xlabel('Ip [A]');
ylabel('Veff [V]');

grid;


M=[Ip1'*1e-3,Rp1',Rp2',Rp3'];
WK1WRITE('C:\MATLAB6p1\work\Rtriaxdata',M);


format short e
Ma=[Ip1',Rp1'];
save Madata.dat Ma /ascii;

Mb=[Ip2',Rp2'];
save Mbdata.dat Mb /ascii;

Mc=[Ip3',Rp3'];
save Mcdata.dat Mc /ascii;

length
```

“triaxATP”

```
%*//////ATP--.pl4 FILE CAPTURE FOR ATP TRIAXIAL CABLE SIMULATION//////////////////    *
%*  Loads time, voltage, and current data columns from .pl4 file and performs          *
%*  desired calculations so that line characteristics can be plotted as a function     *
%*  of distance.                                                                       *
%*                                                                                     *
%*  Version 1.3--created for triax10milecsd
%*  ///////////////created by Marcus Young/////June 23, 2004//////////////             *
%*************************************************************************************

clear;
clc;

%Load .pl4 file & assign data-----------------------------------------------------------
alldata=load('C:\AEP triax project\triaxprograms\60kvtri10micsd\triax10milecsd60kv.pl4');
sizedata=size(alldata)
columns=sizedata(1,2)
datacolumn=sizedata(1,1)
vcolumns=33;
columnsperphase=vcolumns/3;
time=alldata(:,1);
%*************************************************************************************

%Acquire voltage vectors----------------------------------------------------------------
k=1;    %incrementer for sorting out phases
for i=2:3:vcolumns+1   %phase A voltages
    t(k)=i;
    Va(:,k)=alldata(:,i);
    k=k+1;
end
k=1;
for i=3:3:vcolumns+1   %phase B voltages
    t(k)=i;
    Vb(:,k)=alldata(:,i);
    k=k+1;
end
k=1;
for i=4:3:vcolumns+1   %phase C voltages
    t(k)=i;
    Vc(:,k)=alldata(:,i);
    k=k+1;
end
%*************************************************************************************

%Acquire current vectors----------------------------------------------------------------
k=1;    %incrementer for sorting out phases
for i=46:3:columns-11   %phase A voltages
    t(k)=i;
    Ia(:,k)=alldata(:,i);
    k=k+1;
end
k=1;
for i=47:3:columns-11   %phase B voltages
    t(k)=i;
    Ib(:,k)=alldata(:,i);
    k=k+1;
end
k=1;
for i=48:3:columns-11   %phase C voltages
    t(k)=i;
    Ic(:,k)=alldata(:,i);
    k=k+1;
end
%*************************************************************************************

%Create distance vector-----------------------------------------------------------------
for i=1:columnsperphase
```

```
    deltad(i)=(i-1);
end
%*******************************************************************************************

%Find rms voltage at each distance-----------------------------------------------
for i=1:columnsperphase
    vamax(i)=max(Va(:,i))/sqrt(2);
    vbmax(i)=max(Vb(:,i))/sqrt(2);
    vcmax(i)=max(Vc(:,i))/sqrt(2);
end
%*******************************************************************************************

%Find rms current at each distance-----------------------------------------------
for i=1:columnsperphase
    iamax(i)=max(Ia(:,i))/sqrt(2);
    ibmax(i)=max(Ib(:,i))/sqrt(2);
    icmax(i)=max(Ic(:,i))/sqrt(2);
end
%*******************************************************************************************

%Find angles between voltages and currents---------------------------------------------
%calculate time vector for one cycle

for i=1:1854
    time2(i)=time(i);
    va2(i,:)=Va(i,:);
    ia2(i,:)=Ia(i,:);
    vb2(i,:)=Vb(i,:);
    ib2(i,:)=Ib(i,:);
    vc2(i,:)=Vc(i,:);
    ic2(i,:)=Ic(i,:);
end
[r1,c1]=min(va2);
[r2,c2]=min(ia2);
[r3,c3]=min(vb2);
[r4,c4]=min(ib2);
[r5,c5]=min(vc2);
[r6,c6]=min(ic2);
dtime1=time(c2)-time(c1);
dtime2=time(c4)-time(c3);
dtime3=time(c6)-time(c5);
theta1=dtime1/(1/60)*2*pi;
theta2=dtime2/(1/60)*2*pi;
theta3=dtime3/(1/60)*2*pi;

%Find voltage angle with respect to zero reference angle:
%Therefore, the max occurs at pi/2, or at T/4, where T=1/60 in this case.
vreftime=(1/60)/2;
phangle1=(time(c1)-vreftime)/(1/60)*2*pi;

phangle2=(time(c3)-vreftime)/(1/60)*2*pi;
phangle3=(time(c5)-vreftime)/(1/60)*2*pi;

%Find rectangular coordinates of each L-n voltage
van=(cos(phangle1)-j*sin(phangle1)).*abs(r1')/sqrt(2);
vbn=(cos(phangle2)-j*sin(phangle2)).*abs(r3')/sqrt(2);
vcn=(cos(phangle3)-j*sin(phangle3)).*abs(r5')/sqrt(2);

%Calculate LL voltages
vab=van-vbn;
vbc=vbn-vcn;
vca=vcn-van;

thetava=angle(van)*180/pi;
thetavb=angle(vbn)*180/pi;
thetavc=angle(vcn)*180/pi;

thetavab=angle(van-vbn)*180/pi;
thetavbc=angle(vbn-vcn)*180/pi;
```

```
thetavca=angle(vcn-van)*180/pi;
%*******************************************************************************

%Calculate average real & reactive power (W & VA)-------------------------------------
--------------------
Pa=vamax.*iamax.*cos(theta1)';
Pb=vbmax.*ibmax.*cos(theta2)';
Pc=vcmax.*icmax.*cos(theta3)';
Qa=vamax.*iamax.*sin(theta1)';
Qb=vbmax.*ibmax.*sin(theta2)';
Qc=vcmax.*icmax.*sin(theta3)';

Qtot=Qa+Qb+Qc;
Ptot=Pa+Pb+Pc;

Stot=sqrt(Ptot.^2+Qtot.^2);
%*******************************************************************************
figure(1)
subplot(4,1,1)
plot(deltad,vamax*1e-3,'r',deltad,vbmax*1e-3,'b',deltad,vcmax*1e-3,'m');
%axis([0,10,0,80e3]);
title('Line Characteristics for the 13.2 kV Superconducting Triaxial Power Cable');
ylabel('Line Voltage [kVrms]');
%xlabel('Source                              distance [miles]
Load');


subplot(4,1,2)
plot(deltad,abs(vab)*1e-3,'r',deltad,abs(vbc)*1e-3,'b',deltad,abs(vca)*1e-3,'m');
ylabel('L-L Voltage [Vrms]');
%xlabel('Source                              distance [miles]
Load');


subplot(4,1,3)
plot(deltad,iamax*1e-3,'r',deltad,ibmax*1e-3,'b',deltad,icmax*1e-3,'m');
%axis([0,10,0,80e3]);
%title('Tiaxial Cable Current');
ylabel('Line current [kArms]');
%xlabel('Source                              distance [miles]
Load');

subplot(4,1,4)
plot(deltad,theta1*180/pi,'r',deltad,theta2*180/pi,'b',deltad,theta3*180/pi,'m');
ylabel('Phase angle shift [deg]');
xlabel('Source                             distance [miles]
Load');


figure(2)
subplot(3,1,1)
%plot(deltad,Pa,'r',deltad,Pb,'b',deltad,Pc,'m');

plot(deltad,Ptot*1e-6,'r');
title('Real & Reactive Power');
ylabel('P [MW]');
%axis([0,10,60,70]);


subplot(3,1,2)
plot(deltad,Qtot*1e-6,'r');
ylabel('Q [MVA]')
%axis([0,10,-1.5,.5])

subplot(3,1,3)
plot(deltad,Stot*1e-6,'r');
ylabel('S [MVA]');
xlabel('Source                             distance [miles]
Load');
```

```
%axis([0,10,60,70]);


%*******************************************************************************************
%Shield current and voltages/////////////*************************************************
%*******************************************************************************************
%Acquire voltage vectors-------------------------------------------------------------------
k=1;    %incrementer for sorting out phases
for i=35:1:45   %phase A voltages
    t(k)=i;
    Vs(:,k)=alldata(:,i);
    k=k+1;
end
%Acquire current vectors-------------------------------------------------------------------
k=1;    %incrementer for sorting out phases
for i=79:1:89   %phase A voltages
    t(k)=i;
    Is(:,k)=alldata(:,i);
    k=k+1;
end

%Find angles between shield voltages and currents-----------------------------------------
-
%calculate time vector for one cycle
for i=1:1667
    timecycle(i)=time(i);
    vs2(i,:)=Vs(i,:);
    is2(i,:)=Is(i,:);
end
[rs1,cs1]=max(vs2);
[rs2,cs2]=max(is2);
dtimes=time(cs2)-time(cs1);
thetas=dtimes/(1/60)*2*pi;



%Find rms voltage at each distance---------------------------------------------
for i=1:11
    vsrms(i)=max(Vs(:,i))/sqrt(2);
    vsmax(i)=max(Vs(:,i));
end
%*******************************************************************************************

%Find rms current at each distance---------------------------------------------
for i=1:11
    isrms(i)=max(Is(:,i))/sqrt(2);
    ismax(i)=max(Is(:,i));
end
%*******************************************************************************************

%Find real shield power
Ps=vsmax.*ismax.*cos(thetas)';
Qs=vsmax.*ismax.*sin(thetas)';


figure(3)
%subplot(2,1,1)
%plot(time,Vs)
%axis([0,.0167,-20e-9,15e-9])
%subplot(2,1,2)
%plot(time,Is)
subplot(2,2,1);
plot(deltad,vsrms);
title('shield voltage')
ylabel('Vsrms   [V]');
subplot(2,2,2);
plot(deltad,isrms);
title('shield current')
ylabel('Isrms   [A]');
```

```
subplot(2,2,3)
plot(deltad,thetas)
title('power angle')
ylabel('theta   [degrees]');
xlabel('source          distance (miles)        load');
subplot(2,2,4)
plot(deltad,Ps*1e-3,'r',deltad,Qs*1e-3);
title('real & reactive power')
ylabel('P (red)  [kW] & Q (blue)   [kVAR]');
xlabel('source          distance (miles)        load');

figure(4)

subplot(4,1,1)
plot(deltad,vamax*1e-3,'g',deltad,vbmax*1e-3,'b',deltad,vcmax*1e-3,'r');
title('ATP Simulation Results for the 13.2 kV Superconducting Triaxial Power Cable');
ylabel('L-n Voltage [kVrms]');
%xlabel('Source                              distance [miles]
Load');

subplot(4,1,2)
plot(deltad,abs(vab)*1e-3,'g',deltad,abs(vbc)*1e-3,'b',deltad,abs(vca)*1e-3,'r');
ylabel('L-L Voltage [Vrms]');
%xlabel('Source                              distance [miles]
Load');

subplot(4,1,3)
plot(deltad,thetava,'g',deltad,thetavb,'b',deltad,thetavc,'r');
ylabel('thetavln [degrees]');
%xlabel('Source                              distance [miles]
Load');

subplot(4,1,4)
plot(deltad,thetavab,'g',deltad,thetavbc,'b',deltad,thetavca,'r');
ylabel('thetavll [degrees]');
axis([0 10 -100 160]);
xlabel('Source                             distance [miles]
Load');


%Save data to a file for Excel Plotting
%convert from miles to km
dis=deltad*1.60934;
M=[dis',vamax'*1e-3,vbmax'*1e-3,vcmax'*1e-3,vsrms',iamax'*1e-3,ibmax'*1e-3,icmax'*1e-
3,isrms',theta1*180/pi,theta2*180/pi,theta3*180/pi,Ptot'*1e-6,Pa'*1e-6,Pb'*1e-6,Pc'*1e-
6,Qtot'*1e-6,Qa'*1e-6,Qb'*1e-6,Qc'*1e-6,Stot'*1e-6,Ps'*1e-
3,thetava,thetavb,thetavc,thetavab,thetavbc,thetavca,abs(vab)*1e-3,abs(vbc)*1e-
3,abs(vca)*1e-3];
WK1WRITE('C:\AEPtemp\10miledata69kv',M);
```

“triaxTE”

```
%TE model for the 13.2kV Triaxial Cable
%Marcus Young

clear;
clc;
x=1
%Define system parameters.
R=2.6;                          %load resistance (ohms) (wye configuration)
xmiles=10;                      %cable length (miles)
xl=xmiles*1609.34;              %cable length (meters)
v1m=13.2/sqrt(3);                       %source voltage magnitude (kV) (line-to-line)


%Define radii (in m) of each concentric phase of infintesimal width.
a1=0.02125*0.0254;
a2=.02375*0.0254;
a3=.02625*0.0254;
a4=.0295*0.0254;

%Define constitutive parameters of the materials.
mur=1;                          %relative permeability
muo=(4*pi)*10^-7;                 %permeability of free space (H/m)
mu=mur*muo;                     %permeability (H/m)

epsilonr=2.6;                   %relative permittivity or dielectric constant
epsilono=8.85e-12;              %permittivity of free space (F/m)
epsilon=epsilonr*epsilono;      %permittivity (F/m)

c=3e8;                          %speed of light in a vacuum (m/s)

%Calculate wavenumber in accordance with equation 2.39 for f=60Hz in dielectric.
omega=2*pi*60;                  %angular velocity (rad/s)
beta=omega*sqrt(mu*epsilon);    %phase constant or wavenumber (rad/m)
%*************************************************************************

%Set-up natural logarithims for inductance & capacitance calulations.
%Refer to equations 3.7 & 3.9
%1) set-up natural logarithims for inductance calulations
ML(1,1)=log(a4/a1);
ML(1,2)=log(a4/a2);
ML(1,3)=log(a4/a3);
ML(2,1)=log(a4/a2);
ML(2,2)=log(a4/a2);
ML(2,3)=log(a4/a3);
ML(3,1)=log(a4/a3);
ML(3,2)=log(a4/a3);
ML(3,3)=log(a4/a3);

%2) set-up natural logarithims for capacitance calulations by taking the inverse.
MC=inv(ML);
%*************************************************************************

%Calculate inductance and capacitance per meter.
lprime=mu/(2*pi)*ML;            %inductance matrix (H/m)
cprime=2*pi*epsilon*MC;         %capacitance matrix (F/m)
%*************************************************************************

%Calculate the characteristic admittance & impedance matrices of the coupled line system
%according to the characteristic impedance for a coaxial cable found in table 2-2.
%Since the cable is superconducting, resistance is assumed to be zero.
zo=60/sqrt(epsilonr)*ML;        %characteristic impedance (ohms)
yo=inv(zo);                     %characteristic admittance (siemens)
%*************************************************************************

%Calculate input impedance of the cable usinf equation 2.63.
zl=eye(3)*R;    %load impedance matrix
```

```
zinum=zl*cos(beta*xl)+i*zo*sin(beta*xl);
ziden=zo*cos(beta*xl)+i*zl*sin(beta*xl);
zin=zo*zinum*inv(ziden);
%*************************************************************************

%Calculate voltage and current at termination.
v1=v1m*[1;exp(i*-2*pi/3);exp(i*2*pi/3)];     %source voltage phasors (volts)
i1=inv(zin)*v1;                              %source current (amps)

v2=v1*cos(beta*xl)-i*zo*i1*sin(beta*xl);   %calculate termination voltage from equation
2.44a subtract and
                                             %add equations 2.44a & 2.44b for x=0, then
substitute into 2.44a then use trig ID
i2=inv(zl)*v2;
%*************************************************************************
%
%Calculate the voltages, currents, power, and angle differences for each position of the
line from the load to the source.
x=0:0.1:xmiles;             %calculate for the entire line; distance from load.
matrixsize=size(x);
numpoints=matrixsize(1,2);
for position=1:numpoints;
    dismiles=x;
    xx=x(position)*1609.43; %convert distance units from miles to meters.
    vf(:,position)=v2*cos(beta*xx)+i*zo*i2*sin(beta*xx);
    If(:,position)=i2*cos(beta*xx)+i*yo*v2*sin(beta*xx);
    va(1,position)=vf(1,position);
    vb(1,position)=vf(2,position);
    vc(1,position)=vf(3,position);
    ia(1,position)=If(1,position);
    ib(1,position)=If(2,position);
    ic(1,position)=If(3,position);
    pa(1,position)=real(va(1,position)*conj(ia(1,position)));        %recieved
instantaneous real power for each phase
    pb(1,position)=real(vb(1,position)*conj(ib(1,position)));
    pc(1,position)=real(vc(1,position)*conj(ic(1,position)));
    qa(1,position)=imag(va(1,position)*conj(ia(1,position)));        %recieved
instantaneous reactive power for each phase
    qb(1,position)=imag(vb(1,position)*conj(ib(1,position)));
    qc(1,position)=imag(vc(1,position)*conj(ic(1,position)));

    pt(1,position)=pa(1,position)+pb(1,position)+pc(1,position);                %recieved
total real power
    qt(1,position)=qa(1,position)+qb(1,position)+qc(1,position);                %recieved
total reactive power
    S(1,position)=sqrt(pt(1,position)^2+qt(1,position)^2);                      %recieved
total apparant power
    PF(1,position)=pt(1,position)/S(1,position);                                %power
factor

end

delthetaV0=(angle(va)-angle(va(1)))*180/pi; %calculate voltage angle differences over
distance with respect to first phase
delthetaVb=(angle(vb)-angle(va))*180/pi-120;
delthetaVc=-(angle(vc)-angle(va))*180/pi-120;



%delthetaI0=angle(ia)*180/pi; %calculate current angle differences over distance with
respect to first phase
delthetaIb=(angle(ib)-angle(ia))*180/pi-120;
delthetaIc=-(angle(ic)-angle(ia))*180/pi-120;

%Find LL voltage mags
Vab=abs(va-vb);
Vbc=abs(vb-vc);
Vca=abs(vc-va);
```

```
thetava=angle(va)*180/pi;
thetavb=angle(vb)*180/pi;
thetavc=angle(vc)*180/pi;

thetavab=angle(va-vb)*180/pi;
thetavbc=angle(vb-vc)*180/pi;
thetavca=angle(vc-va)*180/pi;

EFF=pt/pt(1,numpoints);                                          %Efficiency
%*************************************************************************
x=2
%Plot output
%NOTE: x=0 corresponds to the location of the load.*****************************
figure(1);
subplot(4,2,1), plot(dismiles,abs(va),'g',dismiles,abs(vb),'b',dismiles,abs(vc),'r');
    title('voltage magnitude per phase (kV)');
    %xlabel('distance (miles)');
    %axis([0,xl/1609.3,0,80]);
    %axis([0,xl/1609.3,0,80]);
    grid;
subplot(4,2,2), plot(dismiles,abs(ia),'g',dismiles,abs(ib),'b',dismiles,abs(ic),'r');
    title('current magnitude (kA)');
    %xlabel('distance (miles)');
    %axis([0,xl/1609.3,0,3]);
    grid;
subplot(4,2,3),
plot(dismiles,angle(va)*180/pi,'g',dismiles,angle(vb)*180/pi,'b',dismiles,angle(vc)*180/p
i,'r');
    title('voltage phase angles (deg)');
    %xlabel('distance (miles)');
    grid;
subplot(4,2,4),
plot(dismiles,angle(ia)*180/pi,'g',dismiles,angle(ib)*180/pi,'b',dismiles,angle(ic)*180/p
i,'r');
    title('current phase angles (deg)');
    %xlabel('distance (miles)');
    grid;
subplot(4,2,5), plot(dismiles,(angle(va)-angle(ia))*180/pi,'g',dismiles,(angle(vb)-
angle(ib))*180/pi,'b',dismiles,(angle(vc)-angle(ic))*180/pi,'r');
    title('angle between voltage and current (deg)');
    %xlabel('distance (miles)');
    %axis([0,xl/1609.3,-20,0]);
    grid;
subplot(4,2,6), plot(dismiles,delthetaVb,'b',dismiles,delthetaVc,'r');
    title('delta in voltage phases (deg)');
    %xlabel('distance (miles)');
    %axis([0,xl/1609.3,-1,1]);
    grid;
subplot(4,2,7),
plot(dismiles,abs(va)*sqrt(3),'g',dismiles,abs(vb)*sqrt(3),'b',dismiles,abs(vc)*sqrt(3),'
r');
    title('line-to-line voltage magnitude (kV)');
    xlabel('distance (miles)');
    %%axis([0,xl/1609.3,65.5,66.5]);
    %axis([0,xl/1609.3,0,80]);
    grid;
subplot(4,2,8), plot(dismiles,delthetaIb,'b',dismiles,delthetaIc,'r');
    title('delta in current phases (deg)');
    xlabel('distance (miles)');
    grid;
%subplot(4,2,8), plot(dismiles,pa,'g',dismiles,pb,'b',dismiles,pc,'r');
%   title('real power in each phase (MW)');
%   xlabel('distance (miles)');
%   grid;

figure(2);
subplot(4,1,1), plot(dismiles,pa,'g',dismiles,pb,'b',dismiles,pc,'r');
    title('real power in each phase (MW)');
    %xlabel('distance (miles)');
```

```
    grid;
subplot(4,1,2), plot(dismiles,qa,'g',dismiles,qb,'b',dismiles,qc,'r');
    title('reactive power in each phase (MVars)');
    %xlabel('distance (miles)');
    %axis([0,10,220,230]);
    grid;
subplot(4,1,3), plot(dismiles,pt,'r')
    title('total power (MW)');
    %xlabel('distance (miles)');
    %axis([0,10,220,230]);
    grid;
subplot(4,1,4), plot(dismiles,qt,'r');
    title('total reactive power (MVars)');
    xlabel('distance (miles)');
    %axis([0,10,220,230]);
    grid;

figure(3);
subplot(4,1,1), plot(dismiles,S,'r')
    title('total apparent power (MVA)');
    %xlabel('distance (miles)');
    %axis([0,10,220,230]);
    grid;
subplot(4,1,2), plot(dismiles,PF,'r')
    title('power factor of the line (leading)');
    %xlabel('distance (miles)');
    %axis([0,10,0,1]);

    grid;
subplot(4,1,3), plot(dismiles,EFF,'r')
    title('efficiency (Pout/Pin)');
    xlabel('distance (miles)');
    %axis([0,10,0,1]);
    grid;

figure (4)
subplot(4,1,1), plot(dismiles,abs(va),'g',dismiles,abs(vb),'b',dismiles,abs(vc),'r')
    title('Simulation Results of the 13.2 kV Triaxial Cable Using Telegraph Equations');
    ylabel('L-n voltage (Vrms)');
    %axis([0,10,0,1]);
    grid;

subplot(4,1,2), plot(dismiles,Vab,'g',dismiles,Vbc,'b',dismiles,Vca,'r')
    ylabel('L-L voltage (Vrms)');
    %axis([0,10,0,1]);
    grid;


subplot(4,1,3), plot(dismiles,thetava,'g',dismiles,thetavb,'b',dismiles,thetavc,'r')
    ylabel('thetavln [degrees]');
    %axis([0,10,0,1]);
    grid;


subplot(4,1,4), plot(dismiles,thetavab,'g',dismiles,thetavbc,'b',dismiles,thetavca,'r')
    ylabel('thetavll [degrees]');
    axis([0,10,-100,160]);
    grid;

%Save data to a file for Excel Plotting and convert from miles to km
M=[dismiles'*1.60943,fliplr(abs(va))',fliplr(abs(vb))',fliplr(abs(vc))',fliplr(abs(ia))',
fliplr(abs(ib))',fliplr(abs(ic))',fliplr((angle(va)-
angle(ia))*180/pi)',fliplr((angle(vb)-angle(ib))*180/pi)',fliplr((angle(vc)-
angle(ic))*180/pi)',fliplr(pt)',fliplr(pa)',fliplr(pb)',fliplr(pc)',fliplr(qt)',fliplr(qa
)',fliplr(qb)',fliplr(qc)',fliplr(S)',fliplr(thetava)',fliplr(thetavb)',fliplr(thetavc)',
fliplr(thetavab)',fliplr(thetavbc)',fliplr(thetavca)',abs(fliplr(Vab))',abs(fliplr(Vbc))'
,abs(fliplr(Vca))'];
WK1WRITE('C:\AEPtemp\TE10mile13kv',M);
```

“triaxfault”

```
%*//////ATP--.pl4 FILE CAPTURE FOR ATP TRIAXIAL CABLE FAULT SIMULATION//////////////    *
%*  Loads time, voltage, and current data columns from .pl4 file and performs           *
%*  desired calculations so that line characteristics can be plotted as a function     *
%*  of distance.                                                                        *
%*  ///////////////created by Marcus Young/////June 23, 2004//////////////             *
%*************************************************************************************

clear;
clc;

%Load .pl4 file & assign data-------------------------------------------------------------
alldata=load('c:\ATP_DRAW39\ATP\triax10mile1.pl4');
sizedata=size(alldata)
columns=sizedata(1,2)
datacolumn=sizedata(1,1)

time=alldata(:,1);
i=1;
for k=2:4
    V(:,i)=alldata(:,k);
    i=i+1;
end
i=1;
for k=5:12
    I(:,i)=alldata(:,k);
    i=i+1;
end

%plot(time,I(:,5)*1e-3,time,I(:,6)*1e-3,time,I(:,7)*1e-3,time,I(:,8)*1e-3);

M=[time,I(:,5)*1e-3,I(:,6)*1e-3,I(:,7)*1e-3,I(:,8)*1e-3];
WK1WRITE('C:\AEPtemp\13kvslgout',M);
```

Appendix C

Results of 13.2 kV Steady-State

Simulations with an Inductive Load

Simulation of a 13.2 kV Triaxial Cable with an Inductive Load

Inductive Load Specifications

All specifications used for the steady-state simulation of a 13.2 kV triaxial cable with an inductive load were the same as for the 13.2 kV cable described in chapter 2. The inductance and resistance in the load were chosen such that it would operate at 0.9 power factor lagging.

Steady-State Simulation Results

Results from ATP and TE model simulations are plotted in this section. Solid lines represent ATP results, and the dashed lines represent those of the TE model.

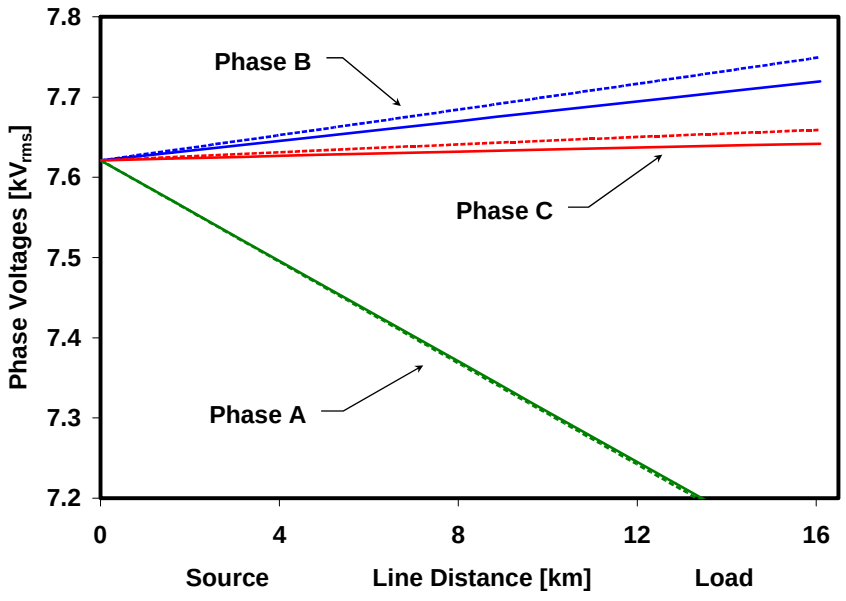

Figure (A.1) Phase voltages of a 13.2 kV triaxial cable with an inductive load.

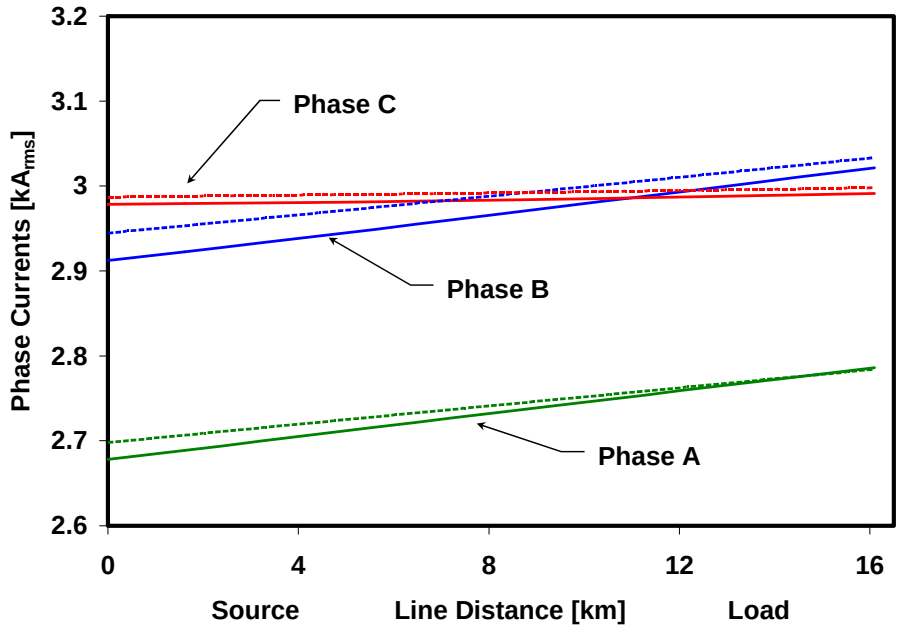

Figure (A.2) Phase Currents of a 13.2 kV triaxial cable with an inductive load.

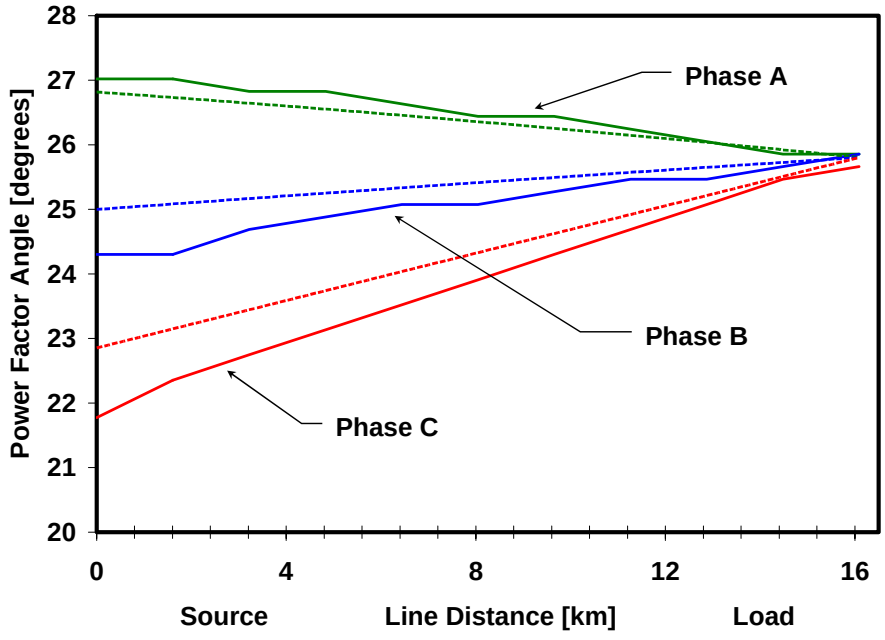

Figure (A.3) Power factor angles of a 13.2 kV triaxial cable with an inductive load.

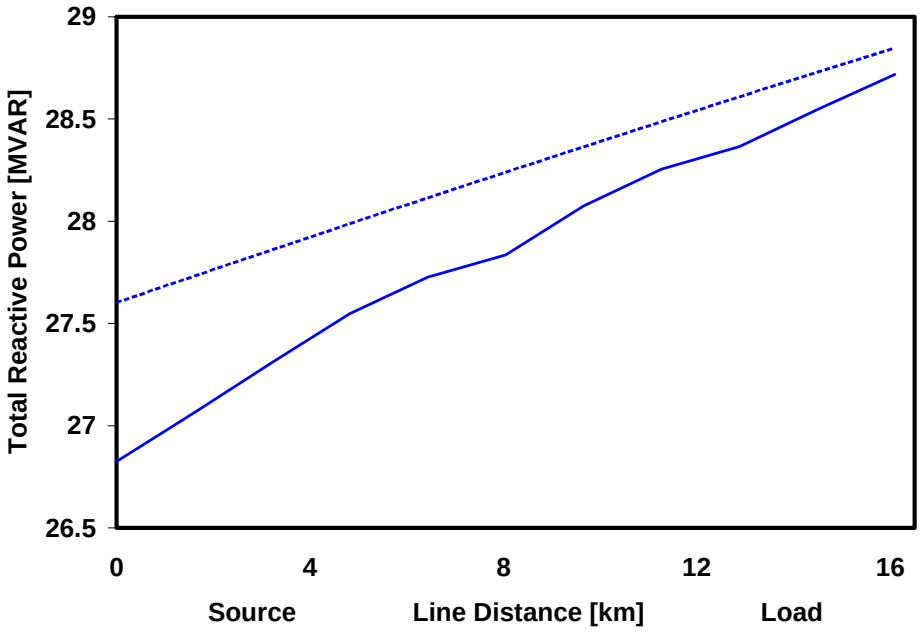

Figure (A.4) Total reactive power of a 13.2 kV triaxial cable with an inductive load.

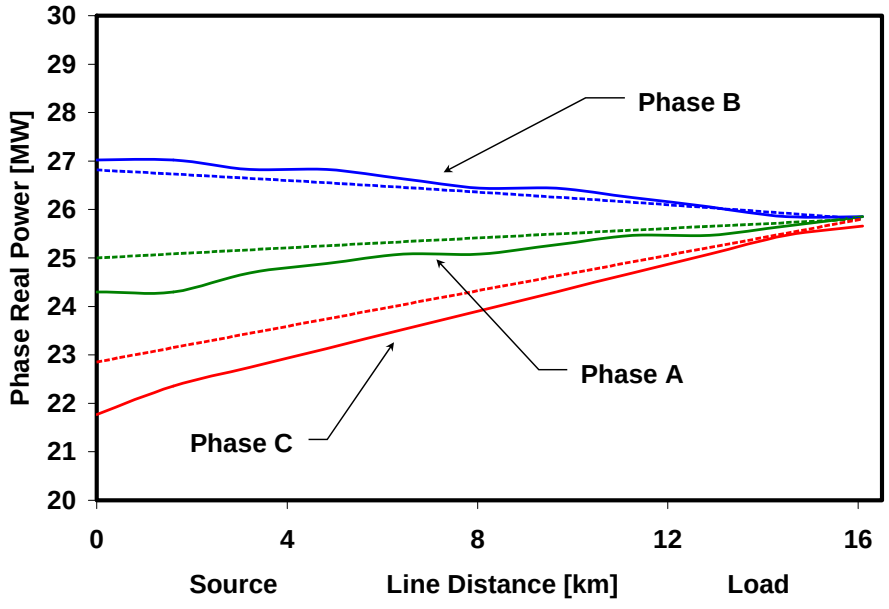

Figure (A.5) Phase real power of a 13.2 kV triaxial cable with an inductive load.

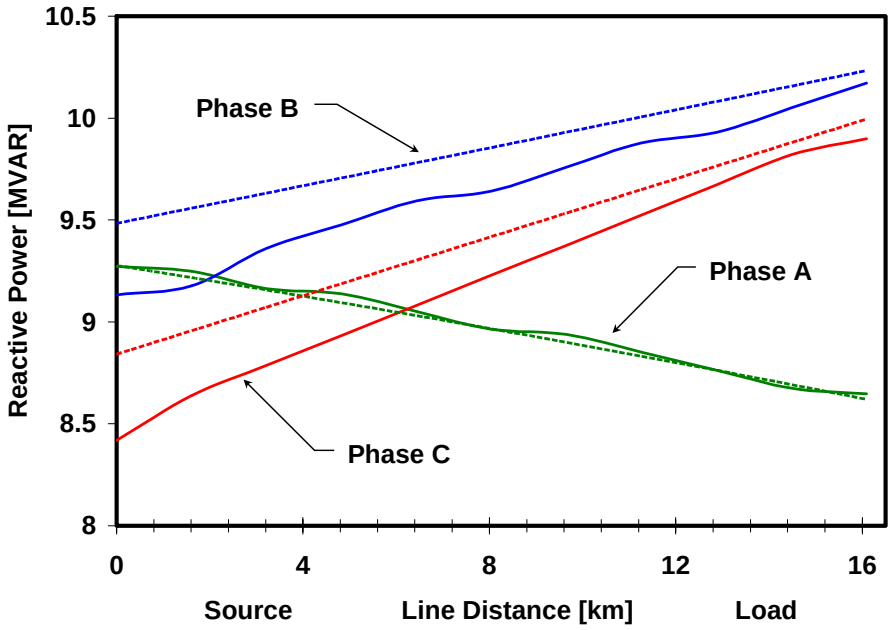

Figure (A.6) Phase reactive power of a 13.2 kV triaxial cable with an inductive load.

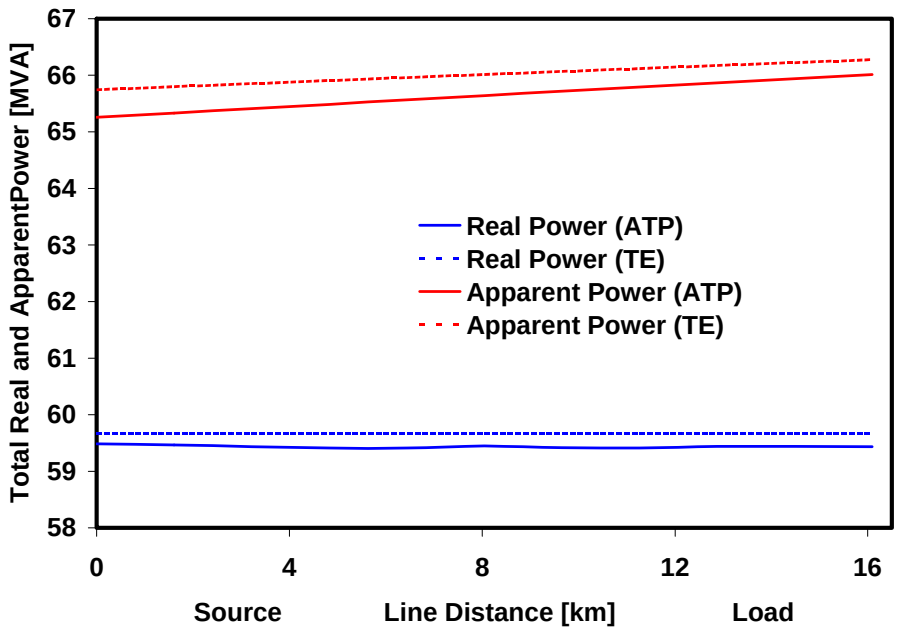

Figure (A.7) Total real and apparent power of a 13.2 kV triaxial cable with an inductive load.

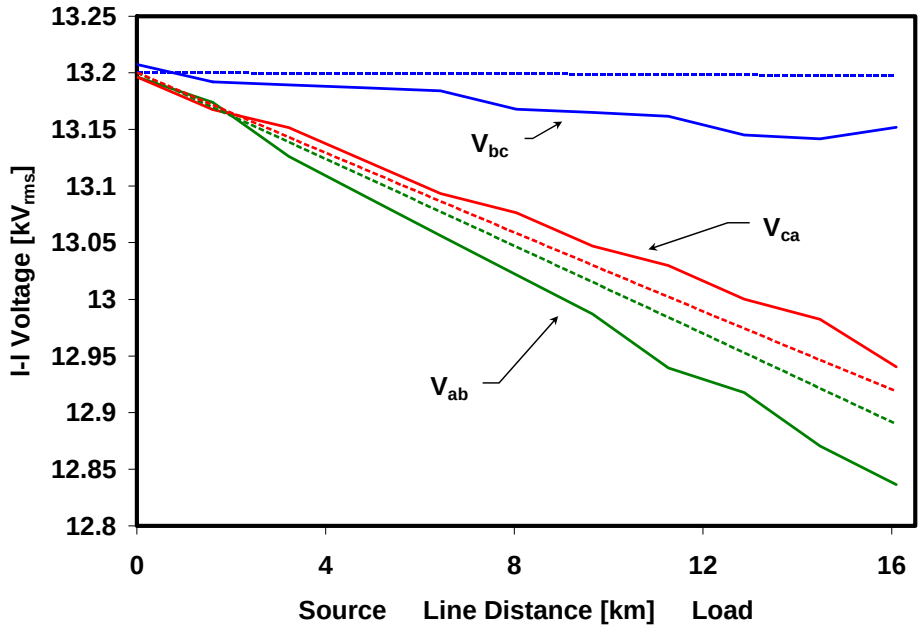

Figure (A.8) Line-to-line voltages of a 13.2 kV triaxial cable with an inductive load.

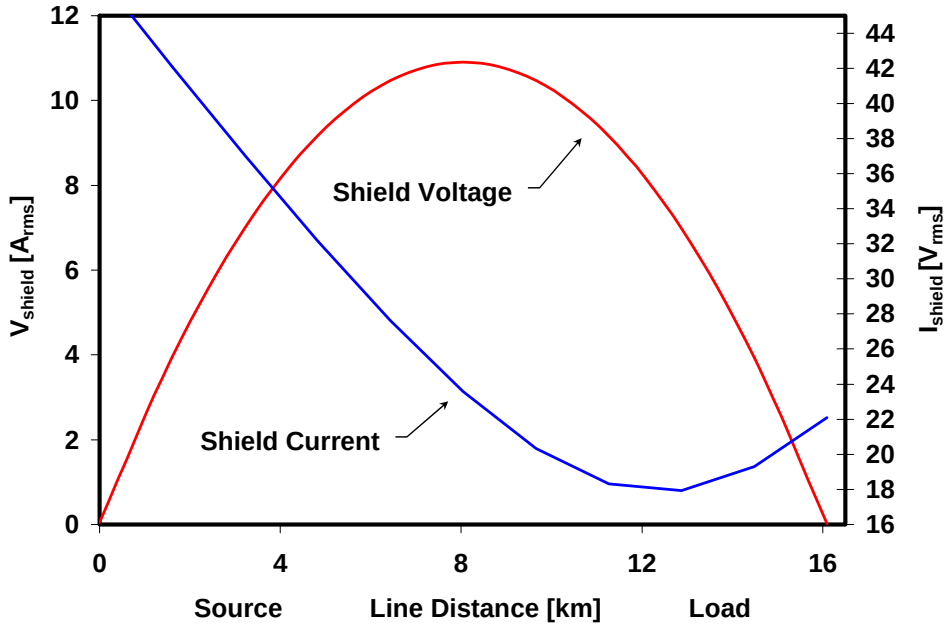

Figure (A.9) Copper shield voltage and current for a 13.2 kV triaxial cable with an inductive load.

Appendix D

Specifications and Results from 69 kV Steady-State Simulations

Simulation of a 13.2 kV Triaxial Cable

69 kV Triaxial Cable Specifications

All specifications used for the 69 kV steady-state simulations were the same as for the 13.2 kV cable described in chapter 2, except for differences in the phase and shield radii. The axial field inductance was excluded from the simulations. The average phase and shield radii approximated for the 69 kV triaxial cable are presented in table (A.1).

69 kV Triaxial Cable Steady-State Simulation Results

Results from ATP and TE model simulation are plotted in this section. Solid lines represent ATP results, and the dashed lines represent those of the TE model.

Table (A.1) Average phase and shield radii of a 69 kV triaxial cable.

Conductor	Average radius [mm]
Phase A	19
Phase B	26
Phase C	33
Shield	40

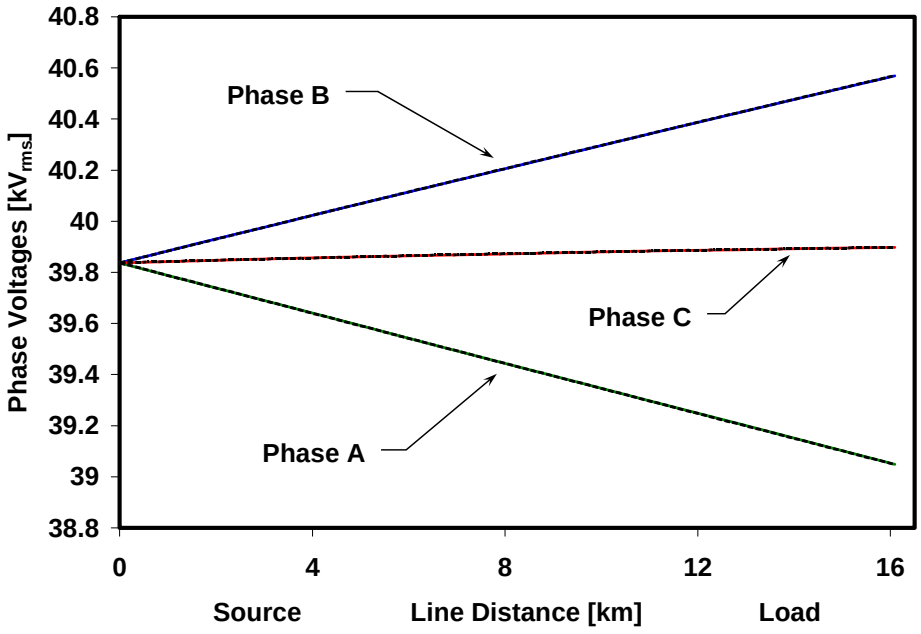

Figure (A.10) Phase voltages of a 69 kV triaxial cable.

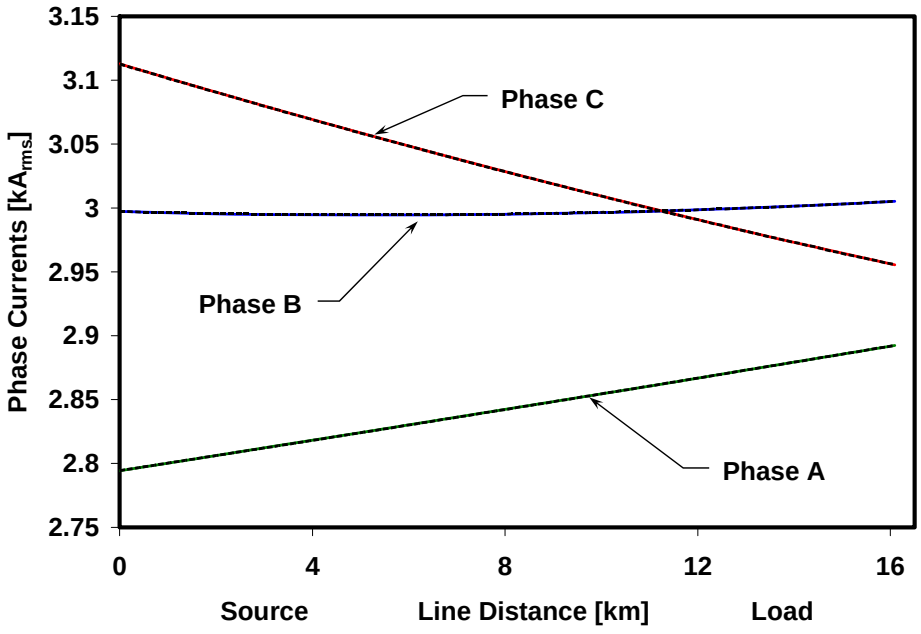

Figure (A.11) Phase Currents of a 69 kV triaxial cable.

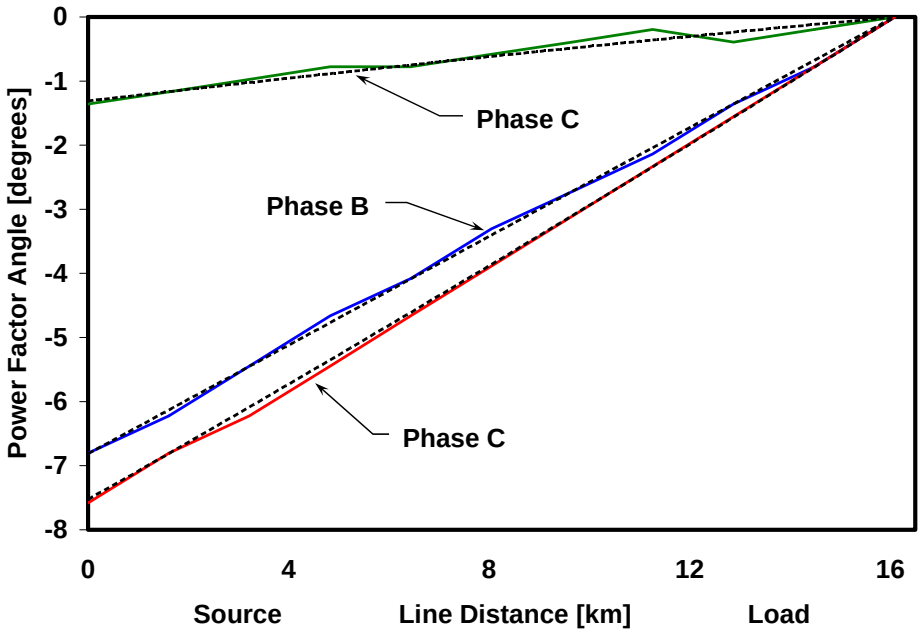

Figure (A.12) Power factor angles of a 69 kV triaxial cable.

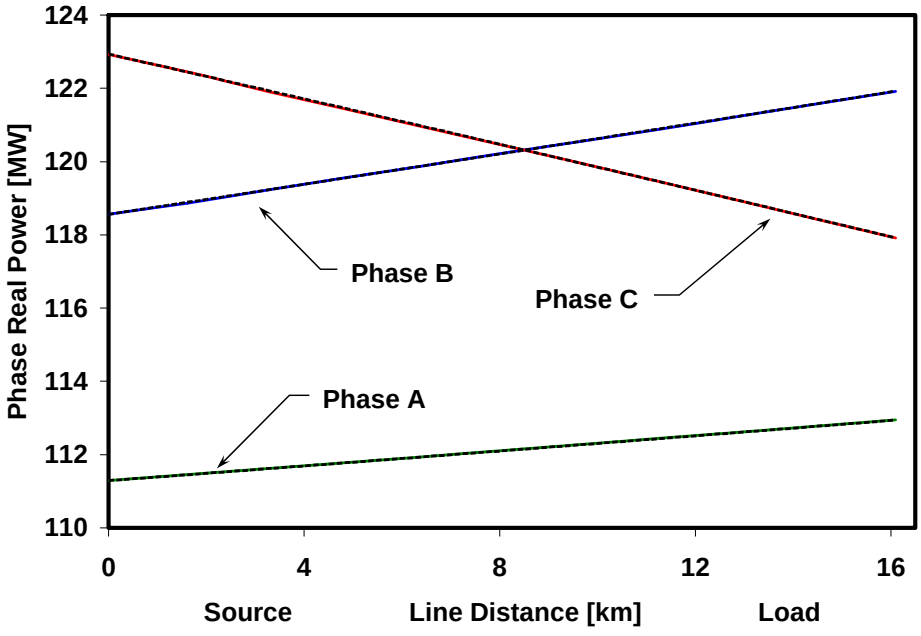

Figure (A.13) Phase real power of a 69 kV triaxial cable.

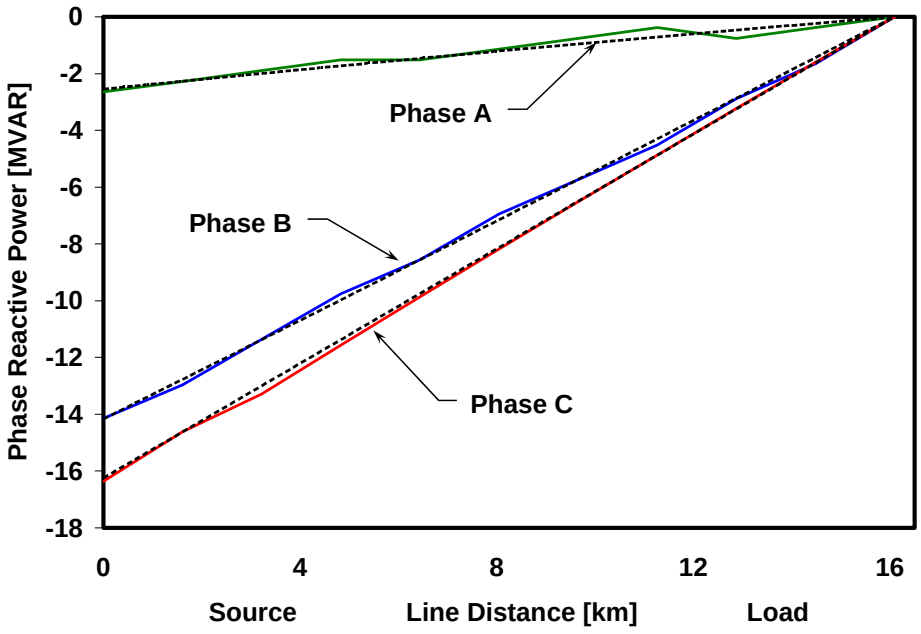

Figure (A.14) Phase reactive power of a 69 kV triaxial cable.

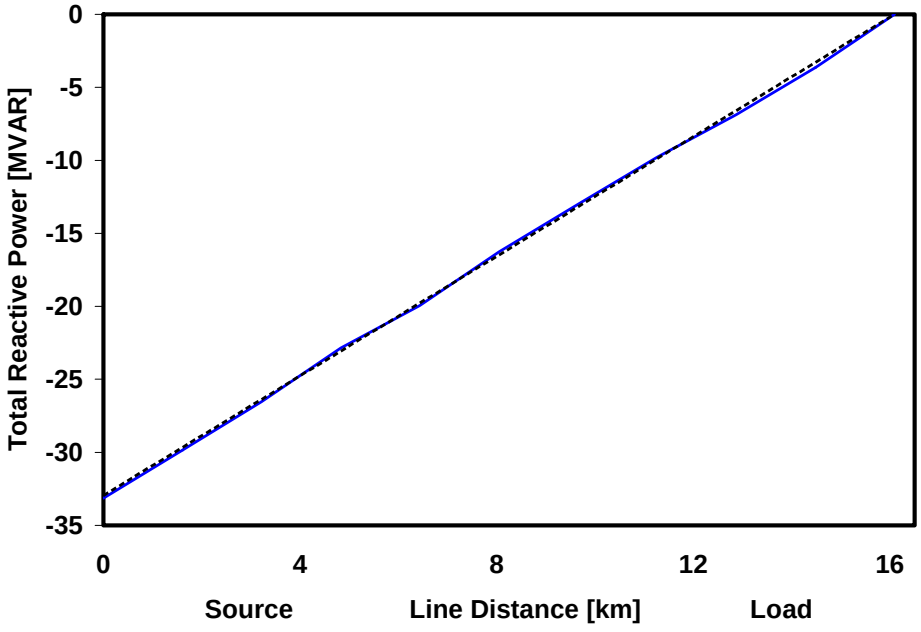

Figure (A.15) Total reactive power of a 69 kV triaxial cable.

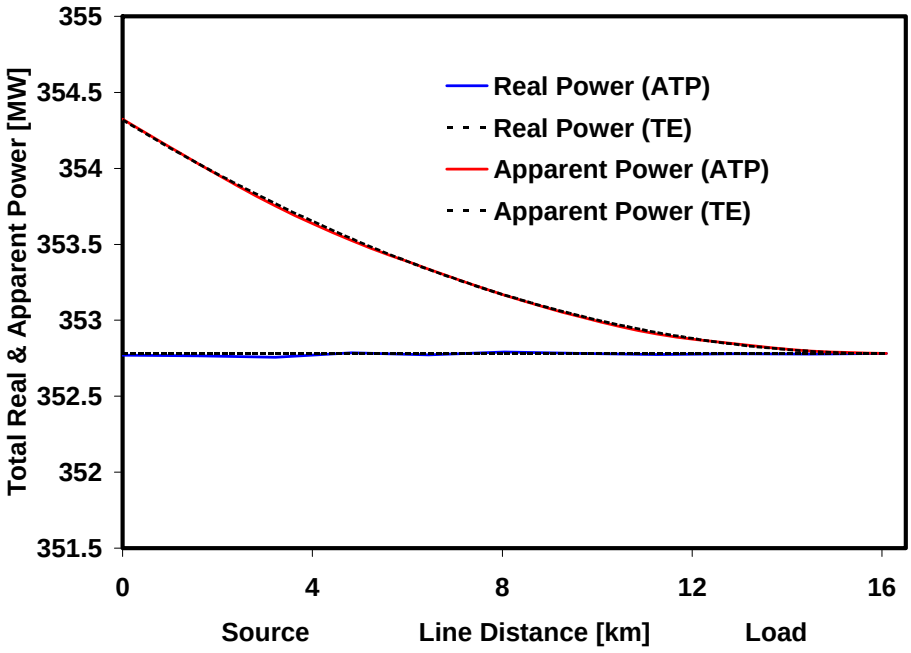

Figure (A.16) Total real and apparent power of a 69 kV triaxial cable.

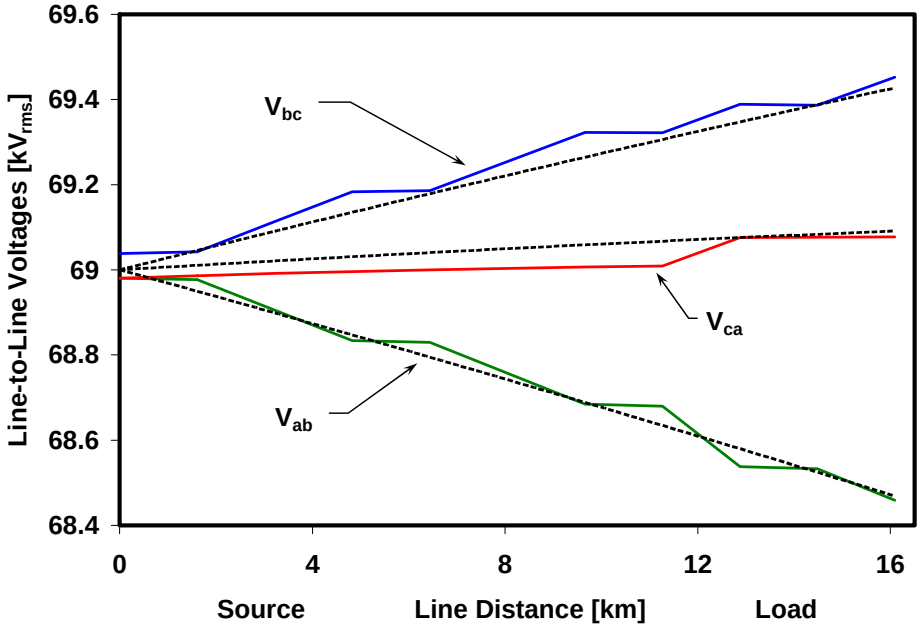

Figure (A.17) Line-to-line voltages of a 69 kV triaxial cable.

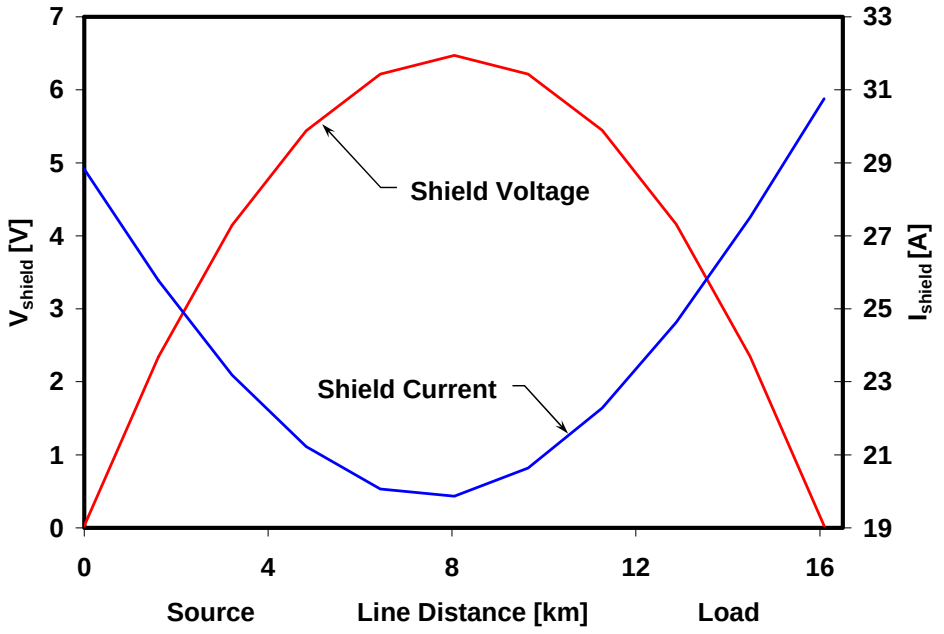

Figure (A.18) Copper shield voltage and current for a 69 kV triaxial cable.

Appendix E

Equivalent Network Impedance

Calculation of the Equivalent Network Impedance

The equivalent network impedance of the 13.2 kV power system simulated in chapter 5 was approximated from assumed values about the short circuit impedance of the system to represent a nominal case [45]. A list of the assumptions made and the calculation of the positive and zero sequence components are provided in this section.

List of assumptions

1) Short circuit capacity (SSC) of the transformer ~ 10%.
2) Minimum transformer rating ~ 70 MVA (at least that of the cable).
3) Short circuit power of the source is 20 times that of the transformer (20 X 70 ~ 1400MVA).
4) R/X ratio ~ 1/10, this ratio assumes a bulk 138 kV/13.2 kV network. The 1/10 value is a nominal value chosen to represent the bulk network as on impedance. The R/X ratio is generally not a used value in power system studies, however in this case it provides nominal values of impedance for simulations conducted in this study.
5) For the Delta/WYE-grounded transformer, $Z_o = Z_+$.
6) For the source, $Z_o = 1.5 * Z_+$.

Calculation of the equivalent network impedance

Positive sequence:

$$X_{+-transformer} \cong \left(\frac{13.2^2}{70} \right) \times 10\% \cong 0.25 \qquad [ohms] \qquad \text{(D.1)}$$

$$X_{+-source} \cong \left(\frac{13.2^2}{1400}\right) \cong 0.125 \qquad [ohms] \qquad \text{(D.2)}$$

$$R_{+-transformer} = 0 \qquad [ohms] \qquad \text{(D.3)}$$

$$R_{+-source} \cong \frac{X_{x-source}}{10} \cong 0.0125 \qquad [ohms] \qquad \text{(D.4)}$$

$$Z_{+} = Z_{+-trasformer} + Z_{+-source} \cong 0.0125 + j0.375 \qquad [ohms] \qquad \text{(D.5)}$$

Zero sequence:

$$R_{o-transformer} = R_{+-transformer} = 0 \qquad [ohms]$$

$$X_{o-transformer} = X_{+-transformer} \cong 0.25 \qquad [ohms]$$

$$R_{o-source} \cong 1.5 \times (0.0125) \cong 0.019 \qquad [ohms]$$

$$X_{o-source} \cong 1.5 \times (0.125) \cong 0.190 \qquad [ohms]$$

$$Z_{o} = Z_{o-trasformer} + Z_{o-source} \cong 0.019 + j0.44 \qquad [ohms] \qquad \text{(D.6)}$$

Vita

Marcus Young was born in Oak Ridge, TN on June 17, 1977. He graduated from Faith Christian School in 1995 and received an A.S. from Pellissippi State Technical Community College in 1998. From there, he went to the University of Tennessee, Knoxville and received a B.S. in Electrical Engineering in 2002.

Marcus is currently working with the Applied Superconductivity Group at the Oak Ridge National Laboratory in the development of high temperature superconducting electric power applications.